2019

Processing of Advanced Infrared Materials

Daniel Mcgill
University of Central Florida

PROCESSING OF ADVANCED INFRARED MATERIALS

by

DANIEL J. MCGILL
B.S., University of Colorado at Colorado Springs, 2007
B.S., University of Colorado at Colorado Springs, 2012

A thesis submitted in partial fulfillment of the requirements
for the degree of Master of Science
in the College of Optics and Photonics
at the University of Central Florida
Orlando, Florida

Spring Term
2019

ABSTRACT

Infrared transparent glassy and crystalline materials often have unique and complex processing requirements but are an important class of materials for such applications as optical windows, lenses, waveplates, polarizers and beam splitters. This thesis investigates two specific materials, one amorphous and one crystalline, that are candidates for use in the short and midwave-infrared and mid and longwave infrared, respectively. It is demonstrated that an innovative uniaxial sintering process, which uses a sacrificial pressure-transmitting medium, can be used to fully densify a $70TeO_2$-$20WO_3$-$10La_2O_3$ (TWL) glass powder. The characteristics of the sintered TWL glass is compared to that of a parent glass produced through a conventional melt/quench process to ascertain the impact of process-specific property changes on the resulting material. Additionally, the design, construction and characterization of a custom-made transparent Bridgman crystal growth furnace is undertaken to enable growth of highly birefringent tellurium single crystal. The key obstacles that need to be overcome to scale up the size of the grown crystals are summarized with the end goal of producing commercial grade optical elements.

To Maureen,

my beautiful wife,

whose sacrifice, support and abundant love have made this work possible.

ACKNOWLEDGMENTS

I would like to thank my thesis advisers Dr. Kathleen Richardson and Dr. Romain Gaume at the University of Central Florida. They patiently guided me through all my work and were always available when I needed support. I look forward to working with them both in the future.

I would also like to thank the current and former members of the Optical Ceramics and Glass Processing and Characterization Laboratories for their assistance and advice on my research. In particular, I would like to thank Dr. Myungkoo Kang, Dr. Anupama Yadav, Dr. Claudia Goncalves, Cesar Blanco, Matthew Julian, Ryker Chute and Chanelle Arias for their great assistance.

Work on this thesis was partially supported by funding from Lockheed Martin Corporation, David Twede, technical point of contact. Without this support my research on tellurium crystals would not have been possible.

TABLE OF CONTENTS

LIST OF FIGURES

LIST OF TABLES

CHAPTER ONE:
MOTIVATION AND OBJECTIVE

Glassy and crystalline materials that are transparent to infrared (IR) radiation are an important class of materials for use in such applications as optical windows, lenses, waveplates, polarizers, beam splitters and prisms. Many of the materials that are used in the visible spectral region are not transparent in the infrared and therefore alternative materials which enable this optical functionality, must be identified and their processing routes defined.

Glasses based upon tellurium dioxide (TeO_2) have a broad transmission range of 0.4-6 µm, are corrosion resistant, possess a high linear refractive index (n), a low phonon energy for an oxide glass and are highly soluble to rare-earth elements which make them ideal for use as optical fibers, laser sources and amplifiers (Churbanov et al., 2005; Dorofeev et al., 2011; Feng, Qi, Lin, & Hu, 1999). This study focuses on a multi-component glass, $70TeO_2$-$20WO_3$-$10La_2O_3$ (TWL). TWL glass has been studied for its use in fiber optics since the addition of La_2O_3 has been shown to increase the stability of the glass to crystallization over and above that of the binary tungstate tellurite (TW) glasses (Churbanov et al., 2005; Dorofeev et al., 2011).

The production of TWL glass in near-net shape is particularly desirable since it would represent a significant reduction in post-processing cost and time, from

operations such as cutting and polishing as well as in the production of preforms and lenses. A possible route for such manufacturing of near-net shape parts is by sintering of powder, such as $70TeO_2$-$20WO_3$-$10La_2O_3$ (TWL) glass powder, through use of a sacrificial pressure-transmitting approach. This approach to sintering has been developed for use with the manufacture of many materials but has not previously been investigated for use with glass materials (Ballard & Hendricks, 1966; Barbaras, 1969; Brennan, 1950; Googin & McLaughlin, 1966; Lange & Terwilliger, 1973; Lepp & Slyh, 1951; Manière, Durand, Weibel, Chevallier, & Estournès, 2016; Wagner, 1960). Therefore, the first objective of this portion of the thesis was the study and evaluation of a sacrificial pressure-transmitting secondary powder approach to uniaxial sintering of TWL glass. A key goal of this study was that any further processing of the TWL glass powder would not adversely impact the key attributes of the glass, such as its optical properties for which the material is principally being used.

To evaluate the potential of a sacrificial pressure-transmitting secondary powder approach to uniaxial sintering of TWL glass an understanding of two key issues were addressed:

1) Identify process-specific limitations such as material contamination from the sintering environment (die, atmosphere), die adhesion, and redox reactions.

2) Identify post process material modifications such as change to the glass' absorption spectrum, index of refraction, composition, amorphous structure and density.

In addition to understanding these two key issues, three objectives needed to be met by this study: 1) achieve a density of the sintered samples > 90 % of that of the melt/quench glass that the starting powder has been derived from, 2) realize a fully amorphous (i.e., crystallite-free) post-sintered sample, and 3) ensure no detectable contamination from the sacrificial powder in the post-processed part.

The second goal of this thesis is related to the design, construction and characterization of a transparent Bridgman furnace and its viability in the production of single crystalline boules of tellurium through a conventional growth process. Crystal manufacturing is a continually developing field with a great many applications to industry which few laboratory spaces are equipped and one which the Ceramic Materials Laboratory wishes to participate in. While previously well studied, recent interest in IR systems requiring larger size optics (> 1" in size) has stimulated the current effort.

Crystalline tellurium was chosen to evaluate the growth capabilities of the designed furnace because it is a commercially unavailable material with unique production concerns and is of interest for its exceptionally high birefringence and transmission from the mid- to longwave infrared (MWIR/LWIR). Its exceptional birefringence is

of particular interest for use in splitting optical elements where the size of the element can be reduced by finding materials with much greater values. In Table 1, the birefringence and transmission window of tellurium is compared with those of other commonly used birefringent materials. No commercially available material was found which could compare to the birefringence of tellurium, within the corresponding spectral window of use (MWIR/LWIR).

Table 1. Birefringence and transmission range of tellurium and commonly used birefringent crystals

Crystal	**Birefringence (at 632.8 nm)**	**Transmission μm (at 300K and >10%)**
Te	-1.45 (4 μm)	3.5 – 32
TiO_2	0.288	0.42 – 4.0
YVO_4	0.2233	0.35 – 4.8
$CaCO_3$ (Calcite)	-0.172	0.2 – 5.5
$PbMoO_4$	-0.123	0.4 – 5.9
TeO_2	0.35	0.33 – 5.0
$LiNbO_3$	-0.076	0.35 – 5.0
MgF_2	0.0118	0.13 – 7.7
α-SiO_2 (Quartz)	0.0095	0.16 – 4.0
$NaNO_3$	-0.251	0.35 – 3
KH_2PO_4 (KDP)	0.03	0.20 – 1.5
$NH_4H_2PO_4$ (ADP)	-0.0458	0.19 –1.5

Source: (Weber, 2003)

For the present effort on IR crystal growth, the following objectives guided the research activities:

1) Design, construction and characterization of a custom-built transparent Bridgman furnace for the use in growth of single crystalline boules.

2) Growth and characterization of crystalline tellurium boules, for use in future research efforts, as a means of studying this furnace design.

Initial findings related to the objectives defined for TWL and crystal growth are presented in subsequent chapters. Each chapter contains a summary of background and motivation, instrumentation used, results obtained and a discussion of the impact of these measurements. Lastly, a concluding chapter highlights overall findings and suggests areas for future work.

CHAPTER TWO:
SINTERING OF $70TeO_2$-$20WO_3$-$10La_2O_3$ GLASS

Introduction

Glasses based upon tellurium dioxide (TeO_2) have a broad transmission range of 0.4-6 µm, are corrosion resistant, possess high linear (n) and nonlinear (n_2) refractive indices, low phonon energy and rare-earth elements are highly soluble in the glass which make them ideal for use as optical fibers, laser sources and amplifiers (Churbanov et al., 2005; Dorofeev et al., 2011; Feng et al., 1999). $70TeO_2$-$20WO_3$-$10La_2O_3$ (TWL) glass has been studied for its use in fiber optics since the addition of La_2O_3 has been shown to increase the stability of the glass to crystallization over and above that of the binary tungstate tellurite (TW) glasses (Churbanov et al., 2005; Dorofeev et al., 2011). Additionally, La_2O_3 addition to this binary tellurite composition has been shown to increase the solubility of dopants commonly used in laser applications such as Yb^{3+} in these glasses (Feng et al., 1999; Leal et al., 2015).

The production of TWL glass in near-net shape is desirable since it would represent a significant reduction in post-processing cost and time, from operations such as cutting and polishing, in the production of preforms and lenses. The production of near-net shape TW/TWL glasses through spark plasma sintering (SPS) and uniaxial pressing has been studied by previous authors (Bertrand, 2015; Bertrand et al., 2014; Dohlen, 2018; Roumiguier, 2016). It has been found that

these glasses, when produced via SPS, are prone to carbon contamination owing to graphite dies or process atmospheres and that sample adhesion resulting in breakage within dies are key limitations. The contamination due to carbon has not been successfully prevented in pressing or spark plasma sintering despite numerous diffusion barriers being explored to mitigate such contamination (Bertrand, 2015; Roumiguier, 2016). Such contamination has however, been shown to be markedly reduced with the use of bed of alumina powder surrounding a TWL green-body around its top and bottom, during spark plasma sintering (Dohlen, 2018). Similar carbon contamination from SPS has also been noted in other materials such as the production of alumina-magnesia spinel (Bernard-Granger, Benameur, Guizard, & Nygren, 2009; K. Morita, B.-N. Kim, H. Yoshida, K. Hiraga, & Y. Sakka, 2015; K. Morita, B. N. Kim, H. Yoshida, K. Hiraga, & Y. Sakka, 2015).

A possible route for the manufacture of near-net shape parts from the sintering of tellurite glasses such as $70TeO_2$-$20WO_3$-$10La_2O_3$ (TWL) glass powder is through the use of a sacrificial pressure-transmitting approach. This approach to sintering has been developed for use with the manufacture of many materials but has not previously been previously investigated for use with glass materials (Ballard & Hendricks, 1966; Barbaras, 1969; Brennan, 1950; Googin & McLaughlin, 1966; Lange & Terwilliger, 1973; Lepp & Slyh, 1951; Manière et al., 2016; Wagner, 1960). Research on the use of a boron nitride sacrificial pressure-transmitting

powder surrounding a green-body has shown that when the powder is in a loose, non-densified form, it acts as a fluid imparting a near-isostatic pressure upon the green-body during compression (Lange & Terwilliger, 1973). Further the researchers found that once the sacrificial boron nitride pressure-transmitting powder was fully densified, the pressure state became triaxial with differing pressures in the axial and radial directions (Lange & Terwilliger, 1973). Therefore, it was hypothesized in this study that through the use of a highly plastic, potassium chloride sacrificial pressure-transmitting powder surrounding a TWL green-body and the exclusion of graphite within the sintering system, uniaxial hot pressing could densify a TWL to full densification and concurrently reduce the opportunity for carbon contamination.

To evaluate the potential impact on optical quality that sintering with a sacrificial pressure-transmitting secondary powder approach could have several issues which had to be addressed:

1) Identify process-specific limitations such as material contamination from the sintering environment (die, atmosphere), die adhesion, and redox reactions.

2) Identify post process material modifications such as change to the glass' absorption spectrum, amorphous structure and density.

These two aspects of the challenge formed the basis of the present study on processing of TWL powder.

Literature Review

Glasses

A glass is an amorphous solid which does not possess long-range order. Unlike crystalline materials which are organized in a periodic structure of unit cells, the molecular units or atoms in a glass are randomly arranged with only small localized structure being present (few angstrom in size) (Kingery, Bowen, & Uhlmann, 1976). Very few other statements about glasses hold uniformly across the entire field of glassy structures since nearly any material can form a glass when cooled from the melt at a sufficiently fast rate (Varshneya, 1994). Glasses which can be made at moderate cooling rates are characterized as good glass-formers whereas those which require exceptionally rapid cooling rates are usually characterized as poor glass-formers and are often prone to crystallization (Shelby, 2005). Other means of forming glasses besides cooling from a melt also exist such as condensation from vapor, solution processing (sol-gel) or electrodeposition (Kingery et al., 1976).

Glass properties, including the resulting material's volume and thus density are always dependent on the thermal history, or more specifically, the pathway that

the glass melt takes upon cooling from the liquid to the solid state (Pye, Joseph, & Montenero, 2005). A glass-forming material that is cooled from the melt will experience a drop in molecular mobility due to the contracting volume of the material and an associated drop in intermolecular spacing that accompanies the intrinsic increase of viscosity with decreasing temperature (Badrinarayanan, Zheng, Li, & Simon, 2007). As seen in Figure 1, if the melt was cooled rapidly, its structure cannot rearrange to its ideal crystalline state and enters the glassy phase, it will deviate from the straight 'liquidus' line (Varshneya, 1994). The glassy line when extrapolated (dashed line) deviates from the liquidus line at a point represented by the start of the glass transformation region. The tangential intercept of the liquidus and solidus line indicates the glass transition temperature (T_g). Within this region, the glass' mobility decreases with increase of viscosity, arresting further glass movement (Badrinarayanan et al., 2007; Carter & Norton, 2007; Shelby, 2005). Unlike crystals which undergo an instantaneous 'freeze' at the crystallization temperature (upon cooling) that is characterized by a first order phase transition (from liquid to solid), glasses undergo a gradual transition to the solid state and do not exhibit either a characteristic crystallization temperature (upon cooling) or an analogous distinct melting temperature (upon heating) (Pye et al., 2005). The liquidus temperature for a 'conventional' glass melt is where the glass material no longer contains any crystalline fragments or nuclei, and no further nucleation and crystallization can occur. This differs from the glass' fictive

temperature (T_f) which is characterized as the point where the deviation from 'ideal' liquid behavior has occurred (Badrinarayanan et al., 2007). This temperature, as well as the resulting glass' final volume, are thus temperature-dependent as shown for fast and slow-cooled glasses, in Figure 1.

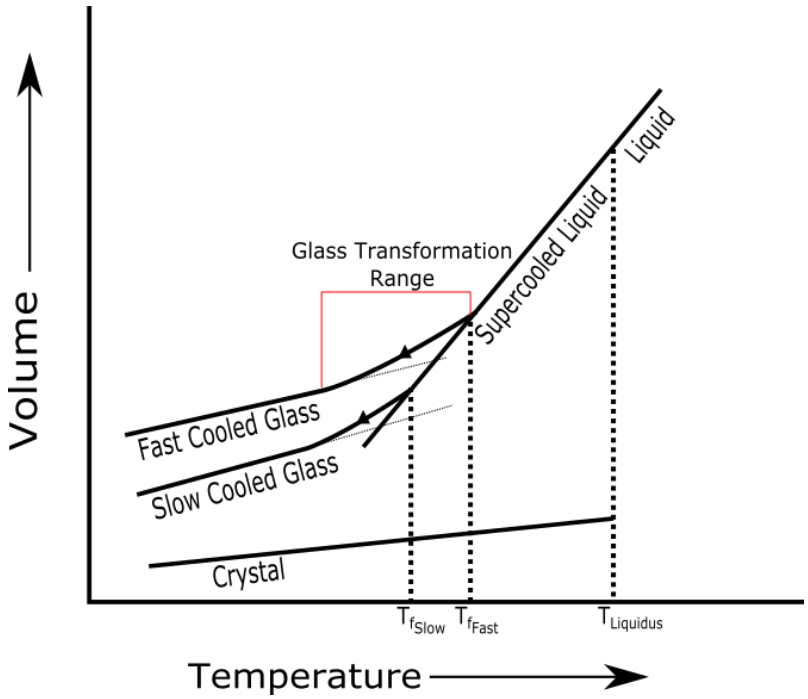

Figure 1. Volume of glass forming melt versus temperature

Source: Figure adapted by author from (Shelby, 2005; Varshneya, 1994)

Most glasses are produced via a melt-quench technique where a glass melt is rapidly cooled (avoiding crystallization) to room temperature and realizes its meta-stable solid state. The medium possesses a non-equilibrium structure, with a volume greater than that of an equivalent crystalline, and similarly, possesses a

density dependent on its thermal history. Other physical and optical properties are also defined by this thermal history and thus, variations on processing that result in a change in this initial thermal history would be expected to modify the resulting glass' structure and properties. The parent glass in this study, the TWL glass processed with our collaborators at the University of Limoges in France, have been produced through such a conventional melt-quench process. The physical characteristics of the parent glass, and those of the powder derived from it, form the starting point for comparison of material produced by any subsequent sintering process. Thus, based upon the expected difference between the parent glass' melt quench thermal history and that imparted through the reheat and pressure of a sintering process, we would expect variations between the resulting properties of the sintered glass compared to those of the parent glass, including a change in density due to a change in molar and free volumes. This increase in density will lead to an associated change in index of refraction (Oughstun & Cartwright, 2003). An equation showing the dependence of index of refraction on density can be derived from electrostatic equations:

$$\frac{(n^2-1)M}{(4\pi+b(n^2-1))\rho} = N_A \sum_i f_i \propto_i \qquad (1)$$

Source: (Oughstun & Cartwright, 2003; Ritland, 1955)

where n is the index of refraction, N_A Avogadro's number, f_i the molar fraction of ions of each type *i*, α_i the polarizability of each ion type *i*, ρ the density and M the

molecular weight. The *b* term is a constant based on the contribution of dipole polarization on the local electric field and is determined by the structure of the material. The well-known Lorentz-Lorenz relation is based upon this equation with a value of *b* equal to 4π/3 and which is valid for randomly arranged dipoles such as found within an amorphous glass:

$$\frac{(n^2-1)M}{(n^2+2)\rho} = N_A \sum_i f_i \propto_i \quad (2)$$

Source: (Oughstun & Cartwright, 2003; Ritland, 1955)

Another relationship, which relates the index of refraction to density is the Gladstone-Dale relationship:

$$\frac{(n-1)}{\rho} = \sum_i k_i w_i \quad (3)$$

Source: (Gladstone & Dale, 1863; Teertstra, 2005)

where k_i is the specific refractive energy of each compositional component *i*, and w_i the weight fraction of each component *i*. All these relationships suggest that for an amorphous solid such as glass, an increase in density is expected to lead to a decrease in index of refraction. Therefore, by adjusting the cooling rate of a glass, one modifies the density of the glassy solid and an associated change to index of refraction occurs. As the post-sintered part produced in this effort is meant for optical applications, verification of the Gladstone-Dale relationship for TWL glass and calculations using this relationship have been performed in this study.

As shown, temperature plays a role in defining the glass structure, but it also influences the initiation and development of crystallization (devitrification) in the glass. In order for a crystal to grow within a glass, a crystal nucleus must form either homogenously and spontaneously or heterogeneously (on a surface such as an impurity) (Kingery et al., 1976). There is no definitive means by which to detect nuclei within a glass so that a glass in which nucleation has occurred without an associated crystal growth is still considered a glass (Shelby, 2005). In normal pressure environments, with no applied force, nucleation and growth will not occur below the glass transition temperature. The laws of thermodynamics suggest that when a force is applied, by a press or by a compressive environment, nucleation and growth can occur even below T_g.

The homogenous growth of nuclei requires an interface to form between two differing phases and typically requires a rise in free-energy of the system (Kingery et al., 1976). If the interfacial energy becomes small when compared to the decrease in volume energy, then the change in free-energy due to the formation of this new phase is negative and the formation of the nuclei is more likely (Kingery et al., 1976). The rate of nucleation per unit volume (I) is:

$$I = nve^{\left(\frac{-N_A W^*}{RT}\right)} e^{\left(\frac{-\Delta G'}{RT}\right)} \quad (4)$$

Source: (Rawson, 1967)

where n atoms/cm^3, v the vibrational frequency of the atoms at the interface between the nucleus and the liquid, N_A Avogadro's number, W^* thermodynamic barrier to nucleation, R the gas constant and ΔG the change in free energy per gram when a transformation from liquid to crystal occurs in an atom (Rawson, 1967). This equation can be understood by looking at:

$$(I_v)_{eq} = vn_s n^* \quad (5)$$

Source: (Kingery et al., 1976)

where $(I_v)_{eq}$ the equilibrium value of the nucleation rate at a certain collision frequency, v the collision frequency, n_s the number of molecules near the critical sized nuclei and n^* the number of critical nuclei per unit volume. The critical size of the nuclei depends on the free-energy of formation by the relation:

$$r^* = -2\gamma/\Delta G \quad (6)$$

Source: (Shelby, 2005)

where γ is the crystal-melt interfacial free-energy per unit area. With rising temperature, the free-energy of formation will decrease causing an associated rise in the critical nuclei's size.

Nucleation can also be heterogeneous where the nuclei form on a surface or interface such as found on a die or impurities within the source material. The presence of these interfaces reduces the activation energy needed for crystal growth to occur. Thus, experimental controls must be in place to try avoiding these issues.

Nuclei are imperceptibly small (on the order of a few atoms, tens of nm's in size) but once they have formed subsequent crystal growth may occur. The crystal growth rate per unit area (U) is expressed as:

$$U = \nu a_o \left[1 - exp\left(-\frac{\Delta G}{kT}\right)\right] \quad (7)$$

Source: (Kingery et al., 1976)

where

$$\nu = \frac{kT}{3\pi a_o^3 \eta} \quad (8)$$

Source: (Kingery et al., 1976)

with a_o being the distance the distance the interface has moved, η the viscosity and ΔG the change in free-energy due to crystallization.

With the nucleation and growth rates in mind, a visual representation of these differing processes can be developed. As seen in Figure 2, at some temperature above T_g, nucleation can occur and the formation rate of nuclei increases with

temperature. As temperature increases further, the critical size of a nuclei increases with decreasing ΔG until the probability of occurrence diminishes. But with decreasing ΔG the growth rate increases until approaching the melting point when structural order begins to break down.

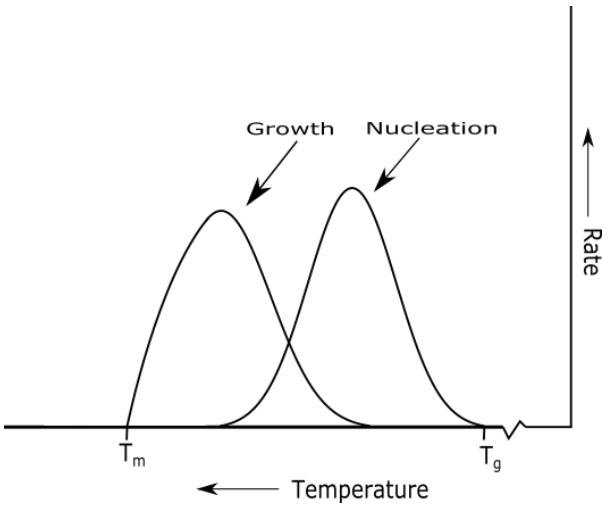

Figure 2. Rates of nucleation and crystal growth of a glass

Source: Figure adapted by author from (Shelby, 2005)

This background discussion is especially important in light of the temperature and pressure conditions employed in the present effort to sinter TWL material. Specifically, the devitrification (crystallization) process whereby nuclei are formed and can subsequently grow into crystals of detectable size is to be avoided during the sintering process, where the heating and cooling rates are much different (slower) than those used to initially form (quench) the parent glass. With analysis through the means of a differential scanning calorimeter a close approximation,

ignoring applied pressure and heterogeneous nucleation, can be carried out to determine the likely outcome of a glass undergoing temperature fluctuations. With this background, specifics related to the TWL glass are now presented.

Tellurite Glasses

As noted previously in this chapter, glasses based upon tellurium dioxide (TeO_2) have a broad transmission range of 0.4-6 μm, are corrosion resistant, possess a high linear (n) and nonlinear (n_2) refractive indices, high phonon energy for an oxide glass and rare-earth elements are highly soluble in tellurite glasses which make them ideal for use as optical fibers, laser sources and amplifiers (Anashkina, Andrianov, Dorofeev, & Kim, 2016; Churbanov et al., 2005; Dorofeev et al., 2011; Fargin et al., 1996; Feng et al., 1999; Ohishi et al., 1998; Wang, Vogel, & Snitzer, 1994; Zhang et al., 2005).

The formation of tellurite glasses is typically done by batching the high purity raw ingredients and grinding them within a mortar and thoroughly mixing to ensure no segregation of constituents. The well-mixed batch is then transferred to a platinum or gold crucible where it is melted and stirred often in a purified oxygen environment. This melt is then quenched on a hot steel or brass plate or poured into a mold and then transferred to an oven for annealing to remove strain from the

system. Specific details on the preparation of TWL glass in the present study will be addressed in the next section.

TW / TWL Glasses

Tellurite glasses contain TeO_2 trigonal bipyramids each which include an electron lone pair (Sokolov, Plotnichenko, Koltashev, & Dianov, 2006; Upender, Bharadwaj, Awasthi, & Mouli, 2009). The lone pair associated with the Te atom is what reduces the glass forming ability of TeO_2 (as compared to SiO_2 or GeO_2) adding a geometric constraint to the structure of the glass (Kaur, Khanna, Sathe, Gonzalez, & Ortiz, 2013). The addition of a metal oxide (a modifier or intermediate) enhances the ability of the Te-O chains to form and adds stability to the network (Kaur et al., 2013). Adding a heavy metal oxide, such as WO_3, also enhances the chemical and devitrification stability of the glass (Çelikbilek, Ersundu, Solak, & Aydin, 2011; Öveçoğlu, Özen, & Cenk, 2006).

The addition of WO_3 causes the formation of TeO_3 trigonal units and the formation of Te-O-W linkages and the formation of these linkages increases with increasing WO_3 content (Kaur et al., 2013). The formation of these Te-O-W linkages is believed to be responsible for the observed increase in the T_g of the produced glasses (Kaur et al., 2013). Tungsten found in the glass is most often in the form W^{6+} but at high temperature and low oxygen environments W^{5+} or W^{4+} become

more likely (Leftheriotis, Papaefthimiou, Yianoulis, & Siokou, 2001; Sarin, 1975; Wilken, Morcom, Wert, & Woodhouse, 1976).

The addition of La_2O_3 (TWL) to the system has the effect of increasing the glass stability further, increasing the T_g to higher temperature and increasing the glasses ability to dissolve large dopants such as Yb^{3+} (Feng et al., 1999). While it was not of specific interest to the present work, tellurite glass systems have been investigated for use in lasers and fiber systems owing to its high glass stability and the solubility of dopants in TWL glass have been shown to be of particular interest (Churbanov et al., 2005; Dorofeev et al., 2011; Feng et al., 1999; Ohishi et al., 1998; Wang et al., 1994; Zhang et al., 2005).

While the Te-O vibrational band of tellurite glasses result in some of the best mid-wave transmission found for oxide glasses, their ultimate transmission in the MWIR range is limited by the presence of impurities. Tellurium oxide is extremely hygroscopic and thus, hydroxyl groups are often present as an impurity within tellurite glasses, adversely impacting the glass' IR transmission (Guery et al., 2014). This hydroxyl impurity, present as an OH^- anion, can be reduced keeping raw materials and batch dry (in a glove box) and by melting the batch ingredients within a purified oxygen environment (Massera, 2009). Using this melting methodology, oxygen species displace OH found in the network along with molecular water by removing them from the matrix (Massera, 2009). Massera also

observed similar reduction of moisture via additions of halides which displace the negatively charged OH^- species. This decrease in OH content would also have the effect on increasing the glass transition temperature (Massera, 2009). The OH content of the glasses can also be reduced by drawing a rod from the melt rather than quenching in air on steel or in a mold thereby reducing the presence of bubbles within the melt and Figure 3 shows the increased transmission obtained through use of this method on 10 mm thick samples (Churbanov et al., 2005). Tellurite glasses with high OH content have large optical absorption at 3 – 4 μm with maximum absorption at 3.3 μm and an additional absorption peak occurs at 4.4 μm associated with hydrogen bonded OH groups (Ebendorff-Heidepriem, Kuan, Oermann, Knight, & Monro, 2012).

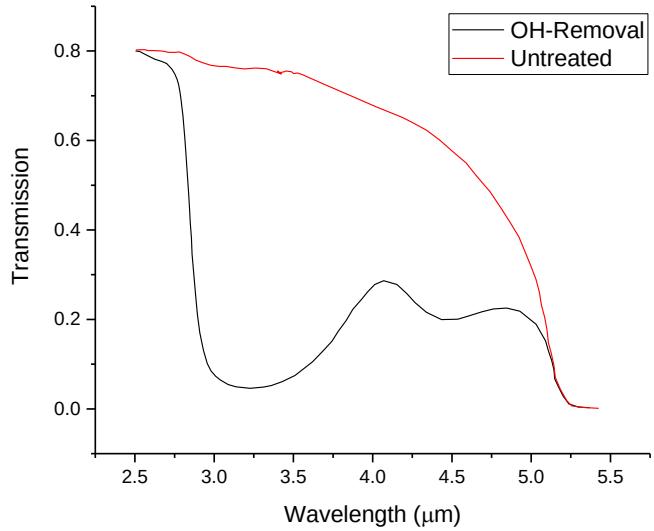

Figure 3. Effect of OH^- removal process on TWL glass by drawing the glass from the melt into rods

Source: Data from (Churbanov et al., 2005)

Tellurite glasses and specifically, $70TeO_2$-$20WO_3$-$10La_2O_3$ (TWL) glass, have been of research interest at the Science of Ceramic Processes and Surface Treatments (SPCTS) group at the University of Limoges for many years. The SPCTS group has kindly supplied the glass powder used for this thesis as part of a multi-year collaboration. TWL glass was prepared by first batching the constituent parts: TeO_2 99.9 % from Toldini GmbH, WO_3 99.8 % from Alfa Aesar and La_2O_3 99.99 % from Rhône-Poulenc. The batch is transferred to a high purity platinum crucible made by Heraeus and melted at 850 ˚C for one hour in lab

atmosphere during which the melt is stirred four times to remove bubbles. The melt is then quenched by pressing between two room temperature brass plates. No annealing is done as the glass is subsequently crushed for use in sintering.

Besides stirring, no special procedures are used to remove OH^- or water such as oxygen rich melt environments or pulling from the melt. This choice has the effect to decrease transmission over a large wavelength region. As seen Figure 3 a process of pulling the glass from the melt (OH group removal) greatly improves transmission (Churbanov et al., 2005).

Sintering of Glasses

Sintering is the process of densifying a powder material into a compact without the means of melting. This densification occurs by application of heat or pressure onto the power compact which causes the individual powder particles to fuse. In the case of a glass, which lack crystalline grains, the fusing of the particles occurs by way of viscous flow where the particles distort and combine (Rahaman, 2008). This thesis focuses on the hot-pressing sintering process where the primary means of densification is by viscous flow.

In the sintering of glasses, sintering usually occurs below the liquidus temperature as operating above the liquidus temperature is typically not referred to as sintering at all (Rabinovich, 1985). This liquidus temperature is the temperature above which

crystallization cannot occur as the molecular mobility is too great to form stable crystalline structures which do not dissolve into the melt (are above the critical radius). Devitrification of the glass is undesirable for two primary reasons (1) sintering by viscous flow occurs at a significantly faster rate than diffusion-induced crystalline grain growth, and (2) crystallites within the glass act as scattering centers within the material which reduces transmission. In order to avoid crystallization most glass sintering research occurs at temperatures below the glass transition but the advantage of lower viscosities at higher temperatures justifies temperatures above the glass transition if crystallization of the resulting compact can be avoided. To aid in avoiding crystallization differential scanning calorimetry can be done to ascertain the growth curves of crystallites and careful selection of operating temperatures, low dwell times and rapid heat up and cool down rates to avoid these growth regions.

Forming glass structures through sintering can have several advantages over making the structure from a melt, including a lower operating temperature and the potential for creation of complex forms and composites. The conventional method of forming a glass structure is through the melting of batching ingredients, pouring/casting the melt into a form (commonly flat or cylindrical in shape) or float, quenching the melt through rapid cooling in air, selective atmosphere or immersion within a coolant. Once cooled, the glass is annealed to remove structural strain, cut and polished to reach the desired shape. Cutting and polishing are done at the

expense of significant time and money. In addition, it may not be possible to create an optically polished complex form or doing so presents numerous manufacturing challenges. Molding of tellurite glass is also a poor option owing to the low stability of tellurites to crystallization. Instead, sintering is a processing route whereby the bulk glass is pulverized and sieved to create a glass powder. This powder is formed into a specific shape either through making a powder compact (green-body) or by filling a specially designed container/die of the desired shape. The resulting extracted post-sintered sample has the near-net shape of the starting powder compact.

Rahaman (2008) discusses three stages which occur when sintering glass (where viscous flow is the dominant densification process): 1) initial stage 2) intermediate stage and 3) final stage. In the initial stage neck growth occurs between particles by means of a variety of mechanisms but importantly for this study viscous flow. Once the neck radius has reached 40 to 50% of the particle radius the intermediate stage is said to begin. The intermediate stage is where further densification occurs leading to pores (voids of gas or vacuum) becoming disconnected from one another. In the final stages the disconnected pores collapse further until full densification occurs (>97% relative density).

According to Frenkel, in the initial stage of sintering, glass particles (non-crystalline grains of the powder), which are assumed to be spheres, are placed in contact

with one another (Frenkel, 1945). With the application of heat and/or pressure they begin to form a system of particles connected via broad necks. The means by which these broad necks form is due to viscous flow in the glassy system and proceeds at a rate such that the rate of energy dissipation by viscous flow equates with the rate of energy gained by reduction in surface area of the particles (Rahaman, 2008). This is described by evaluating the change in surface area of the two touching spheres [Figure 4], where S and S_o are the surface areas of the final and starting spherical particles, a is the radius of the particles, X the radius of the neck and θ the angle formed from particle midpoint to outer radius of the neck.

$$S_o - S = 8\pi a^2 - 4\pi a^2(1 + cos\theta) \quad (9)$$

Source: (Rahaman, 2008)

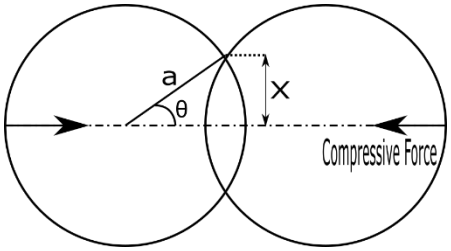

Figure 4. Frenkel model of neck growth

Source: Figure adapted by author from (Frenkel, 1945)

The rate of change of energy (dE_s/dt) owing to the reducing surface area is expressed as:

$$\dot{E}_s = -\gamma_{SV}\frac{dS}{dt} = 4\pi a^2 \gamma_{SV}\frac{d}{dt}\left(\frac{\theta^2}{2}\right) \quad (10)$$

Source: (Rahaman, 2008)

where γ_{SV} is the specific surface energy of the solid-vapor interface (pore/particle interface) and is approximately $x^2/2a$ when x/a is less than 0.3 (Kingery et al., 1976). The specific surface energy of this solid-vapor interface can be modified through selection of different process gases or using vacuum. In the present thesis vacuum was used to increase this value and thereby increase the rate of surface area reduction (Mackenzie & Shuttleworth, 1949). From these equations and with consideration of viscosity (η) and velocity of viscous flow, one can derive an equation for the initial neck growth:

$$\frac{X}{a} = \left(\frac{3\gamma_{SV}}{2\eta r}\right)^{1/2} t^{1/2} \quad (11)$$

Source: (Kuczynski, 1949; Rabinovich, 1985; Rahaman, 2008)

where r is the radius of curvature of the spherical particles. The viscosity is usually expressed using the Arrhenian equation:

$$\eta = \eta_o e^{E/RT} \quad (12)$$

Source: (Kuczynski, 1949; Pye et al., 2005)

where R is the gas constant, T the temperature and η_o and E are considered constants. However, since the activation energy (E) is not actually constant over

all temperatures, a new way of expressing the Arrhenian equation was developed by Vogel-Fulcher-Tamman, which by taking a natural log of both sides and redefining the activation energy (E) as a variable which changes with temperature (Pye et al., 2005; Shelby, 2005). Additionally, it defines a temperature, T_o, which affirms that the Arrhenian equation only holds true over a range of temperatures from the glass transition temperature to highly fluid melts (Pye et al., 2005; Shelby, 2005). The equation is as follows:

$$\ln(\eta) = -A + \frac{B*10^3}{T-T_o} \qquad (13)$$

Source: (Fulcher, 1925; Tamman, 1926; Vogel, 1921)

This equation can be used to fit data collected from a viscometer and allows accurate calculation of viscosity (η) at temperatures above T_g.

Once the radius of the neck reaches 40-50% of the sphere radius, through the mechanisms of viscous flow toward the neck, the system is said to be in the intermediate sintering stage and, at this stage, the pores are found to be interconnected. An idealized model is considered whereby the spherical pores have connected via necks to form long cylindrical structures and those structures form a cubic array [Figure 5] (Scherer, 1977). In this figure, *l* is the length of an individual cylindrical structure and *a* is the radius of the cylinder.

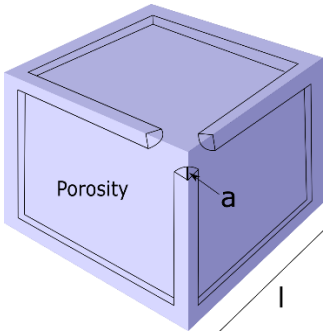

Figure 5. Sintering intermediate stage model

Source: Figure adapted by author from (Scherer, 1977)

In this model, the unit cell describing the porosity network is made up of an array of twelve quarter cylinders and the volume of the solid phase is:

$$V_S = 3\pi a^2 l - 8\sqrt{2a^3} \quad (14)$$

Source: (Scherer, 1977)

Therefore, with x defined as *a*/*l*, one can express the relative density:

$$\rho_{rel} = 3\pi x^2 - 8\sqrt{2}x^3 \quad (15)$$

Source: (Scherer, 1977)

where the relative density, ρ_{rel}, is equal to d/d_s or the ratio of density of the cell over the theoretical density of the solid and d equals $d_s V_s/l^3$ which are the density and volume of the solid divided by volume of the cell (l^3) (Rahaman, 2008). Using these equations and that the number of pores per unit volume (N) equals $1/\rho_o l_o$ where ρ_o

and l_o are the initial density and length, respectively, Frenkel was able to derive an equation for the densification of the system:

$$\int_{t_0}^{t} \frac{\gamma_{SV} N^{1/3}}{\eta} dt = \int_{x_o}^{x} \frac{2}{(3\pi - 8\sqrt{2}x)^{1/3} x^{2/3}} dx \quad (16)$$

Source: (Frenkel, 1945)

This idealized model suggests that if the viscosity for a given temperature, the number of pores per unit volume and the specific surface energy of the solid-vapor interface are known, one can derive the amount of time necessary to reach any given relative density. However, for the final stage of sintering, where density increases from 90% to 100% of full density, models of greater accuracy have been derived.

One such model is the one developed by Mackenzie and Shuttleworth (Mackenzie & Shuttleworth, 1949). In this model, a Newtonian fluid is assumed, and the rate of density change is expressed as:

$$\frac{\partial \rho}{\partial t} = \frac{3}{2}\left(\frac{4\pi}{3}\right)^{\frac{1}{3}} \frac{\gamma_{SV} N^{1/3}}{\eta} (1-\rho)^{\frac{2}{3}} \rho^{\frac{1}{3}} \left[1 - a\left(\frac{1}{\rho} - 1\right)^{\frac{1}{3}} ln\left\{\frac{1}{1-\rho}\right\}\right] \quad (17)$$

Source: (Mackenzie & Shuttleworth, 1949)

where:

$$a = \sqrt{2}\left(\frac{3}{4\pi}\right)^{1/3} \frac{\tau_C}{2\gamma_{SV} N^{1/3}} \quad (18)$$

Source: (Mackenzie & Shuttleworth, 1949)

with τ_C being the Bingham threshold. Further, McClelland suggested a simplified version of the Mackenzie and Shuttleworth model but taking into account the applied pressure (P):

$$\frac{\partial \rho}{\partial t} = \frac{3P}{4\eta}(1-\rho)\left(\frac{1}{1-(1-\rho)^{2/3}}\right) + \frac{\sqrt{2}\tau_C}{P} ln(1-\rho) \quad (19)$$

Source: (McClelland, 1961)

Therefore, given a known pressure, starting relative density and the Bingham threshold at the sintering temperature, a calculation of the amount of time to reach full densification can be made.

Sintering under pressure has the effect of significantly increasing the densification rate; it also may have the effect of increasing the nucleation and crystal growth rates (Uhlmann, Hays, & Turnbull, 1967). Therefore, post-process evaluation of crystallization of samples is necessary.

Particle size is known to play a role in the rate of densification of a powder and the smaller the particles are, the more rapid the densification occurs. This can lead to advantages such as the ability to decrease process temperatures (Rahaman, 2008). Smaller particles are however more prone to trapping of gases and contamination since the number of pores and total surface area is larger. Therefore, though the necessary process temperatures may be higher and densification rate slower, larger particles may still be preferable. A wide particle size distribution is also known to speed up the densification process by decreasing the size of pores in the starting green-body.

The choice of particle size also affects the crystallization behavior of the glass powder. As seen in Figure 5 a fine powder (< 100 µm) has an additional crystallization peak at ~500 ˚C which is not present in a coarse powder (100 – 250 µm) or the bulk glass. This additional peak is due to the increased surface area of fine powders which provides for additional nucleation sites. For reasons of carbon contamination and crystallization behavior a coarse powder should be used in sintering.

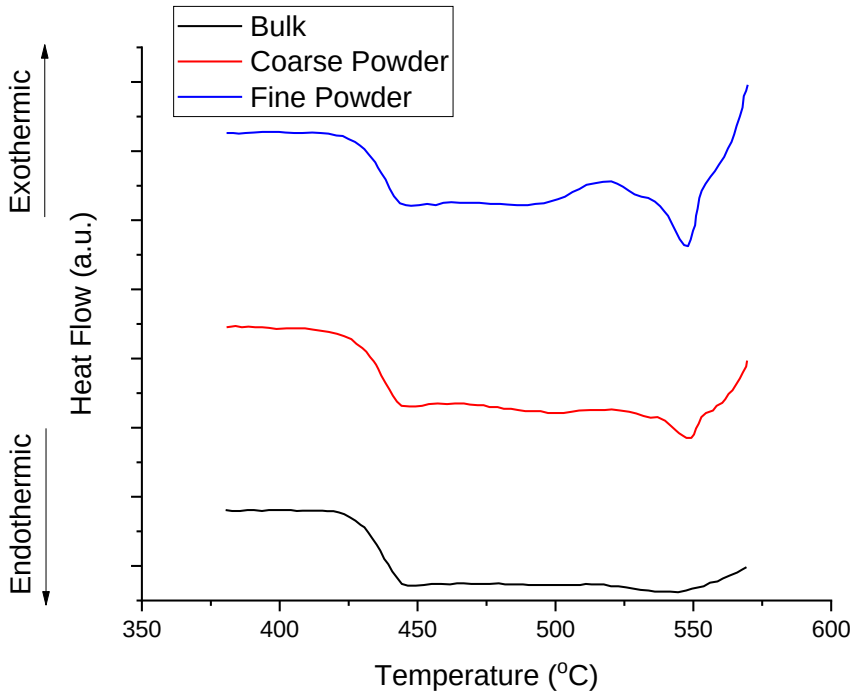

Figure 6. DSC of TWL glass powders and bulk glass (measurements made using 10 ˚C/min heating rate and unstated mass)

Source: Data from (Dohlen, 2018)

The primary method of sintering tellurite and TWL glass powder is a process known as spark plasma sintering.

Spark Plasma Sintering of TWL Glass

Spark plasma sintering (SPS) uses a pulsed DC power supply connected to a graphite die containing the sample powder. The die with the powder is enclosed

within a water-cooled vacuum chamber and pressure is applied onto the graphite die during the cycle to speed up the sintering process [Figure 7].

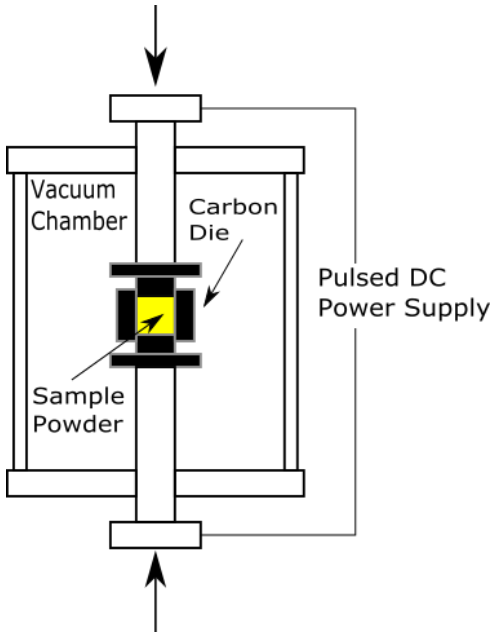

Figure 7. Diagram of a spark plasma sintering (SPS) device

Source: Figure adapted by author from (Bertrand, 2015)

In work done by Bertrand et al., on $85TeO_2$-$15WO_3$ (TW) it was identified that carbon was a key limiting factor in the optical transmission of SPS prepared glass (Bertrand et al., 2014). Carbon contamination was determined to increase in finer powders than in coarser powders and that the use of tantalum foil, alumina, and platinum diffusion barriers did little to reduce this contamination. Another researcher has suggested that the use of alumina did have the effect of decreasing carbon contamination in TWL glass but also decreased the pressure transferred

to the powder (Dohlen, 2018). Further, it was identified that the use of graphite dies was the primary cause of this contamination (Bertrand et al., 2014). It was also determined that finer powders would have homogenous dark brown coloration whereas coarse powders would have brownish coloration with dark spots and it was believed that a difference in the number of pores was the likely cause of this difference (Bertrand et al., 2014).

A study on the densification of TWL powder has been conducted by Dohlen (2018) using spark plasma sintering (SPS). The TWL powder was ground and sieved from a melt/quench prepared glass to select for course powder (100 – 250 µm) and fine powder (<100 µm). Each powder type was sintered at 450 ˚C for 1 minute under 50 MPa pressure and its transmission was compared to that of a parent reference glass [Figure 8]. SPS of fine and course powders led to high density glass compact but fine powder has greater loss at 3200 nm due to OH groups and the 400-1600 nm wavelength range which is attributable to light scattering.

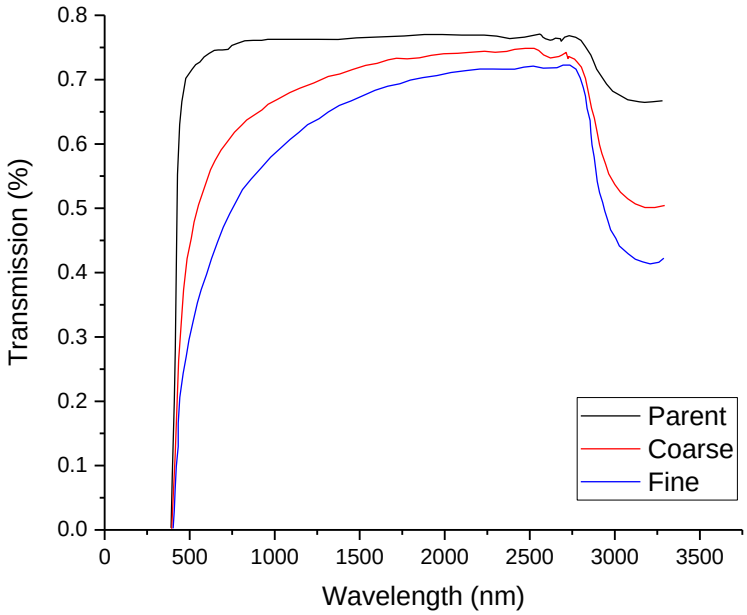

Figure 8. SPS comparison of fine and coarse powders (1.0 mm thick samples)

Source: Data from (Dohlen, 2018)

Dohlen (2018) (TWL glass) and Bertrand (2015) (TW glass) also observed that the sieving process leaves small submicron particles present on the surfaces of the coarse powder which have the effect of increasing carbon contamination during the sintering process. These were eliminated through a process of ultrasonic baths of ethanol and baking of the final powder. The effect this would have on powders when a graphite die was not used has not yet been determined and since ethanol is an organic compound, it may itself be a source of contamination. It was observed that in SPS sintering this process decreases carbon contamination (Bertrand, 2015; Dohlen, 2018).

Due to the high temperature operations of the sintering process and to the fact that nucleation and crystallization are found to occur more readily when subjected to pressure, the formation of crystals within the sintered body is also of concern. According to Dohlen (2018), small TWL powder compacts held at temperatures of 460 ˚C and 470 ˚C for 1 hour or 450 ˚C for 2 hours are found to lead to the formation of a $La_2Te_6O_{15}$ cubic crystalline phase.

Uniaxial Pressing of TWL Glass

Uniaxial hot pressing is a sintering process where a starting powder compact called the green-body is placed inside a die and through a combination of heat and single axis applied pressure the green-body is sintered into a densified compact [Figure 9, Figure 10]. The die body itself prevents the lateral displacement of the starting material and the applied pressure is applied over an unchanging cross-sectional area. The pressure is typically applied via a mechanical press and a resistive heater is used to heat the starting material.

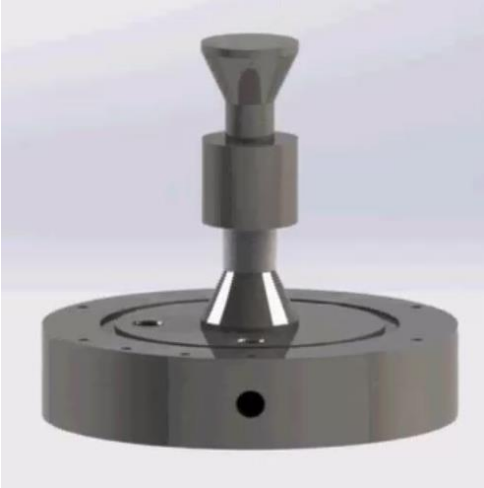

Figure 9. Representation of uniaxial steel die used in hot pressing shown mounted on a steel base

Figure 10. Representation of resistive heater surrounding a uniaxial steel die

A previous researcher working with hot pressing the same composition glass found that sintering at 450°C with 50 MPa applied for 12 minutes resulted in a fully

densified TWL sample (Roumiguier, 2016). During the sintering process, TWL glass adheres to the steel die and causes seizing of the die and problematic sample removal. In order to aid in the demolding of sintered TWL glass from the die this previous researcher experimented with the use of boron nitride coatings, aluminum foil and alumina powder (Roumiguier, 2016). Roumiguier's (2016) investigation found that though use of boron nitride coatings which aided in demolding they were still unable to extract intact samples. They then experimented with annealing the sample while still inside the die to attempt to relieve internal stresses in the sample. This coating and annealing work resulted in moderate size pieces being removed from the die but never resulted in achieving a fully intact sample.

Demolding of the TWL from the die and control of carbon contamination has been key challenges for the successful sintering of TWL glass to full density. It is known that TWL glass does not adhere to steel during quenching of the molten glass but repeated experiments by previous researchers have led to steel dies seizing and broken samples. Carbon contamination has been observed by past researchers as well and whether diffusion boundaries reduce this appears to still be an open question. Despite attempts to eliminate all carbon from the experimental design samples continued to be extracted that were darkened.

To address both the issue with seizing dies and with the intention of reducing carbon contamination, a method of using a sacrificial powder that encapsulates the sample powder was investigated.

Sacrificial Pressure-Transmitting Powder Sintering

The use of sacrificial pressure-transmitting powders to aid in the sintering process has been explored in many patents and papers (Ballard & Hendricks, 1966; Barbaras, 1969; Brennan, 1950; Googin & McLaughlin, 1966; Lange & Terwilliger, 1973; Lepp & Slyh, 1951; Manière et al., 2016; Wagner, 1960). Typically, a powder of flake graphite or ceramic is used for its characteristic of maintaining fluidity even at exceptionally high temperatures or pressures. These sacrificial powders act to allow pressure to be transmitted to the green-body or sample powder without the use of complex die configurations. By using cold pressing or a deformable barrier, contamination from the sacrificial powder can be avoided and the powder can be chosen to allow for ease of demolding. The use of a putty like mixture consisting of an alkali or alkali earth halide and oxide metals is reported to have been used as a sacrificial powder (Barbaras, 1969). This aided in demolding and allowed for a green-body or bodies to be sintered at high heat and pressure within a uniaxial hot press (Barbaras, 1969). The fused sacrificial powder was broken away from the sintered sample after the completion of hot pressing (Barbaras, 1969).

A later approach explored shape change and densification that was experienced during hot pressing when utilizing graphite and boron nitride powders (Lange & Terwilliger, 1973). It was found that at low densities the sacrificial powder would create isostatic conditions on the green-body but as densification of the sacrificial powder occurred the ability to transmit pressure to the green-body was hindered (Lange & Terwilliger, 1973). The resultant sintered bodies would be concave in shape owing to a decrease in transmitted pressure near the die walls (Lange & Terwilliger, 1973). However, it has been reported that should the medium be highly plastic at the sintering temperature little distortion would be observed in the sintered body (Barbaras, 1969).

An alkali halide, potassium chloride (KCl), was used as a sacrificial powder within a uniaxial hot press owing to its high plasticity at all temperatures below its melting point. The low melting point of 771˚C precludes its use for the sintering of many powders applicable to industry, such as steel, but is sufficiently high for use with many IR transparent optical ceramics. Additionally, it was thought that KCl could potentially form a carbon impervious layer that would be useful for future experiments with SPS.

Table 2 shows the objectives of this thesis with regards to sintering of TWL glass using a sacrificial pressure-transmitting powder in a uniaxial hot press. Each of these objectives will be addressed in the methodology section and the results

described. Many of these objectives are based upon sample comparison materials including a same composition glass and powder that was prepared via a melt/quench method.

Table 2. Desired attributes and potential setbacks in processing sintered TWL glass

Desired TWL Attribute	Potential Setbacks
>99.99 % Density of starting powder	Porosity, differing thermal history
Fully amorphous	Formation of crystallites
No detectable contamination from sacrificial powder	Presence of potassium or chlorine in the bulk or surfaces

In order to avoid the formation of crystallites within the glass during the sintering process an understanding of the glass' stability to devitrification must be understood.

TWL Glass Stability

When selecting a sintering dwell temperature that is above the T_g and below the liquidus temperature for the glass, temperatures higher than the lowest temperature crystallization region must be avoided or the dwell time must be kept to a minimum. A previous study of a glass of similar composition as TWL, $69TeO_2$-$23WO_3$-$8La_2O_3$, found that the glass did not show signs of crystallization at heating rates of 2.5, 5, and 10 ˚C/min. up to 650˚C (Dorofeev et al., 2011). This observation

is contradicted by Dohlen who observed that $70TeO_2$-$20WO_3$-$10La_2O_3$ glass shows a crystallization peak at ~550 ˚C but that an additional crystallization peak is present at ~500 ˚C for a powder with particle size <100 µm (Dohlen, 2018). It has been determined that this crystallization peak corresponds to $La_2Te_6O_{15}$ cubic phase which is heterogeneously formed (surface forming) (Dohlen, 2018). Therefore, by using a coarser particle size and operating at temperatures above the glass transition temperature but below ~550 °C, the devitrification of the glass can likely be avoided. When operating at these higher temperatures, and in a low oxygen atmosphere, the tungsten present within the glass may undergo reduction.

Reduction of Tungsten

In order to ensure pore collapse and avoid contamination in the TWL sample material during the sintering process, a vacuum environment is desired. In a low oxygen, high temperature sintering environment such as that created by the chosen sintering process here, W^{6+} from the WO_3 composition may undergo a reduction reaction. In the region of 500 °C to 575 °C the published reaction type is:

$$WO_{2.96} \rightarrow WO_{2.9} \rightarrow \beta - W \rightarrow \alpha - W \qquad (20)$$

Source: (Wilken et al., 1976)

The first stage of this reaction represents the reduction of W^{6+} to W^{5+} and W^{5+} to W^{4+} and is associated with a blue coloration change in an oxide glass (Leftheriotis et al., 2001; Sarin, 1975). This can be seen as a sample darkening and is easy to misidentify as a form of carbon contamination which leads to a browning of samples and has been observed in tungstate tellurite glasses prepared through SPS (Bertrand et al., 2014).

In a study done on WO_3 amorphous films by Leftheriotis et al., (2001), it was observed that reduction is observed in a vacuum environment when the film is annealed in increments of 100 ˚C for one hour each to 300 ˚C and that this reduction could not be fully reversed by oxidation within a high oxygen environment. The vacuum level used during this study was significantly higher than that used in the current research (Leftheriotis et al., 2001).

Since coloration change may be mis-attributed to tungsten reduction a quantitative test should be done to determine the source of any such change. Raman spectroscopy can be performed to determine if the tungsten-oxygen stretching modes are reduced in intensity in samples that are held at high temperatures in vacuum for various times. If the reduced intensity can be positively correlated with length of time in high heat and vacuum, then it can be determined that tungsten reduction can occur during the sintering experiments.

Based on this background and the processing constraints suggested to realize optically transparent glass from the sintering of glass powders, the experimental methods used in this thesis are explained in detail.

Methodology

Experimental Procedure

The sintering of TWL glass was conducted by forming a green-body of powder in a cold press, transferring the green-body to a uniaxial steel die and enclosing it into a custom designed sintering container. An external bottle press applies pressure onto the container during the heat-up, dwell and cool-down processes.

The sintering container used was an elastic and airtight container which consists of a machined stainless-steel base to which an iso-160 stainless steel vacuum bellow measuring approximately 150 mm tall and having an internal diameter of 150 mm. The bellow was attached to the base by iso-K single clamps, bolts and a silicone O-ring with centering ring. An iso-160 lid was attached to the top of the bellow with iso-K double clamps, bolts and a silicone O-ring with centering ring. This system was previously detailed by Shoulders, Locke and Gaume (2016) for use with air-sensitive materials.

The process of preparing a TWL green-body and sintering it to full densification is diagrammed in Figure 11. Below the diagram, each step is discussed in more detail.

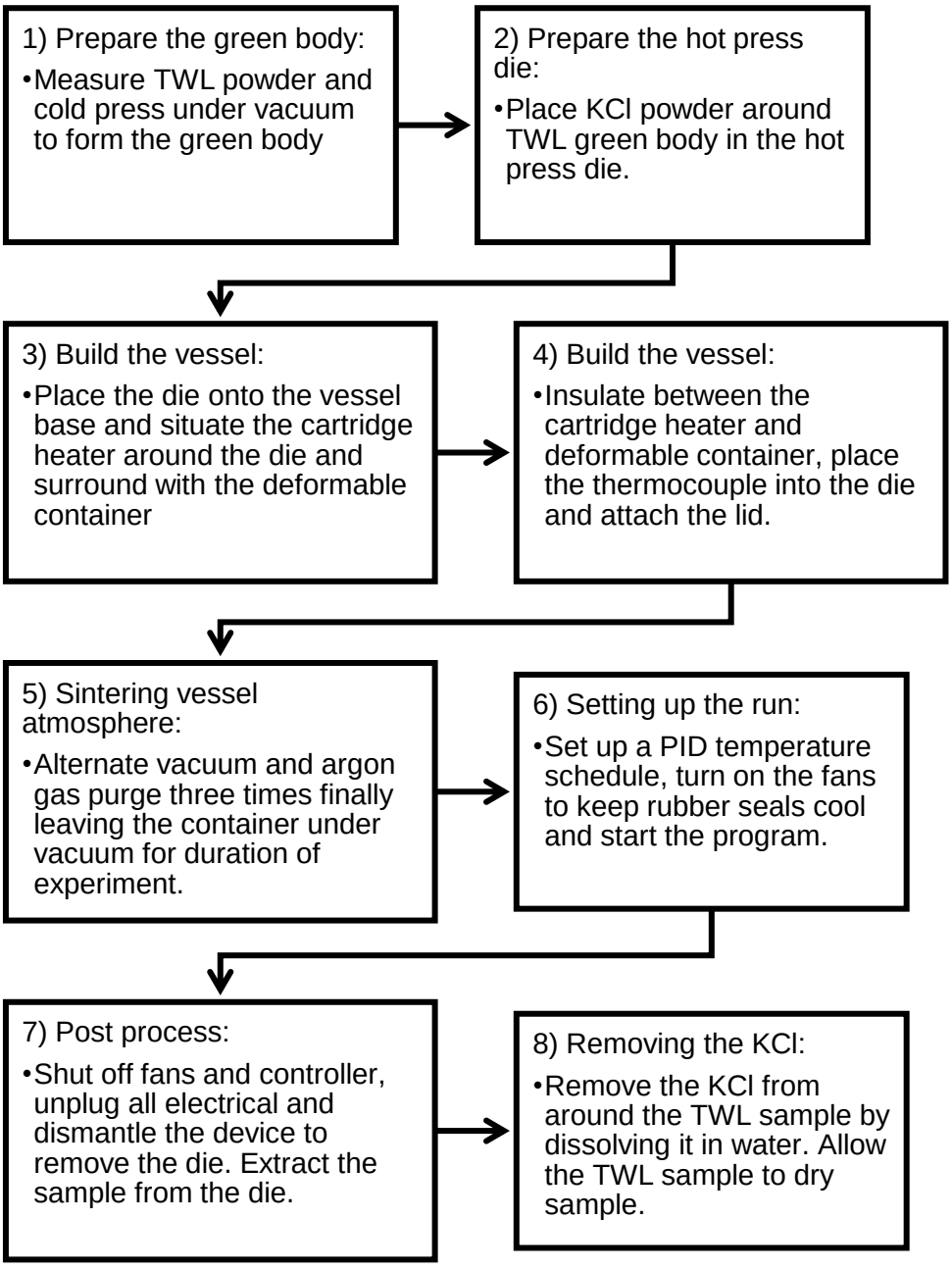

Figure 11. Hot uniaxial sintering procedure using sacrificial pressure-transmitting powder

1) $70TeO_2$-$20WO_3$-$10La_2O_3$ glass powder was supplied by the University of Limoges and prepared by a melt/quench process in a platinum crucible. An example of TWL glass prepared through melt/quench is shown in Figure 12. For sintering studies, the prepared glass was ground and sieved to have a 100-250 µm-sized grains [Figure 13] and stored within a nitrogen glovebox upon receipt.

Figure 12. $70TeO_2$-$20WO_3$-$10La_2O_3$ melt/quench sample

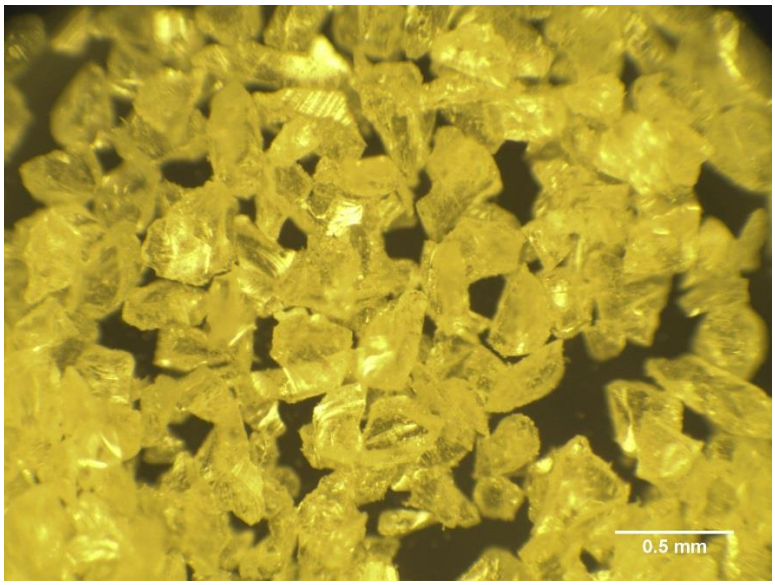

Figure 13. $70TeO_2$-$20WO_3$-$10La_2O_3$ 100-250 µm glass powder

1.00 g of powder was cold pressed inside a 13 mm die at rough vacuum (> 10^{-3} torr) [Figure 14] to form the green-body [Figure 15].

Figure 14. 13 mm diameter vacuum capable die used for cold pressing

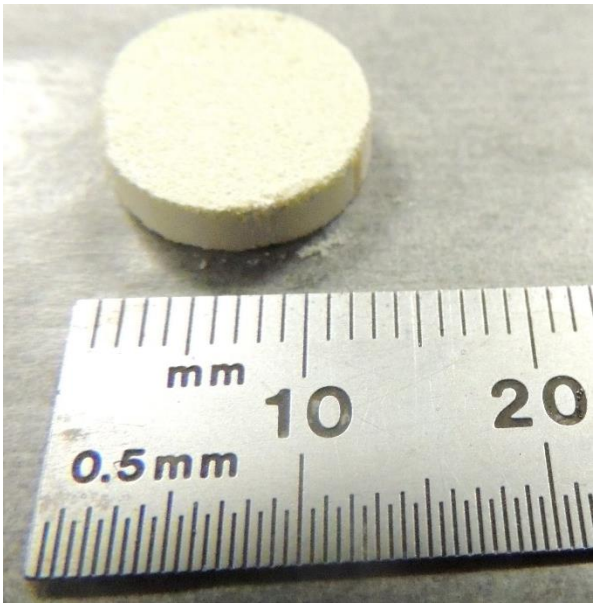

Figure 15. Green-body: cold pressed TWL powder (2.00 g shown)

2) The green-body was placed into a steel die [Figure 16] where it is surrounded by KCl powder that has been baked at 100°C to remove H_2O. The die consists of two plungers and sleeve and the sleeve has a hole for thermocouple placement.

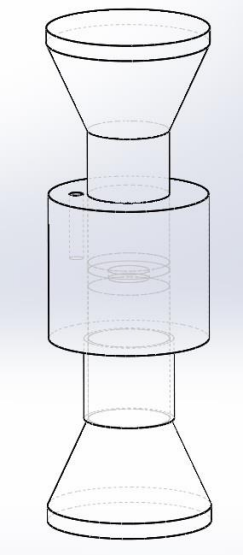

Figure 16. Hot pressing die

3) The steel die was placed onto an indentation in the base of the sintering vessel [Figure 17]. Then a cartridge heater was placed around the prepared die and a deformable container was attached to the base around the heater and die.

Figure 17. Base of the vacuum capable sintering vessel

4) Fiberfrax® insulation was placed between the deformable container and the cartridge heater and a K-type thermocouple was placed in a small hole in the body of the die that was close to the sample area. The lid was then attached to finish the construction of the vessel [Figure 18].

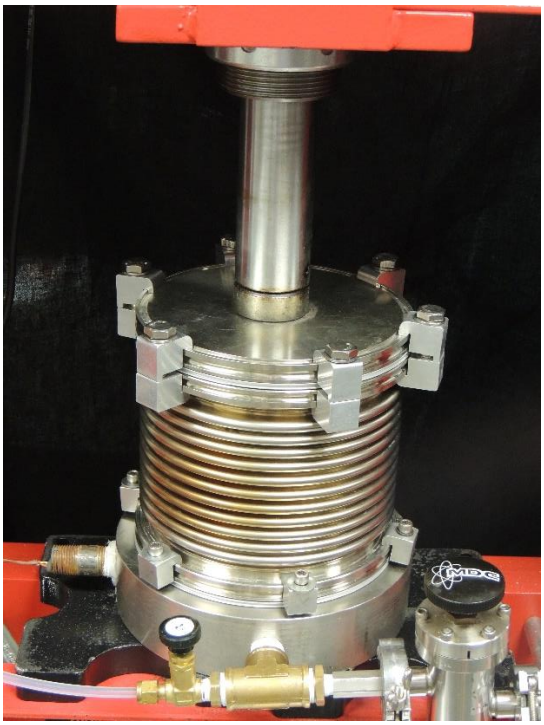

Figure 18. Vacuum capable sintering vessel

5) A rough vacuum (> 10^{-3} torr) was drawn on the vessel and then the vessel is filled with argon gas. This process is repeated three times before drawing vacuum and sustaining this state throughout the sintering process.

6) Two fans were set up to blow across the top and sides of the vessel to keep the silicone O-rings, located at the top and bottom of the deformable container, cool. Then the heater and thermocouple lines were connected to a PID (proportional-integral-derivative) controller [Figure 19]. A temperature schedule was programmed and ran on the controller to begin the sintering process.

Figure 19. PID controller

7) The dwell temperature was held for approximately 15 minutes and pressure was applied during this period. Then the pressure would be released, and the die allowed to cool. Upon the completion of the temperature schedule the fans, controller and vacuum pump are turned off and the device is dismantled to remove the die. The top plunger of the die was removed, and the bottom plunger was used to move the sample up and out of the sleeve.

8) The sintered sample now surrounded by densified KCl was then placed in a beaker of water to allow the KCl to dissolve. After a few rinses the sample was allowed to air dry within the beaker while covered with an aluminum foil.

The temperature within the die was measured using a thermocouple inserted within the sleeve of the die. This temperature has been found to be significantly different than the temperature at the center of the die where the sample was located. In order to estimate this temperature difference a die was built which matched the one used for experiments but with a hole drilled into the side of the

sleeve for insertion of a thermocouple into the sample space. The temperature measurements obtained from the side inserted thermocouple ($T_{sample\ space}$) was compared to those obtained from a thermocouple in the normal position (T_{sleeve}) and it was found that the two were related by the approximate relationship:

$$T_{sample\ space} = T_{sleeve} - 97 \quad (21)$$

Since the true relationship between the temperatures would depend upon heat up rate, dwell time and a multitude of other conditions which may change between experiments this thesis reports the temperatures recorded at the position of the sleeve but also shows the estimated “true” temperature within the sample space.

The TWL glass supplied by the University of Limoges was in the form of a coarse powder of 100 – 250 µm-sized particles. After quenching the melt between brass plates, the melt/quench glass was then crushed in an agate mortar and sieved with metallic sieves. This powder was packaged and sent to the University of Central Florida for use in experiments.

With an experimental method elaborated, the experimental conditions necessary to achieve full density need to be determined. The first step in this process was to determine the viscosity and model the densification rate of the powder compact.

Viscosity and Densification Modelling

In order to model the densification of TWL glass at a variety of temperatures a measure of the parent glass' viscosity was necessary. Viscosity measurements were done on TWL sample pieces using an Orton parallel plate viscometer (PPV) which is designed for automatic measurement of the viscosity of solid glass cylinders as a function of temperature using ASTM C-1351M procedure guidelines under an applied load of 305 g. The measured samples had dimensions of 6-12 mm in diameter and 6 mm thick.

These viscosity measurements were fitted using the Vogel-Fulcher-Tamman (VFT) equation:

$$\ln(\eta) = -A + \frac{B*10^3}{T-T_o} \quad (22)$$

Source: (Fulcher, 1925; Tamman, 1926; Vogel, 1921)

The results of the viscosity measurements were then utilized in the McClelland equation to model the densification of the powder compact:

$$\frac{\partial \rho}{\partial t} = \frac{3P}{4\eta}(1-\rho)\left(\frac{1}{1-(1-\rho)^{2/3}}\right) + \frac{\sqrt{2}\tau_C}{P} ln(1-\rho) \quad (23)$$

Source: (McClelland, 1961)

The yield stress for TWL glass has not been determined and has been estimated using data obtained for $78TeO_2$-$22WO_3$ glass by Churbanov et al., as shown in Figure 20.

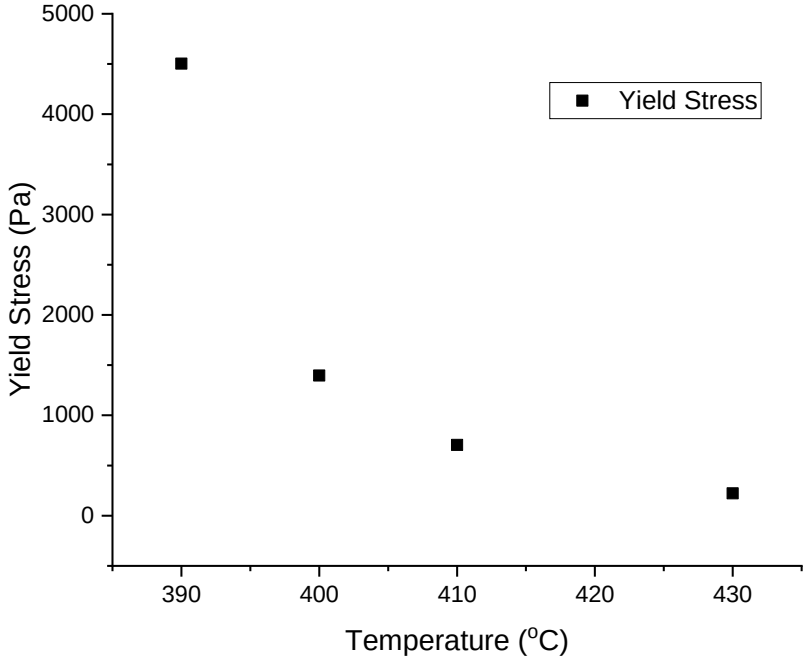

Figure 20. Yield stress of $78TeO_2$-$22WO_3$

Source: Data from (Churbanov, Snopatin, Shaposhnikov, Shabarov, & Plotnichenko, 2007)

Based on literature on the T_g of a similar composition glass, $75TeO_2$-$25WO_3$, of 370 ˚C the measurements at 390, 400, 410 and 430 ˚C can be interpreted as 20, 30, 40 and 60 ˚C above T_g (Dorofeev et al., 2011). A table of derived data for use in densification modelling has been found and is shown in Table 3. This data was

used as an estimate of the yield stress at similar values for TWL, with a T_g of 444.5 ˚C (10 ˚C/min. heat up rate), at values of 464.5, 474.5, 484.5 and 504.5 ˚C.

Table 3. Yield stresses for $75TeO_2$-$25WO_3$ glass

Temperature – T_g (˚C)	Yield Stress (Pa)
20	4504
30	1397
40	705
60	222

Source: (Dorofeev et al., 2011)

No analytical model exists for the description of a sacrificial pressure-transmitting powder surrounding a powder compact during densification. The McClellan model assumes a constant area during compaction which therefore implies that density and volume of the sample space are inversely related. This assumption does not hold true for a two-powder system where a complex interplay between differing densification rates and distortion of the powder compact occur. The McClellan model can however be used as a starting point in the optimization of experimental conditions. If the McClellan model predicts that experimental conditions are unreasonable for full densification of TWL alone then it would stand to reason that incorporation of a sacrificial pressure-transmitting powder would undoubtedly not lead to full densification.

Differential Scanning Calorimetry

The differential scanning calorimetry (DSC) measurements were done using a Netzsch DSC204 F1 Phoenix® device using aluminum pans with a temperature range of 30 °C to 590 °C and approximate sample mass of 20 g. DSC measurements was performed at three heating rates (2 ˚C/min, 5 ˚C/min and 10 ˚C/min) for a representative sintered sample and two melt/quench powders of same composition one which was “course” (100 – 250 µm particle size) and one which was “fine” (< 100 µm particle size). DSC measurements identify the glass transition temperature and the onsets of crystallization peaks and this information is used to design experimental parameters which allow for rapid densification of the powder compact (green-body) while avoiding crystal growth.

Temperatures corresponding to the glass transition temperature and exothermic peaks were extracted from these DSC measurements and used to calculate the activation energy of the glass transition (E_a) and crystallization (E_c). These calculations were performed using Kissinger’s formula:

$$\ln\left(\frac{\varphi}{T_m^2}\right) = -\frac{E}{RT_m} + C \qquad (24)$$

Source: (Kissinger, 1956)

where Φ is the heating rate, T_m is the temperature of the crystallization peak or glass transition temperature, R is the gas constant, E is the activation energy and C is a mathematically determined constant.

Densification along with other powder, powder compact and sintered sample features can be visually observed with an optical microscope.

Optical Microscopy

An optical microscope was used for initial analysis of samples. Despite the limitations of resolution, the optical microscope allows for rapid characterization of such features as particulate contamination, voids and secondary nucleation. In this work, a Nikon Labophot-2 optical microscope was used, and the pictures were taken using an Edmunds Optics EO-3112c camera. All sintered samples were polished before analysis.

Optical microscopy was used to see features in the TWL starting powder such as particle size, the presence of fine particles which have adhered to larger particles and the presence of surface level voids. Optical microscopy can also be used to observe neck growth in powders which are in the initial stage of sintering. Once the powder was fully densified into a compact a test of density could be used to determine the densification percentage:

$$densification\ \% = \frac{\rho_{experimental}}{\rho_{pre-sinter\ powder}} * 100\% \quad (25)$$

where the pre-sinter density is the density of the starting TWL powder used in the sintering experiments.

Density

Density measurements were made using Archimedes' principle with an Adam Equipment PW 254 analytical balance with an attached density kit. The samples were suspended in deionized water and the density as a function of temperature for the water was known. The measurements were done on post-processed samples where little to no porosity was observed.

With known deionized water density (ρ_{water}), the sample's mass can be measured in air and in water ($m_{sample,\ air}$ and $m_{sample,\ water}$) to find the density of the sample (ρ_{sample}):

$$\rho_{sample} = \rho_{water}\left(\frac{m_{sample,\ air}}{m_{sample,\ air} - m_{sample,\ water}}\right) \quad (26)$$

Since the overall goal of sintering was the densification of a powder into a compact the density measurement can be used to determine when full densification was being achieved.

In glasses, an increase in sample density can also be a sign of devitrification or changes in thermal history. In order to ensure that the samples have not crystallized, X-ray diffraction could be done on the samples.

X-Ray Diffraction

Due to the sintering dwell temperature which was known to exceed the glass transition temperature, nucleation and associated crystal growth become likely. In order to evaluate whether crystal growth has occurred X-ray diffraction (XRD) measurements were taken on a post sintered sample and the parent glass powder, both of which were crushed and sieved to select for <75 µm particle size. The XRD measurements were done with a Malvern PANalytical Empryrean with copper X-ray tube and the data is processed using Highscore software where background was removed, and K-alpha stripped from the data. The software was further used to scan the data for peaks and if found evaluate what crystal structures they correspond to.

According to experiments done at the University of Limoges a TWL glass powder held at 450 ˚C for over one hour will devitrify and a cubic phase of $La_2Te_6O_{15}$ will form (Dohlen, 2018). This $La_2Te_6O_{15}$ forming in tellurite glasses containing La_2O_3 is confirmed by Fujimoto et al., (2001) in their study of $BaO\text{-}La_2O\text{-}TeO_2$ glass heat

treated at 475 ˚C and is shown to form heterogeneously (on the surface) rather than homogeneously.

XRD is necessary before an index of refraction can be determined since the presence of crystallites will modify the measured refractive index. Since the goal was to have an optically transparent TWL glass formed after sintering this analysis can be used as a verification for the presence or absence of crystallites.

Refractive Index

After ensuring that the TWL sintered glass has not devitrified during processing index of refraction measurements can be performed. The index of refraction in the wavelength range of 0.24 – 1.7 µm was determined using a J.A. Woollam M-2000 ellipsometer. The data acquired is fitted using a Cauchy equation of the form:

$$n(\lambda) = A + \frac{B}{\lambda^2} + \frac{C}{\lambda^2} \qquad (27)$$

Additional index of refraction measurements were done using a Metricon 2010M system modified for use in the IR. A prism coupler employing a prism of GaP (refractive index = 3.0439 at 1.8 µm ((*"Optical Properties of Selected Inorganic and Organic Solids," in CRC Handbook of Chemistry and Physics*, 2018)) suitable for index measurements of media with indices between 1.9 and 2.6 was placed in contact with the sample of unknown refractive index through use of a pneumatic

piston. The two were rotated together to find the angle of total internal reflection at the interface and from this angle the index was calculated. The index of refraction of the material was measured twenty times at the following wavelengths: 1.880 µm, 3.300 µm, 4.000 µm, 4.515 µm, 5.252 µm, 7.968 µm and the prism index was calibrated using a ZnSe reference sample. A description of the sources used (vendor / model / type / wavelength range) are as follows:

M Squared / Firefly-IR-LP-A-BB-SI / optical parametric oscillator / 1.485 – 1.885 µm and 2.444 – 3.756 µm

M Squared / Firefly-IR-LP-B-BB-I / optical parametric oscillator / 3.246 – 4.617 µm

Thorlabs / QD5250CM1 / quantum cascade laser / 5.245 – 5.258 µm

Thorlabs / QD7950CM1 / quantum cascade laser / 7.958 – 7.979 µm

An average of the results having standard deviation no greater than 0.0006 was fitted using Sellmeier equations of the form:

$$\left(n(\lambda)\right)^2 = A + \frac{B^2 * \lambda^2}{\lambda^2 - C^2} \qquad (28)$$

where A, B, C, D, and E are determined through fitting of the data.

Due to size limitation of the sintered sample, ellipsometry data could not be acquired on the same TWL sintered sample. Thus, Fresnel losses in the 0.24 –

1.7 µm range were calculated from the index of refraction for the melt/quench glass. The index of both a sintered sample glass and melt/quench glass were measured with the prism coupler system and used to calculate the associated data across the 1.88 – 7.968 µm spectral range.

Once confirmed the ellipsometry and prism coupled data acquired for a TWL melt/quench glass was used to calculate and account for the Fresnel losses and to quantify the absorption coefficient for a sintered sample and the TWL melt/quench glass for comparison with previously reported literature values.

Transmission and Absorption

Ultraviolet-visible spectroscopy (UV-Vis) was performed using a Cary 500 system. Transmission measurements of the melt/quench glass and sintered sample were performed with the sample in the holder (T_{sample}), without the sample (T_{100}) and with the sample beam fully blocked (T_0). The transmission, T, is then calculated using:

$$T = \frac{T_{sample} - T_0}{T_{100} - T_0} \qquad (29)$$

The transmission in the NIR and MWIR was obtained using a Thermo Scientific Nicolet iS5 Fourier transform infrared spectroscopy (FTIR).

In the case of FTIR, to obtain the absorption coefficient of the samples the optical transmission was modeled with the assumption that the incident angle is negligibly small. A schematic of the incident, transmitted and reflected rays is shown in Figure 21.

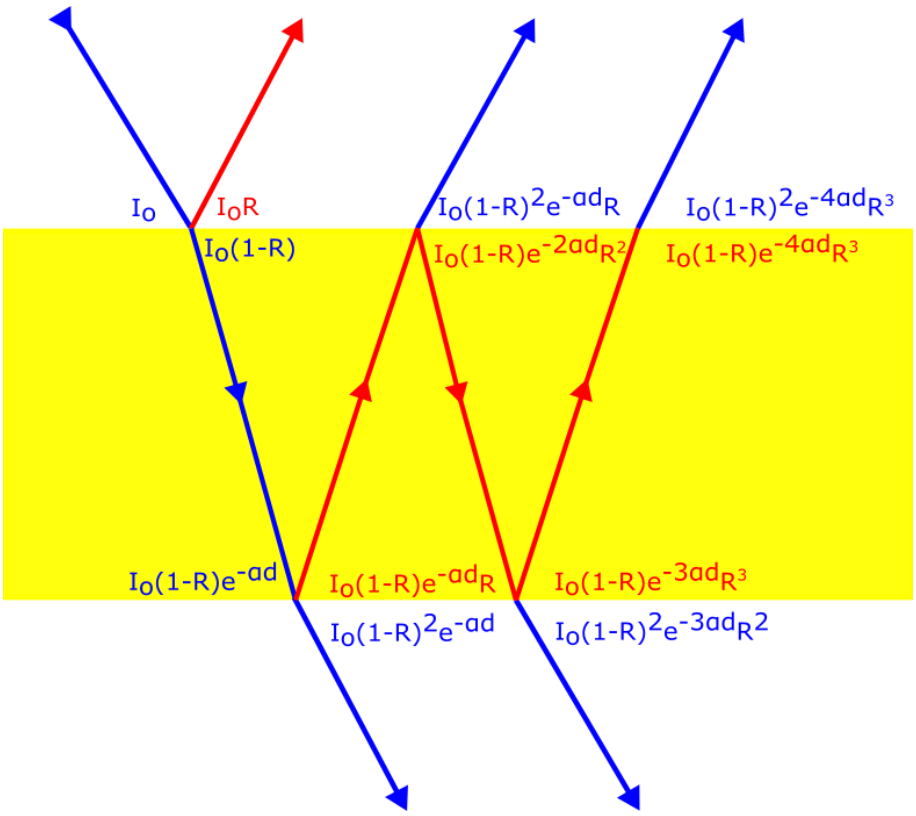

Figure 21. Transmission through a sample. Red arrows are reflected rays and blue arrows are transmitted. All incident angles exaggerated for illustration.

The light transmitted through the substrate can be expressed as:

$$T = (1-R)^2 e^{-\propto d}(1 + R^2 e^{-2\propto d} + R^4 e^{-4\propto d} + \cdots) \quad (30)$$

where T the transmission, R the reflection coefficient, α the absorption coefficient and d the sample thickness. Which simplifies to:

$$T = \frac{(1-R)^2 e^{-\propto d}}{1-R^2 e^{-2\propto d}} \quad (31)$$

Solving this equation for the exponential term, with use of the quadratic formula, and simplifying:

$$\propto = -\frac{1}{d} ln\left(\frac{-(1-R)^2 \pm \sqrt{(1-R)^4 + 4T^2R^2}}{2TR^2}\right) \quad (32)$$

The reflection coefficient is expressed as:

$$R = \left(\frac{n_{air} - n_{sample}(\lambda)}{n_{air} + n_{sample}(\lambda)}\right)^2 \quad (33)$$

where the n is the index of refraction which was assumed to be equal to 1 for air and was given by the experimentally determined Cauchy formula for the sample.

Therefore, the absorption coefficient was deduced from measuring the transmission spectrum, the index of refraction across the required spectrum and the sample thickness with calipers.

The index of refraction, and in turn transmission and absorption coefficient, may be impacted by the presence of potassium or chlorine contamination from the sacrificial pressure-transmitting powder. In order to account for this possibility

electron dispersive X-ray spectroscopy (EDS) was performed to determine if these contaminants are present.

Electron Dispersive X-ray Spectroscopy

Electron dispersive X-ray spectroscopy (EDS) was used to determine if potassium or chlorine are present within the sintered samples, either on the surface or in the bulk. EDS measurements were performed using a Zeiss ULTRA-55 FEG scanning electron microscope (SEM) equipped with Noran System 7 EDS. The EDS accelerating voltage was 15.0 kV with a takeoff angle of 35˚. The spectrum from a sintered sample was compared to that of a reference melt/quench sample that shares composition with the sintering starting powder. The reference spectrum is the average of five normalized spectra obtained at different locations from the top of the polished melt/quench sample. This reference spectrum was subtracted from the average of six spectra obtained from the cross section and the average of 11 spectra obtained from the top surface (closest to die plunger) of a polished sintered TWL sample. The area analyzed was from 1 to 10 keV which includes all potassium and chlorine peaks.

Another possible composition changes could come from the reduction of tungsten present within the glass composition. To determine if WO_3 reduction was occurring

in the samples, Raman spectroscopy was performed on samples that have been baked at high temperature while under rough vacuum.

Raman Spectroscopy

Two TWL glass samples were prepared for analysis using Raman spectroscopy to investigate post-processed glass structure (as compared to the parent glass) and to test if tungsten reduction was occurring within samples prepared in the sintering system. Additionally, these samples were investigated to look for TeO_2 and WO_3 crystallites. Each sample was pressed at room temperature into a green-body and placed into a die surrounded by KCl powder. This die was then heated at a rate of 18 °C/min to a dwell temperature of 550°C (estimated true temperature of 455 °C) all while under rough vacuum to match the atmospheric conditions of all the other sintering experiments. One sample was held at this dwell temperature for 30 minutes and the other for 120 minutes. These times were chosen such that they exceed the dwell times in the standard sintering experiments. After sintering, these samples were cooled within the device then placed within DI water overnight to remove KCl. Once soaking was complete, the samples were dried before analysis was conducted.

The pre-sintered powder, 30- and 120-minute dwell samples were all characterized using a Bruker Senterra Raman spectrometer with 785 nm laser at 100 mW

through a 20X objective. These spectra were deconvolved using mathematical fitting in OriginLab and compared to each other. It is expected that the tungsten modes at 362 cm^{-1} and 924 cm^{-1} decrease in amplitude if reduction is occurring.

Though the samples for the Raman study were not polished to allow for the possibility of reduction occurring only in the surface layers, polishing is necessary for any analysis of transmission, index of refraction and at times when inspecting the sample under optical microscope. In the next section, the technique for polishing the TWL sintered samples is detailed.

Polishing

In order to ensure near parallelism between the faces of the samples and decrease the amount of light scattering caused by surface defects, polishing of the sintered samples was necessary. Polishing of sintered samples was done using an Allied Multiprep Polishing System 8” with 320, 600, 800, 1200 grit SiC paper and a variety of final polishing techniques including 1 μm alumina and diamond solutions. Additionally, the removal of the relatively rough top layers of the samples was often necessary to characterize the samples under optical microscope.

Results

For this thesis four samples sintered with the sacrificial pressure-transmitting approach to hot pressing were prepared and analyzed using the tools and methods described in the previous section. The experimental conditions used in the preparation of these samples is summarized in Table 4 where the estimated true temperature is based upon the method as outlined in the Experimental Procedure section. As can be seen in the photos shown in Figure 22, Figure 23, Figure 24 and Figure 25 these samples all have dark inclusions caused by some form of contamination within the glass and are in pieces of various sizes due to the need to mechanically separate them from the die plungers and sleeve during sample removal. The ability to remove the samples has been greatly aided by the KCl powder but as can be seen, while improved, the removal did not result in perfectly intact parts. The top surfaces of the samples are rough and appear imprinted by the KCl powder and the material itself is white in color until polishing occurs. The white color is the same as small particle sized TWL powder and not an indication of KCl contamination. In general, the yellow coloration of the bulk appears darker than that of the parent glass indicating a loss in transparency in the visible.

Table 4. Samples characterized

Sample Name	Heat Up Rate (°C/min.)	Dwell Temp. (°C)	Est. True Temp (°C)	Dwell Time (min.)	Applied Pressure (Mpa)
Sample 1	10	580	485	10	35
Sample 2	10	605	505	30	88 (for 15 min.)
Sample 3	8	570	475	18	53
Sample 4	18	565 – 585	470 – 490	10	53

Figure 22. Photograph of sample 1

Figure 23. Photograph of sample 2 with top right piece polished on one side

Figure 24. Sample 3 with one piece single sided polished

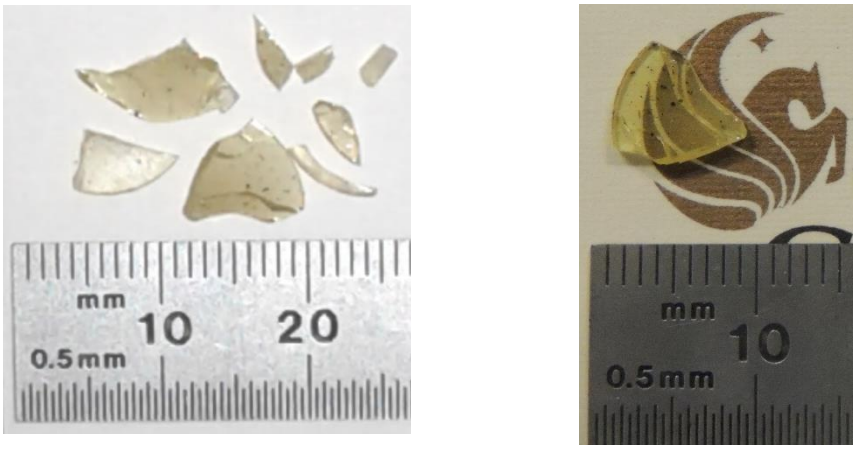

Figure 25. Sample 4 with one piece polished

The experimental methods used on these glasses was compared to the densification models to see if the model predicts full densification under the stated conditions.

Viscosity and Densification Modelling

Using the protocol discussed above, the viscosity of TWL glass was measured on four different parent glass samples prepared by the melt/quench process at Limoges. Figure 26 shows the average of these four measurements fitted with the Vogel-Fulcher-Tamman (VFT) equation.

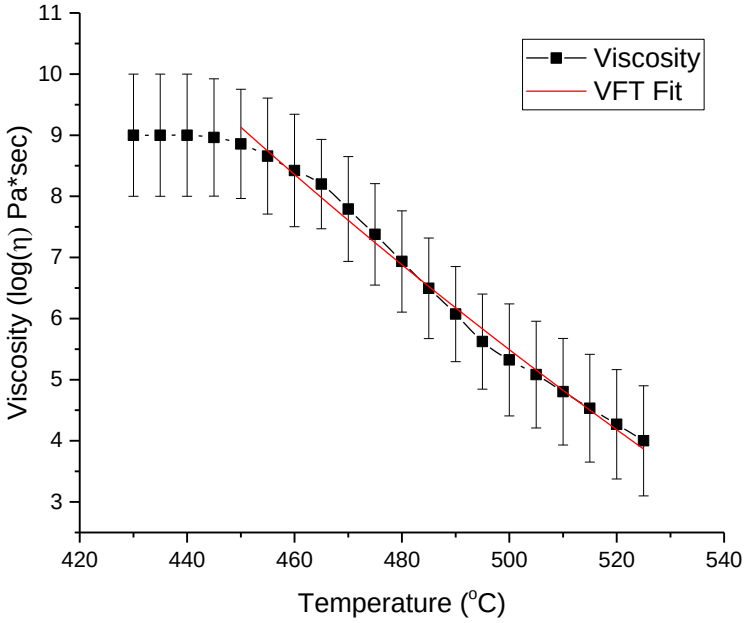

Figure 26. Viscosity of TWL glass fitted with VFT equation (errors bars based on mathematical error between measurements)

Source: Measurements courtesy of Dr. Anupama Yadav

The VFT equation for these measurements was found to be

$$\log(\eta) = -40.26 + \frac{31.05*10^3}{T+178.70} \quad (34)$$

Using this equation viscosity values can be calculated and used in the McCelland model to predict the densification kinetics.

In addition to the inherent assumptions in the model the following assumptions were made:

1) Fitted VFT equation gives a reasonable estimate of viscosity at experimental temperature values where measurements were not performed.

2) Yield stress of TWL glass is equal to the values for $75TeO_2$-$25WO_3$ glass for equivalent temperatures above its respective T_g.

Numerical evaluations of different densification kinetics for varying temperatures pressures were modeled and an example of varying pressure at a constant 464.5 °C is shown in Figure 27. A plot showing the effect of temperature and pressure on densification time is shown in Figure 28.

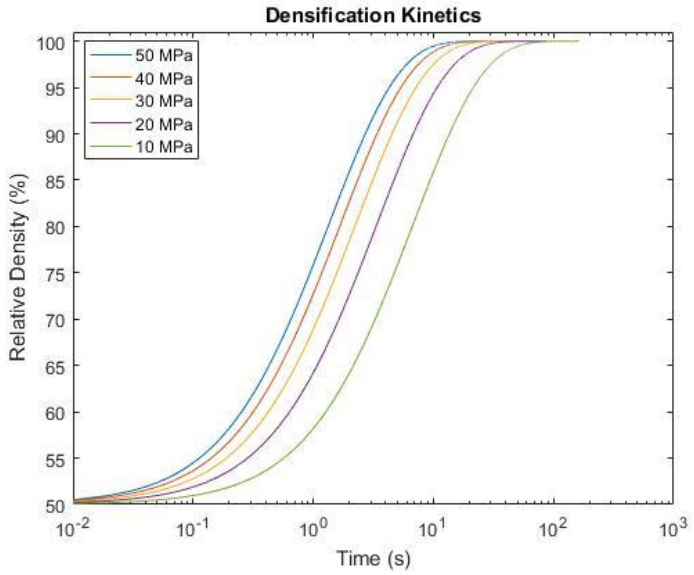

Figure 27. Densification kinetics at 464.5 ˚C and varied pressure

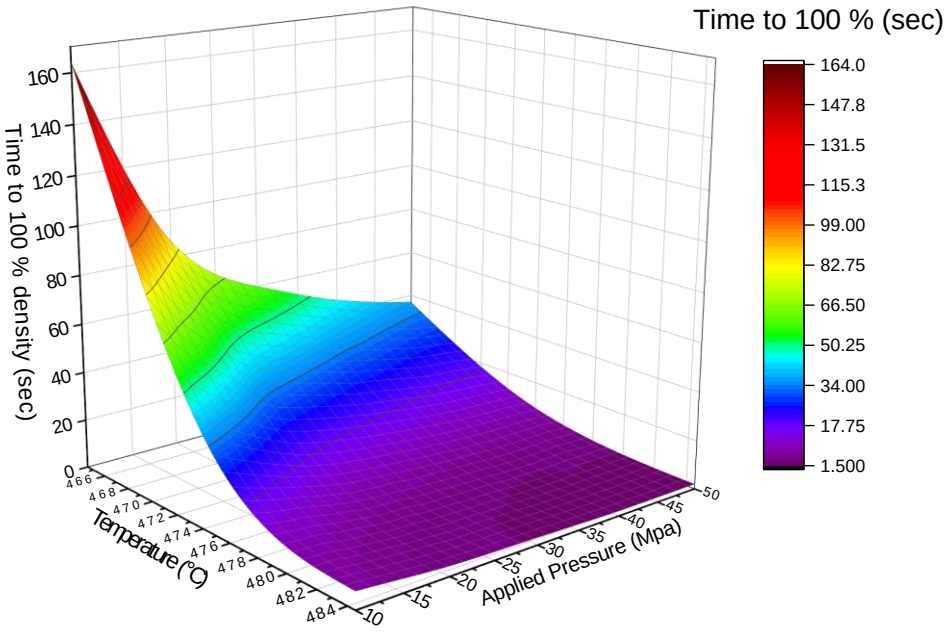

Figure 28. Effect of temperature and pressure on time to 100 % density

These results show that without the use of a sacrificial powder, sintering to 100 % of theoretical density is possible in under 170 seconds at temperatures from $>T_g$ + 20 ˚C and applied pressures greater than 10 MPa. It was expected that with the use of the sacrificial powder the applied pressure upon the green-body would be reduced due to particle-particle interactions.

This model is however built upon a number of assumptions and amongst these assumptions is constant cross-sectional area which does not apply to a two-powder system. Despite this limitation, it was determined that the experimental conditions used to sinter samples 1 – 4 as stated in Table 4 would be likely to result in densification of the powder compact to > 99.99 % of the melt/quench glass (fully densified).

Another factor to consider in building these experiments was that, at temperatures above T_g, the TWL glass may devitrify resulting in a glass-ceramic rather than the desired glass. Additionally, the sintering process may modify the thermal properties of the glass resulting in a less stable material. Determining the glass transition (T_g), crystallization onsets (T_x) and stability $\Delta T = T_x - T_g$ can be done with differential scanning calorimetry (DSC)

Differential Scanning Calorimetry and Differential Thermal Analysis

Differential scanning calorimetry was done on glass powder derived from a parent melt/quench glass (pre-sintered TWL powder) with two different particles sizes, fine which is < 100 µm and course which is 100 – 250 µm, and post-sintered powder derived from sample 4 at 2/5/10 °C/min heat up are shown in Figure 29, Figure 30 and Figure 31 respectively and the results are summarized in Table 5. The parent-coarse and parent-fine glasses are same composition glasses as that used in the sintering process. In the parent-coarse (melt/quench) glass a secondary lower temperature crystallization peak does not appear except in slow DSC heating rates and appears at 506.4 °C at 2 °C/min. This secondary lower temperature crystallization peak appears at all three heating rates in the parent-fine powder. This crystallization is due to $La_2Te_6O_{15}$ crystal formation, which is known to be heterogeneous (surface-forming).

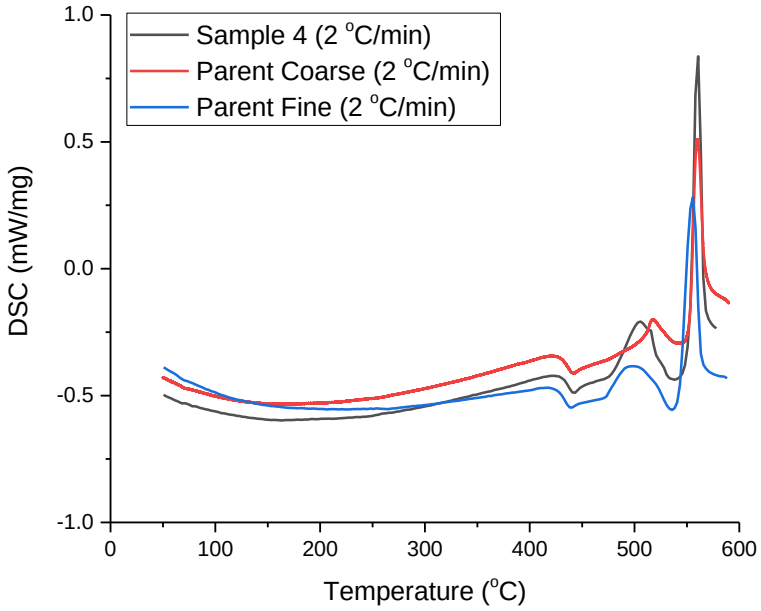

Figure 29. Differential scanning calorimetry (2 ˚C/min)

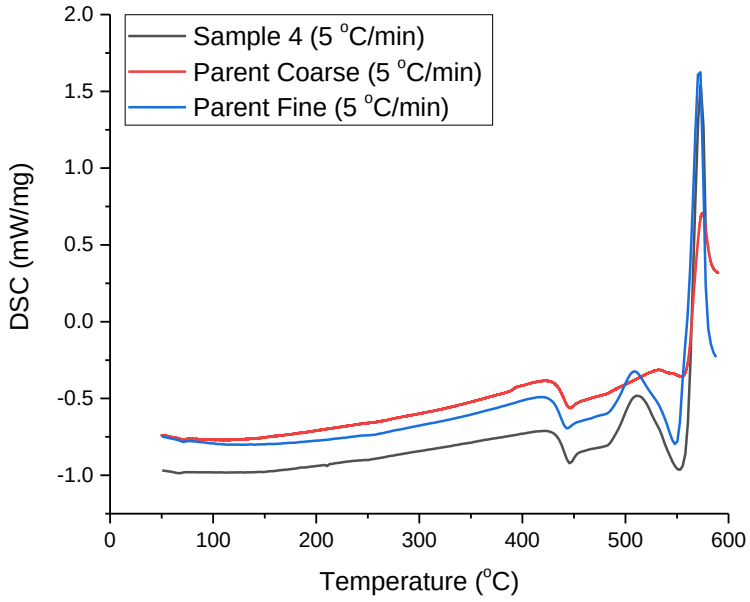

Figure 30. Differential scanning calorimetry (5 ˚C/min)

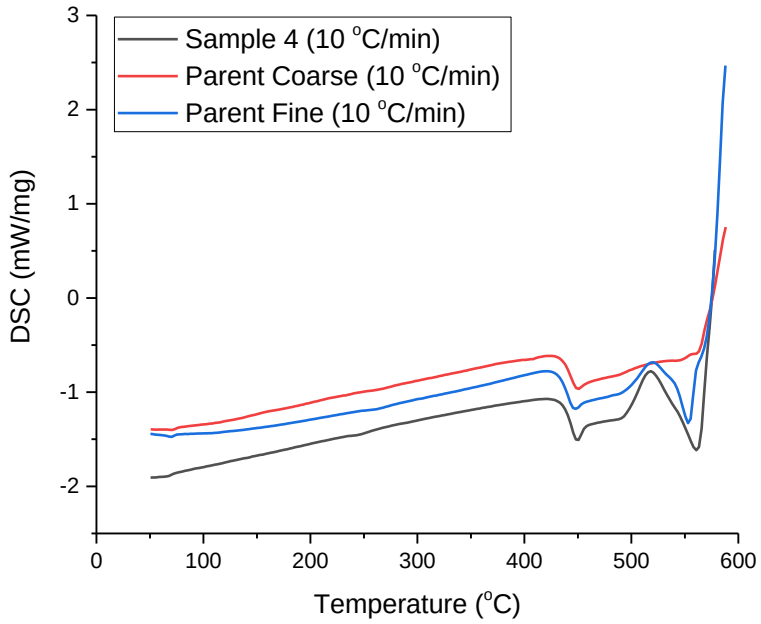

Figure 31. Differential scanning calorimetry (10 ˚C/min)

Table 5. T_g, T_{x1} and T_{x2} data from sintered and parent TWL glass at 2/5/10 ˚C/min. heating rates.

Sample Type	Heating Rate	Mass (mg)	T_g (°C)	T_{x1} (°C)	T_{x2} (°C)
Sample 4	2 ˚C/min.	20.0	432.3	479	553.2
Sample 4	5 ˚C/min.	20.7	442.3	487.5	560.0
Sample 4	10 ˚C/min.	19.9	443.4	495.4	570.5
Parent-Coarse	2 ˚C/min.	21.5	431.3	506.4	552.8
Parent-Coarse	5 ˚C/min.	24.7	441.0	Not Resolved	560.3
Parent-Coarse	10 ˚C/min.	22.2	444.5	Not Resolved	567.7
Parent-Fine	2 ˚C/min.	20.7	434.4	479.9	543.1
Parent-Fine	5 ˚C/min.	22.7	434.8	489.7	555.4
Parent-Fine	10 ˚C/min.	21.8	439.7	491.6	576.1

Previous researchers have conducted DSC measurements on glasses of similar compositions and their observations are well in line with the glass behavior observed in this study (Dohlen, 2018; Dorofeev et al., 2011; Kut'in, Plekhovich, & Dorofeev, 2016). Based on their past research, it appears that increased crystallization behavior of the TWL sintered glass, sourced from sample 4, is likely due to a difference in surface defects coming from the particle size analyzed. The sample 4 material was crushed into powder for analysis but was not sieved to select for a particular powder size, thus suggesting that it had broader size distribution, which would impact the surface area ranges available for subsequent heterogeneous crystallization to initiate. Based upon visual observation, the sample 4 crushed glass appears to have a particle size significantly smaller than the 100 – 250 μm powder identified as the parent glass. Since these crystallization peaks are identified as likely coming from heterogeneous (surface) crystal growth, the smaller particle size would cause them to be more pronounced owing to the increased surface area in the material. The glass transition temperature has been shown to vary by 1 – 2 °C between the sintered and unsintered glass coarse-powder and this small variation suggests that little to no compositional change has occurred within the material. The significant glass transition temperature difference between the parent-fine and sintered glass suggest that a small composition difference exists between two.

From these graphs, the temperatures where the glass transition and crystallization peaks occur was obtained and using Kissinger's equation, the activation energy of these processes can be calculated [Table 6] (Kissinger, 1956). That the activation energy is higher for the second crystallization exothermic peaks suggests that the sample 4 has stronger bonds owing to its smaller free volume, a conclusion supported by the density measurements.

Table 6. Activation energy for the glass transition temperature (E_a) and the first and second crystallizations (E_{c1} and E_{c2} respectively)

Sample Type	E_a (kJ/mol)	E_{c1} (kJ/mol)	E_{c2} (kJ/mol)
Sample 4	288	691	314
Parent-Coarse	287	Not Resolved	264
Parent-Fine	537	317	224

The effect of temperature can also be observed under the microscope where the sintering stages can be visually seen, and the experimental procedure can be modified based on these findings.

Optical Microscopy

The starting TWL glass powder for the sintering experiments was a 100 – 250 µm powder that is obtained by crushing and sieving a bulk melt/quench glass Figure 32. This powder was reported to contain small <1 µm particles which are attached to the surface (Bertrand et al., 2014; Dohlen, 2018). Under microscope, these small particles are evident on the surfaces as shown in Figure 33. Previous researchers have suspected that the elimination of these fine surface particles could decrease the carbon contamination found within the sintered samples (Bertrand et al., 2014). It is however also known that wider particle distributions and finer particles tend to aid in green-body densification and since the current setup has limited carbon sources the decision to not eliminate these was made.

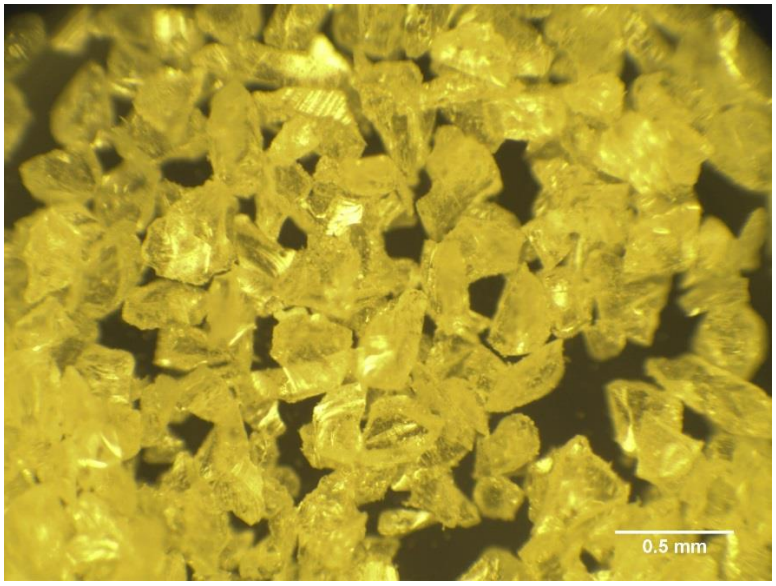

Figure 32. TWL glass powder

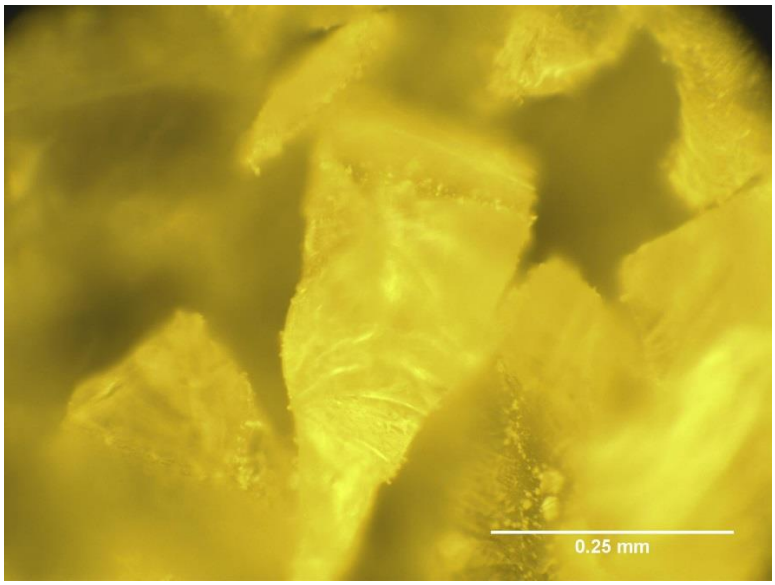

Figure 33. TWL glass powder showing the presence of small surface affixed particles

The ability of this powder to be sintered is confirmed in an experiment where a 1.00 g green-body is held at 550 °C (true temp. 455 °C) for 2 hours. The formation of necks can be seen between the individual grains indicating the compact is progressing through the initial stage of the sintering process [Figure 34 and Figure 35].

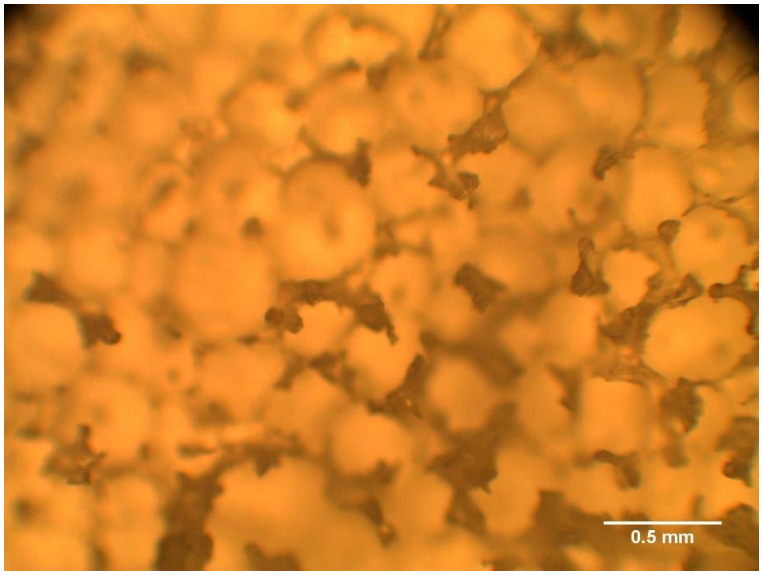

Figure 34. TWL densification after 2 hours without pressure

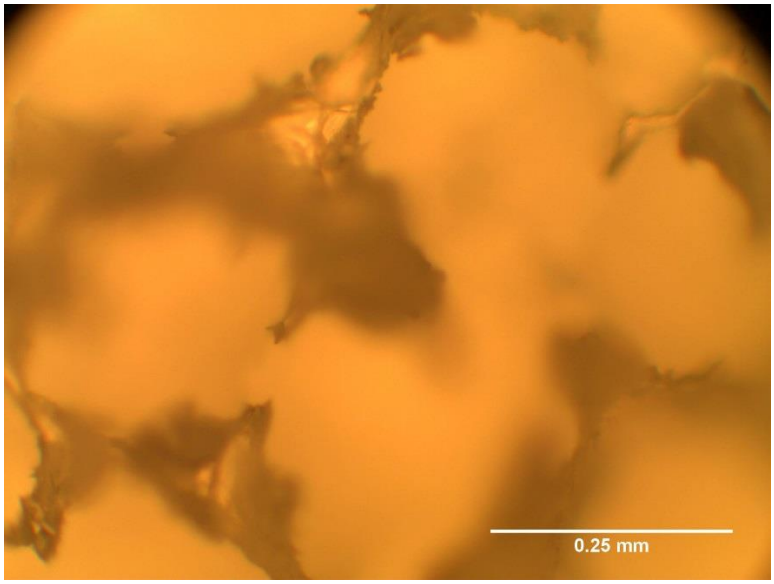

Figure 35. Closer detail of neck formation in TWL densification after 2 hours without pressure

The application of pressure greatly accelerates the sintering process. Sample four as shown in Figure 36 shows that the boundaries between individual powder grains are still evident yet nearly full densification has occurred. The dark patches between the connected particles are some form of contamination and are similar to the observations of carbon contamination that researchers working on spark plasma sintering of TWL have observed (Bertrand et al., 2014; Dohlen, 2018).

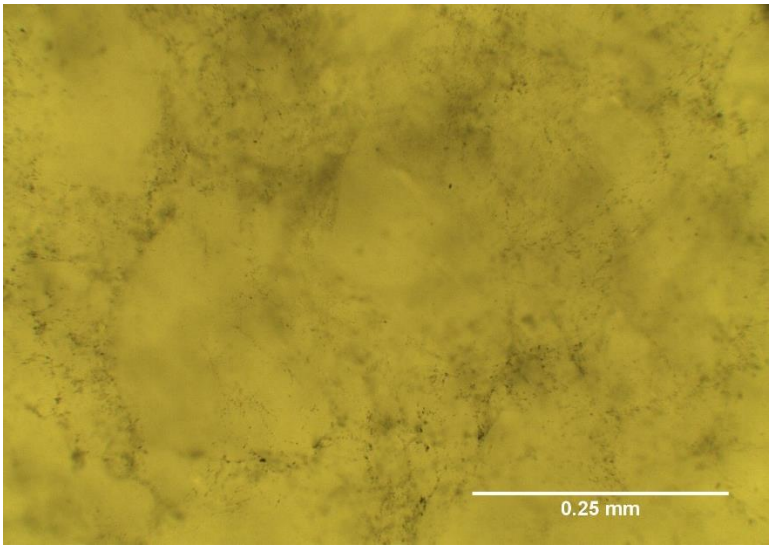

Figure 36. Microscope image of sample 4

In order to determine if full densification has occurred in the samples, the density was measured using an Archimedes' approach.

Density

Full densification in a sintered ceramic is typically defined as 97 % of the theoretical maximum but this definition is insufficient for an optical glass where the presence of open pores would negatively impact transmission. The density of glasses is also highly dependent on thermal history and changes in density do not necessarily indicate the presence of pores but rather could be the result of differences in free volume. With this limitation in mind a goal of achieving a 99.99 % density of the sintered samples when compared to the base powder is proposed.

The density of the TWL powder which is used as the base material for the sintering experiments has been compared to that of the four sample glasses and is shown in Table 7 along with the density of the melt/quench glass which was used for comparison in transmission, absorption and index of refraction measurements.

Table 7. Density comparison of melt/quench glass

Sample Name	Density (g/cc)	$\frac{\rho_{\text{sample}}}{\rho_{\text{pre-sinter powder}}}$
Melt/Quench Glass	6.40 ± 0.03	N/A
Pre-Sinter Powder	5.96 ± 0.02	N/A
Sample 1	6.05 ± 0.06	102. %
Sample 2	5.99 ± 0.04	101. %
Sample 3	6.12 ± 0.02	103. %
Sample 4	6.51 ± 0.05	109. %

Source: Density values on pre-sintered powder courtesy of the University of Limoges SPCTS

The densities of samples 1 – 4 indicate that the applied pressure and differing thermal history the material experiences during the sintering process, increases the density of the material above that of the starting powder. Based on the density of the pre-sintered powder of 5.96 g/cm^3 compared to the density of the same composition melt/quench glass of 6.40 g/cm^3, the increased density of the sintered samples 1 – 4 is within expectation without need to appeal to a compositional change. The pre-sinter powder and melt/quench glass likely have differing densities due to batch size and therefore differing thermal histories but this information is not known.

The most likely crystallite that would form at the operating temperatures is the $La_2Te_6O_{15}$ which has a density of 5.77 g/cm^3 ("La2Te6O15 (La0.25Te0.75O1.875) crystal structure: Datasheet from "pauling file multinaries edition – 2012" in

Springer Materials," 2012) and therefore its formation would cause a resulting decrease in the density of the material. However, none of the measured sample densities show such a decrease. There is no correlation between density and dwell time, dwell temperature or applied pressure. The sintered glass was however cooled from above T_g by blowing fans over the surface of the sintering vessel until the sample space reaches room temperature and this slow cool down rate explains the increased density above that of the pre-sintered powder which was cooled via quenching between brass plates. It is well known that fast-cooled glass has a lower density owing to its increased volume (Varshneya, 1994). The wide variability of the density of the pre-sinter powder versus the same composition melt/quench glass is likely due to the lack of an annealing process in the powder.

Differences in density can also be caused by crystallization since crystallites have a different density than that of an amorphous glass. The density measurements do not suggest the presence of the most likely crystal structure, cubic $La_2Te_6O_{15}$, but in order to further rule out this possibility sample 4 was studied with X-ray diffraction.

X-Ray Diffraction

In order to eliminate crystallization as an explanation for the increased density in sintered samples, X-ray diffraction (XRD) was done on the highest density sample (sample 4) and compared to the parent glass powder (Figure 37).

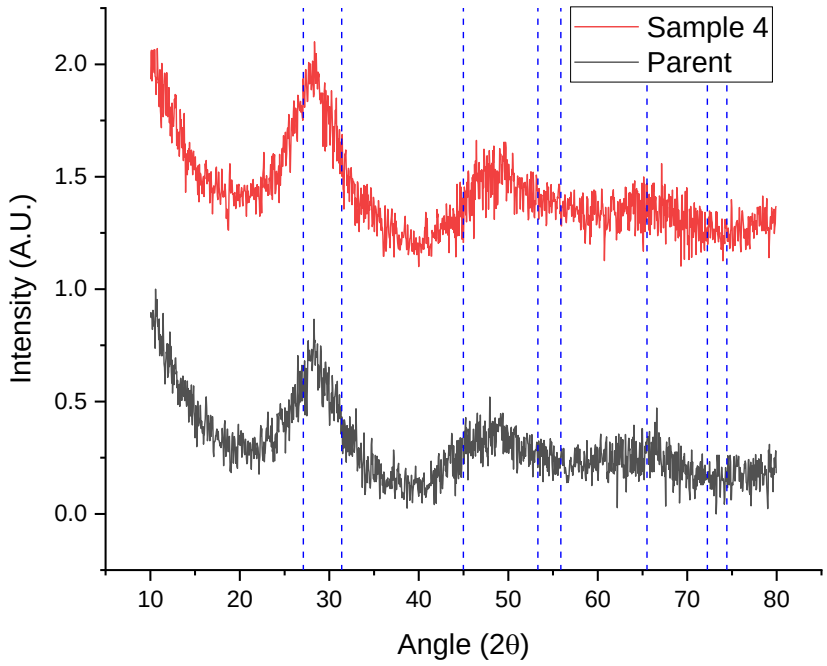

Figure 37. X-ray diffraction of powder sintered sample 4 and parent glass with particle size <75 µm. Drop lines have been added to denote the location of where $La_2Te_6O_{15}$ peaks would be if present

The XRD pattern of sample 4 reveals that detectable crystallization did not occur. It was anticipated that sintering at above T_g would possibly result in the formation of $La_2Te_6O_{15}$ (Dohlen, 2018; Fujimoto et al., 2001). Fujimoto et al., (2001)

observed that $La_2Te_6O_{15}$ formed in a $15BaO\text{-}15La_2O_3\text{-}70TeO_2$ glass that was heat treated for 5 hours at 475 °C (T_g was reported as 474 °C) and was found only in the first 15 µm of the sample. Because polishing was done on sample 4 and an unknown amount was removed, it cannot be determined if surface crystallization occurred. In addition, it is possible that a small amount of crystallization below the detectable limit for the analysis may have formed and based on the temperatures used it seems likely. Formation of nuclei within the glass cannot be determined by XRD and remains a possibility.

Knowing that crystallization is not present or minimal in the sample, measurements of the index of refraction can be made and those measurements used to determine the absorption coefficient from transmission spectra.

Index of Refraction

Base glass and post-process sintered TWL were evaluated to quantify their respective refractive indices through the short and mid-wave spectral region. As the methods rely on different assumptions and their data are subsequently fit to match the measured values, this fitting results in wavelength dependent equations which define refractive index at wavelengths where discrete measurements (such as in the case of refractometry via the Metricon system) were not performed.

The index of refraction as measured by ellipsometry for the TWL melt/quench glass in the range of 0.24 to 1.7 μm can be expressed by:

$$n(\lambda) = 2.028 + \frac{0.03097}{\lambda^2} + \frac{0.00015898}{\lambda^2} \quad (35)$$

where the wavelength (λ) is in microns.

The index of refraction as measured by the prism–coupler method for the TWL melt/quench glass over the range of 1.88 – 7.968 μm can be determined using the Sellmeier relationship:

$$n^2 = 4.59035 + \left(\frac{2.59245^2 * \lambda^2}{\lambda^2 - 19.8026^2}\right) \quad (36)$$

The index of refraction as measured by the prism-coupler method for TWL sintered sample four in the same spectral range is:

$$n^2 = 4.5421 + \left(\frac{2.78466^2 * \lambda^2}{\lambda^2 - 21.10078^2}\right) \quad (37)$$

As shown in Figure 38 the prism coupler measurements exhibit deviation with index data obtained from ellipsometry measurements. The prism coupler measurements have been repeated ten times in two to four separate regions and were found to be highly consistent. Possible reasons for the deviation between measurements are believed to be associated with lack of calibration before taking measurement. Thus, it is believed that the index data realized via the ellipsometric

method is actually below the true index value and therefore has a direct impact on the calculated visible and NIR absorption coefficient. We can estimate this offset to be 0.1.

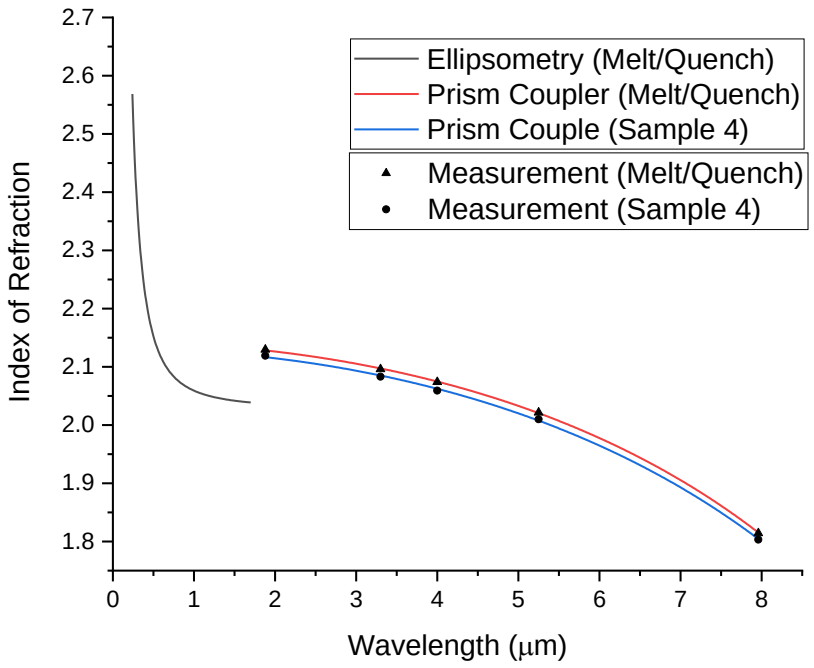

Figure 38. Refractive index as measured by ellipsometry and prism coupler techniques. The error in the prism coupler measurements are within the size of the data point.

Source: Prism coupler refractometry measurements performed by Dr. Myungkoo Kang

The index of refraction of the sintered sample 4 was lower than that of the melt/quench glass owing to its differing thermal history which resulting in a higher density glass and possible small crystallites within the substrate.

The ellipsometry and prism coupler measurement were used to calculate absorption coefficient from experimentally measured transmission.

Transmission and Absorption

Transmission data was obtained for the melt/quench glass and sintered sample 4 using FTIR [Figure 39]. Three absorption regions are labelled in the figure and are attributed to: (1) and (2) OH-group vibrations, and (3) O=W and W-O-W vibrations (Churbanov et al., 2005; Dorofeev et al., 2011).

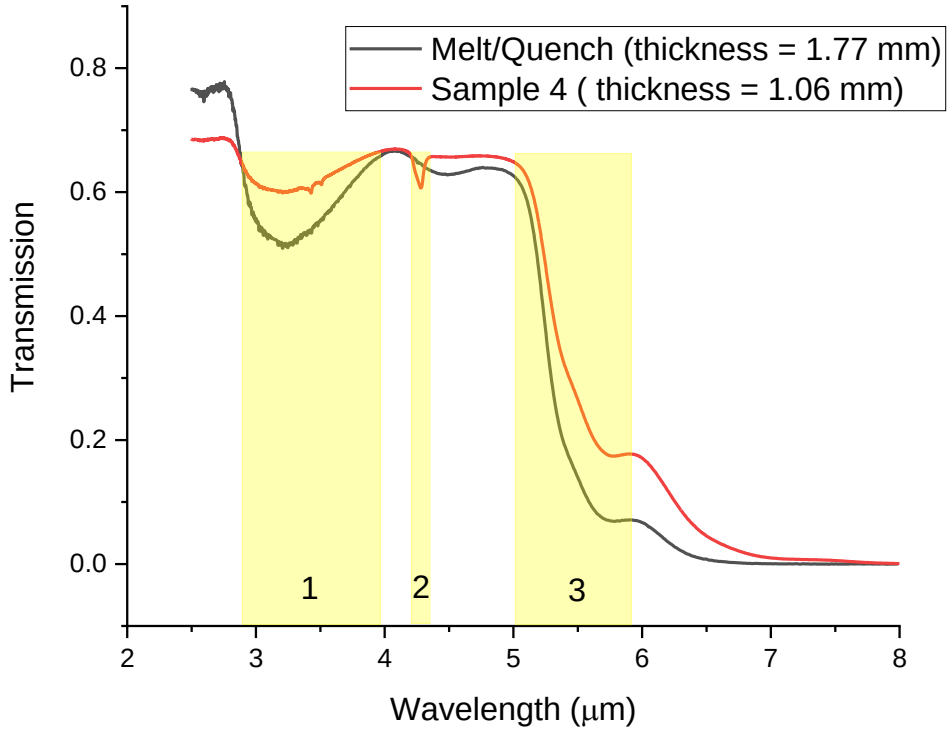

Figure 39. FTIR measurement of melt/quench glass and sintered sample 4 with the primary absorption bands labeled

Using the index of refraction data from the previous section the absorption spectrum has been calculated and is shown in Figure 40. This clearly shows the increased absorption in the sintered glass due to OH-group vibrations (regions 1 and 2) but also that the sintered glass has increased absorption across the NIR and MWIR.

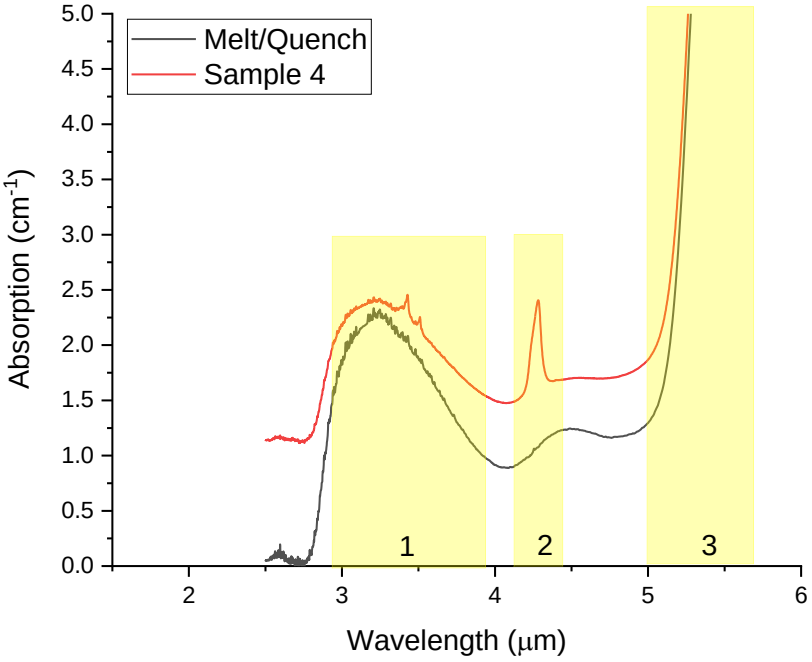

Figure 40. Absorption spectrum for TWL bulk melt/quench glass and sintered sample 4

In order to make a one to one comparison of the optical performance of the sintered sample to the melt/quench glass and literature value for a spark plasma sintered (SPS) sample the absorption coefficient was calculated from the transmission using the index of refraction obtained with ellipsometry from 1000 nm – 1700 nm [Figure 41]. The absorption coefficient is uniformly higher for the sintered glasses with a maximum of 3 cm^{-1} and the glass made through sacrificial pressure-transmitting sintering had more loss than that of the spark plasma sintered glass reported in literature (1.6 cm^{-1}) (Dohlen, 2018). This large absorption present in

the sample is likely due to black inclusions, sample darkening and non-uniform densification which appears as a haziness in parts of the sample [Figure 42]. The black inclusions and sample darkening are similar to the carbon contamination observed by Bertrand et al., (2014) and Dohlen (2018) though a source of carbon is unlikely. Instead, we postulate that some reduction of the glass occurs during sintering (reduction of W^{6+} to lower oxidation state) and forms dark color centers or, more presumably, charge-transfer complexes.

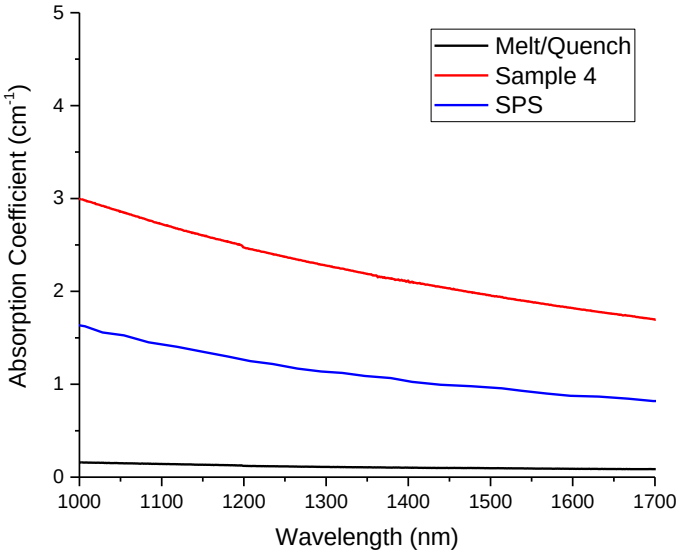

Figure 41. Absorption spectrum comparison

Source: SPS data from (Dohlen, 2018)

Figure 42. A piece of sample 4 showing black inclusions and haziness due to non-uniform densification

In order to rule out changes in optical properties based upon contamination from the sacrificial powder electron dispersive x-ray spectroscopy was performed to identify the possible presence of potassium and chlorine.

Electron Dispersive X-Ray Spectroscopy

The electron dispersive X-ray spectroscopy (EDS) spectrum of a TWL melt/quench glass, of same composition as the source powder used in sintering experiments, was acquired and is shown in Figure 43. This spectrum was used as a baseline for what the spectrum of a post-sintered sample would be if there was no contribution from potassium (K) and chlorine (Cl) from the KCl sacrificial powder used in the sintering experiments. Owing to the limited thickness of the sintered

samples, an acquisition of EDS without contribution from the aluminum sample holder was not possible. The spectra of the sample holder with residue of silver conductive paste is show in Figure 44.

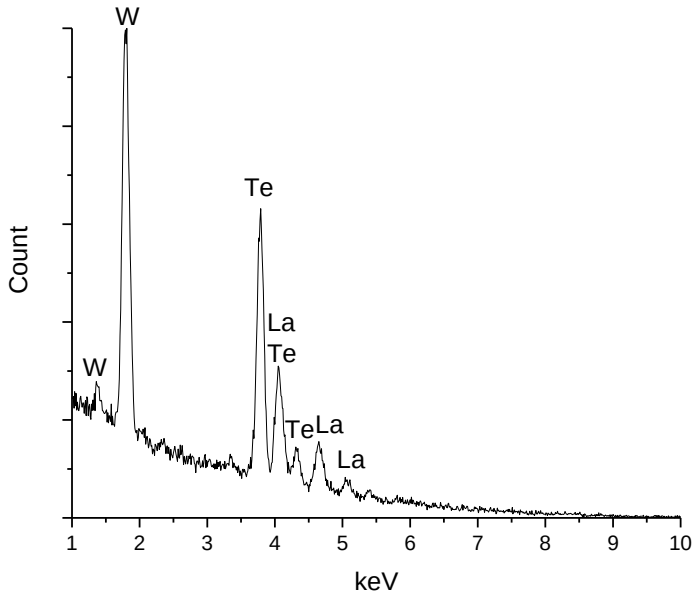

Figure 43. EDS measurement of melt/quench TWL powder

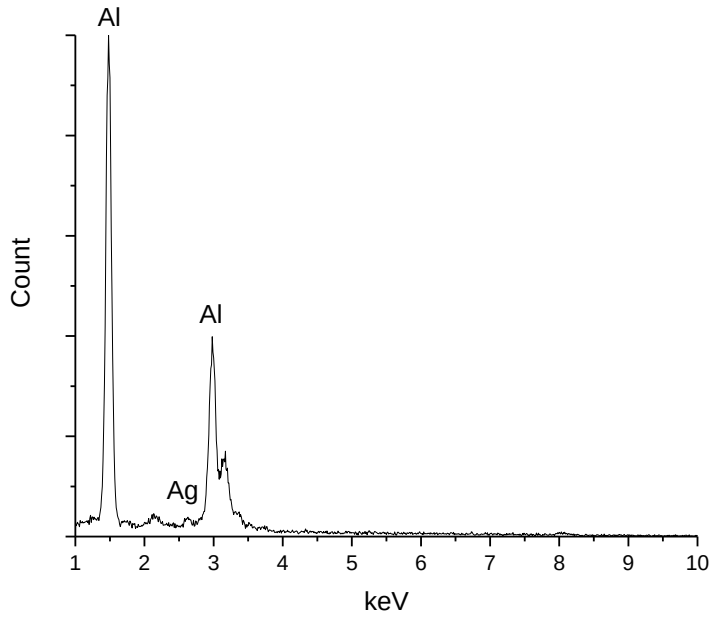

Figure 44. EDS measurement of sample holder

Spectra were acquired from sample 4, which is a sintered sample, of the cross section [Figure 45] and top (surface closest to top die plunger) [Figure 46] of the TWL material to look for possible contamination from the KCl sample powder. This sample has been polished and so contamination on the surface layer of the sample has not been evaluated. Based upon these results it is apparent that the sample is too thin to ignore the contribution of the aluminum sample holder which gives rise to two peaks on each spectra where the one at 1.5 keV overlays on top of a tungsten peak. A small potential contribution from potassium (K) is seen at 3.3 keV

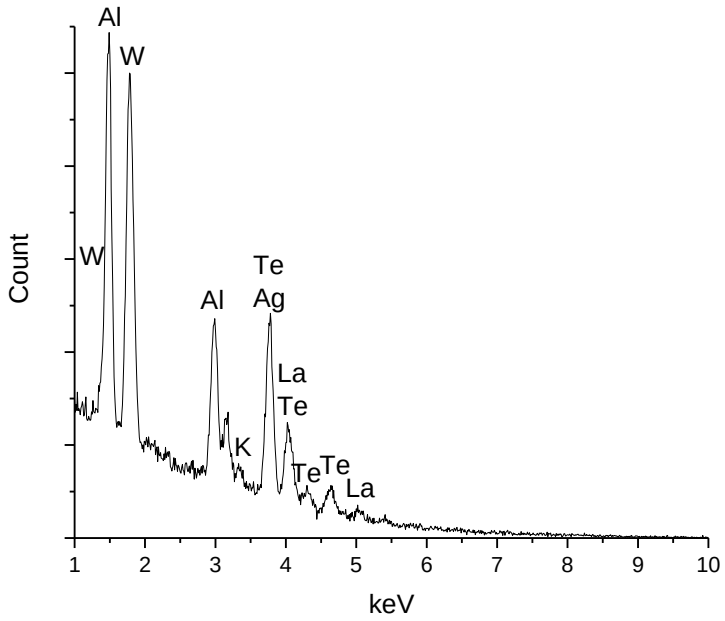

Figure 45. EDS measurement of sample 4 cross section

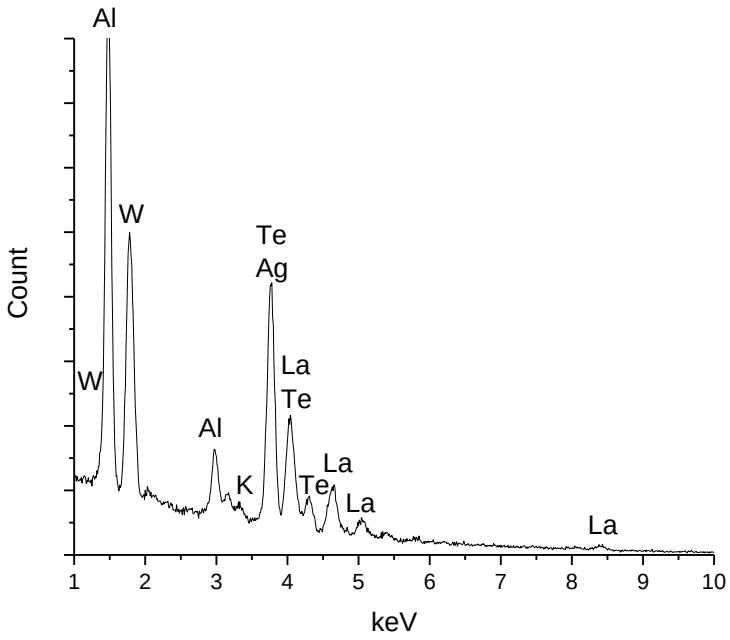

Figure 46. EDS measurement of sample 4 top of sample

To evaluate the significance of this peak and look for other K or Cl peaks each of the spectra has been normalized around the tungsten peak at 1.8 keV. Then the spectra from the melt/quench glass was subtracted from the sample 4 cross section [Figure 47] and top [Figure 48] spectra. The yellow highlighted regions are where chlorine and potassium peaks would be seen if contamination were present. It appears that potassium and chlorine are not present to a detectable level within the polished sample 4. Quantitative analysis on this data is not possible based upon the sampling procedure used as no calibration with reference samples for each element was done.

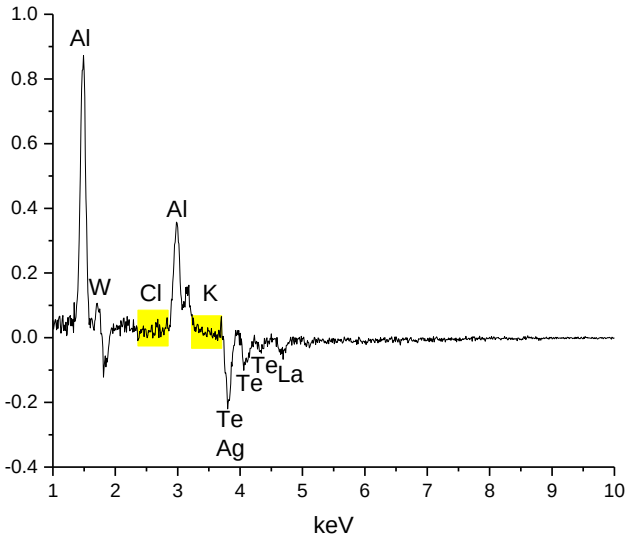

Figure 47. EDS sample 4 cross section spectra minus melt/quench spectra

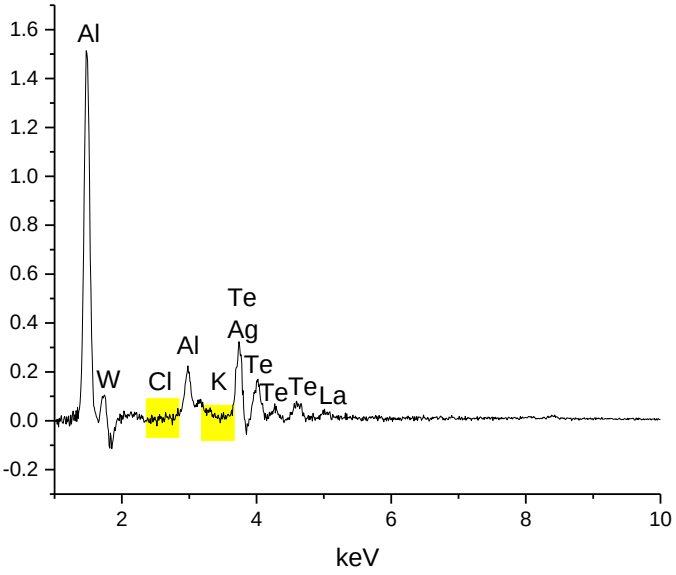

Figure 48. EDS sample 4 top spectra minus melt/quench spectra

Next, an evaluation of possible reduction in valence of tungsten within the glass was evaluated with use of Raman spectroscopy.

Raman Spectroscopy

In order to evaluate whether reduction or crystallization occurs within the glass a study of Raman spectra of glass powder intentionally processed in a high heat and rough vacuum (>10^{-3} torr) environment was undertaken. By creating an environment which approximates that of the TWL glass during the normal sintering process and holding the samples within this environment for a period of time which exceeds the normal dwell times it can be evaluated if it is possible for the tungsten to reduce during the sintering of samples and if crystallization is observed. Tungsten reduction was anticipated based upon the observation of sample darkening occurring in multiple samples such as those shown in Figure 49.

Figure 49. Darkened sample from sintering process

A Raman spectrum of the pre-sintered powder was acquired and its deconvolution into its individual peaks is shown in Figure 50. Based on previous literature on tellurite glasses the Raman peaks are assigned as shown in Table 8. The modes at 362 cm^{-1} and 924 cm^{-1} can be attributed to stretching of tungsten-oxygen bonds and if reduction is occurring the heights of these peaks should decrease as the number of such bonds are reduced. The two peaks at 1179 cm^{-1} and 1348 cm^{-1} have not been successfully attributed at this time. The Raman modes associated with crystalline TeO_2 and WO_3 are shown in Table 9.

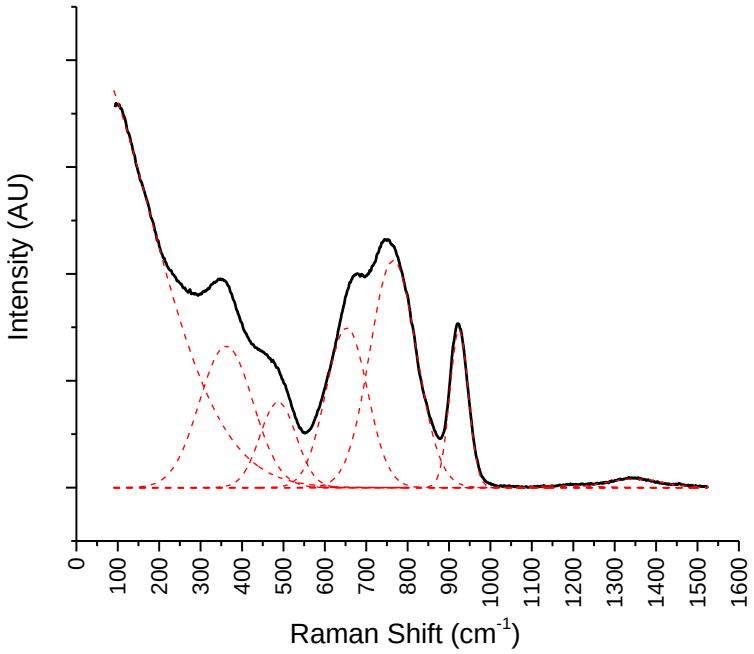

Figure 50. Deconvoluted Raman spectra of TWL pre-sinter glass powder

Table 8. Raman vibrational mode assignment

Raman Band Frequency (cm-1)	Vibrational Mode Assignment	Source
362	$[WO4]^{2-}$	3
487	Te-O-Te stretching vibrations	1
653	TeO_4 trigonal-bipyramidal	1, 2, 4
765	TeO_3/TeO_{3+1} stretching vibrations	1,4
924	W-O-W stretching vibrations	1,2
1179	Unknown	
1348	Unknown	

Source: 1 (Kaur et al., 2013) 2 (Shaltout, Tang, Braunstein, & Abu-Elazm, 1995) 3 (Bertrand et al., 2014) 4 (Sokolov et al., 2006)

Table 9. Raman vibrational mode assignment for crystalline TeO_2 and WO_3

Crystal Type	Raman frequency (cm^{-1})				
TeO_2	187	230	283	334	398
	587	643	716	761	
WO_3	268	324	714	806	

Source: (Shaltout et al., 1995)

Two other samples were similarly analyzed and deconvoluted: one which was held at the 550 ˚C dwell temperature under vacuum for 30 minutes before being cooled down and another held for 120 minutes. As with the sintered samples, these samples were heated while surrounded by KCl in a steel die within the sintering vessel. The deconvolution of each spectrum is shown in Figure 51 and Figure 52. These figures show that none of the determined peak locations correspond to the known values of crystalline TeO_2 and WO_3 further demonstrating that the samples studied likely do not contain these crystalline phases. Further evidence to suggest that if the sintered samples were crystallized, the crystalline fraction is small as their process time was shorter.

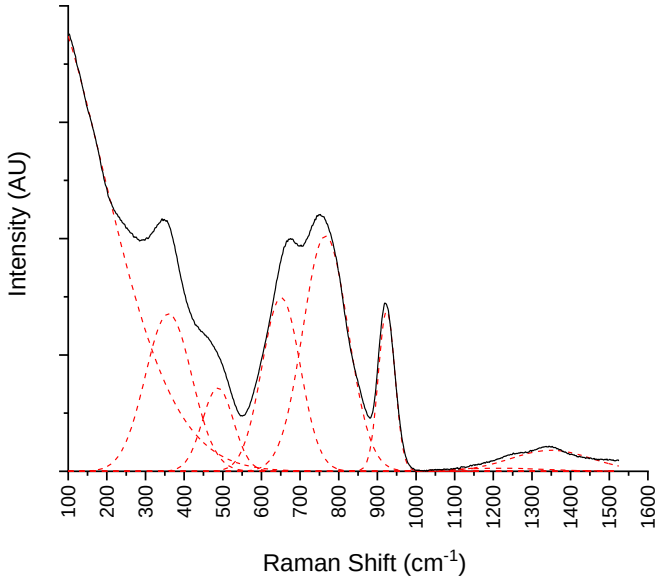

Figure 51. Deconvolved Raman spectra of TWL heat treated for 30 minutes in vacuum

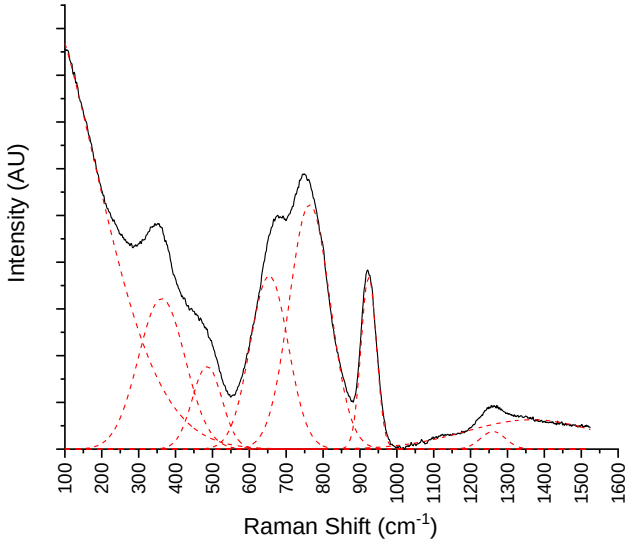

Figure 52. Deconvolved Raman spectra of TWL heat treated for 120 minutes in vacuum

A comparison of the peaks occurring at 362 cm-1 and 924 cm-1 was done [Figure 53] and found that there was no trend relating dwell time to amplitude, though the amplitudes of the peaks did differ. Based on the difference in the peak heights tungsten may be undergoing reduction but the cause is not related to dwell time in these particular experiments. The frequency of these two Raman peaks is not observed to be shifting between the different samples.

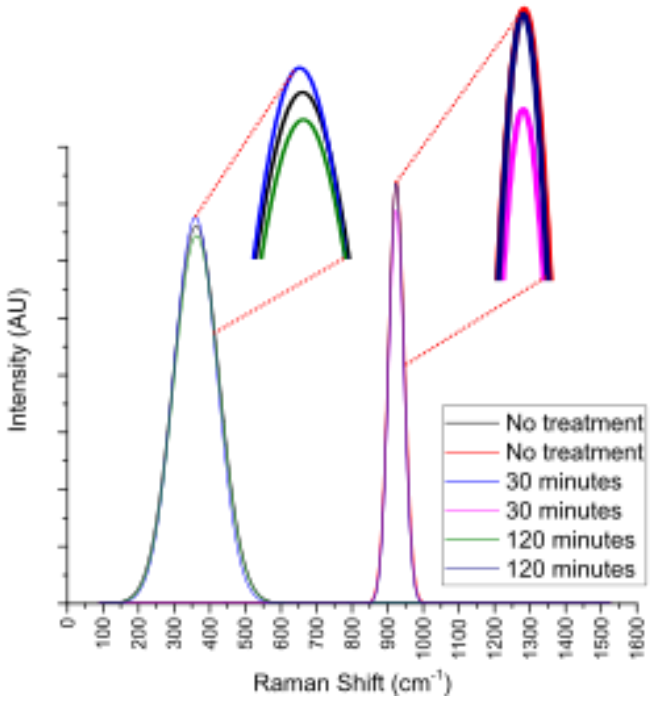

Figure 53. Comparison of tungsten related Raman peaks

Since the Raman measurements were performed at 785 nm, where a high absorption coefficient was observed, further Raman measurements would need to

be made at higher wavelengths with additional samples to determine whether or not tungsten reduction is occurring.

Conclusions

Based on viscosity and densification modelling, it was determined that full densification of TWL glass powder to greater than 99.99 % of the melt/quench glass is possible in a hot press using a sacrificial pressure-transmitting powder. DSC showed that the TWL powder used shows high stability to devitrification and made operating above the glass transition temperature possible. The early (neck formation) and final stages (full densification) of the sintering process can be seen in an optical microscope and the result is a fully densified glass body where slight differentiation between the individual grains is observed.

To evaluate the potential of a sacrificial pressure-transmitting secondary powder approach to uniaxial sintering of TWL glass an understanding of two key issues needed to be addressed:

1) Identify process-specific limitations such as material contamination from the sintering environment (die, atmosphere), die adhesion, and redox reactions.

2) Identify post process material modifications such as change to the glass' absorption spectrum, amorphous structure and density.

Based on EDS measurements no apparent material contamination occurred in the sintered glass from the sacrificial pressure-transmitting KCl powder. Observation of process improvement was that larger samples could be removed, and this removal process was made easier using a secondary powder. Raman measurements suggest signs of redox reactions occurring, but they were not correlated with process time or temperature and further measurements are necessary to confirm this result.

Sintered glass manufactured through both SPS and sacrificial pressure-transmitting sintering increase absorption broadly across the entirety of the measured spectrum. The glass manufactured through sacrificial pressure-transmitting sintering has significantly greater absorption loss than even SPS and is likely due to variations in densification visible in the glass as non-uniform haziness and trapped black inclusions. XRD and Raman confirms that the sintered materials remain largely amorphous though surface crystallization or crystallization below the detectable limit is possible. The density of the processed glasses is higher than that of the starting melt/quench powder they are derived from and the melt/quench reference bulk glass, which was caused by differing free volumes, since it is not readily explainable by the formation of crystalline phases. This explanation is supported by the decreased refractive index of the sintered sample when compared to the melt/quench reference bulk glass.

Table 10 revisits the objectives of this thesis as previously laid out and summarizes the findings.

Table 10. Findings of thesis compared to objectives

Desired TWL Attribute	Finding
>99.99 % Density of starting powder	Sintered TWL has a density that exceeds that of the starting powder owing to the applied pressure and differing thermal history
Fully amorphous	XRD confirms that the sintered glass is largely amorphous with no detectable crystal peaks
No detectable contamination from sacrificial powder	EDS found no detectable levels of potassium or chlorine from the sacrificial powder

This approach to sintering may be valuable in experiments where the sample is highly likely to adhere to a die material or where traditional die coating materials such as boron nitride or graphite is a known contaminate. In addition, the sacrificial powder may act as a diffusion barrier to prevent certain contaminates from interacting with the sintered material.

CHAPTER THREE:
TELLURIUM SINGLE CRYSTAL GROWTH

Introduction

Current infrared (IR) sensors are often bulky and designed around a single function (e.g. imaging). The next generation of systems will ideally combine higher performance and multi-functional modalities to include imaging functions with spectral and polarization information at a reduced size, weight, power and cost. Key innovations have been proposed to address these various challenges, yet further solutions are sought to enable monolithic and planar integration of these optical elements (Nayar, Yasuma, & Mitsunaga, 2015; Tsai & Brady, 2013; Twede, 2013). Hence, thin, carefully engineered components could, for example, be stacked to relay spectrally-filtered and polarization-controlled sub-images for rapid, high-resolution, single-frame acquisition of a scene.

IR polarizing elements are often built around dielectrics, semiconductors or metallic wire grids. Although efficient, these filters always absorb half of randomly polarized light and suffer from rather narrow bandwidth. On the other hand, birefringence-based polarizers separate a randomly-oriented electromagnetic field into two complementary beams (the ordinary and extraordinary rays) and can be used to create two images of orthogonal polarizations, separated by a distance determined by the degree of birefringence and the length of propagation in the material. Hence, such birefringence-based polarizing elements allow far more

polarization throughput and sensitivity than their counterparts and can be used to produce two overlapping images that can be separated using computational image processing techniques (Tsai & Brady, 2013).

However, broadband IR-transmissive materials presenting a sufficient level of birefringence to provide well-separated ordinary and extraordinary rays over an optical path of a millimeter or less are rather uncommon, particularly in the mid- to long-wave IR (MWIR and LWIR). Many candidate materials which exhibit physical property attributes that could be considered as desirable, have not been scaled to be “manufacturable” as defined by scalable size, optical quality and/or realistic price point.

Based on its exceptionally high birefringence (Δn=1.443 at 4 μm (Caldwell & Fan, 1959)), its transparency in the 3.5 – 5 μm region and past successful growth attempts, tellurium appears to be a candidate of choice for future applications. Therefore, the production and characterization of tellurium crystal has been started.

To grow single crystal tellurium, the design, construction and characterization of a transparent Bridgman furnace was undertaken. Based on the work of previous researchers it is known that a single crystal of tellurium could be successfully grown within a specially designed quartz ampoule within this furnace.

This thesis focuses on the design, construction and characterization of a transparent Bridgman furnace and the growth of tellurium crystal through use of this furnace.

Literature Review

Growth Method Overview

Numerous methods of growing single crystalline material exist and have been extensively reported in literature including: Czochralski, zone melting, Bridgman, recrystallization, vapor growth, solution growth and slow cooling to name but a few. Numerous modifications of these methods also exist, and the choice of method is highly dependent on material, application and available resources. With regards to tellurium crystal growth the three that have been most extensively studied are Czochralski, Bridgman and zone melting and associated modifications of these methods.

The Czochralski method involves pulling a crystal from a melt contained within a crucible. In order to aid in the pulling of a single-crystal either a seed crystal is dipped into the melt and then extracted or a wire is dipped creating a polycrystal and then the boule is necked down to promote the propagation of a single-crystal (Brandle, 1980; Laudise, 1970). A diagram showing the basic components of the Czochralski method is shown in Figure 54. This method along with modifications

of this method is the most common production technique for single-crystals used in industry for congruently melting materials. This technique allows for easy scale up to crystal size and the growing of crystal not physically constrained by a container. This is an important advantage when growing materials with large thermal expansion coefficients, such as tellurium.

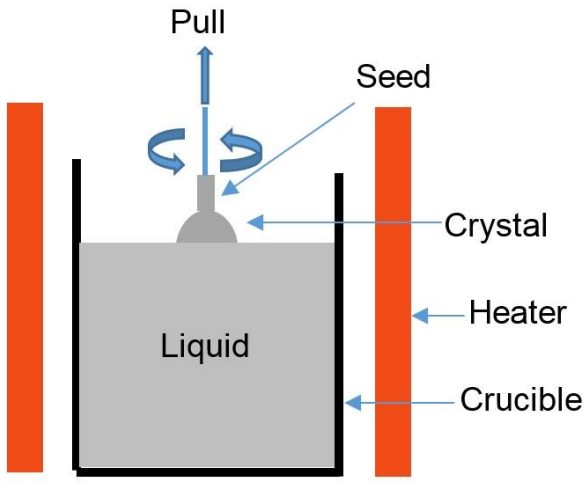

Figure 54. Diagram of Czochralski growth method

Another, though less common, technique for tellurium crystal growth is zone melting whereby a heater generating a molten zone is passed over a solid ingot of material causing a liquid phase to sweep across it as shown in Figure 55. This technique can be used for a variety of purposes including evenly distributing a dopant, controlling discontinuities and the removal of impurities but can also be used for the growth of single crystals (Shah, 1980).

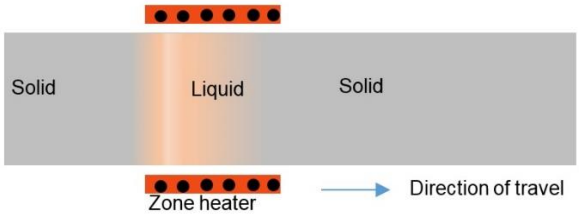

Figure 55. Diagram of zone melting growth method

The Bridgman-Stockbarger (commonly called simply Bridgman) method of growing single crystals involves the use of a dual zoned furnace where one furnace is held above the melt temperature and the other below with the temperature gradient tightly controlled [Figure 56]. An ampoule is placed within the upper hot zone and the contained material allowed to melt. Then it is slowly lowered into the cooler bottom zone and a crystal is propagated as the material solidifies. To aid in crystal growth, the ampoule usually includes a capillary which inhibits off-axis crystals from propagating. Bridgman, in 1925, proposed a single zone furnace whereby the ampoule was quenched in oil as it was lowered (Bridgman, 1925). In 1936 Stockbarger proposed the two zone modification to the Bridgman technique which is now predominately used (Stockbarger, 1936).

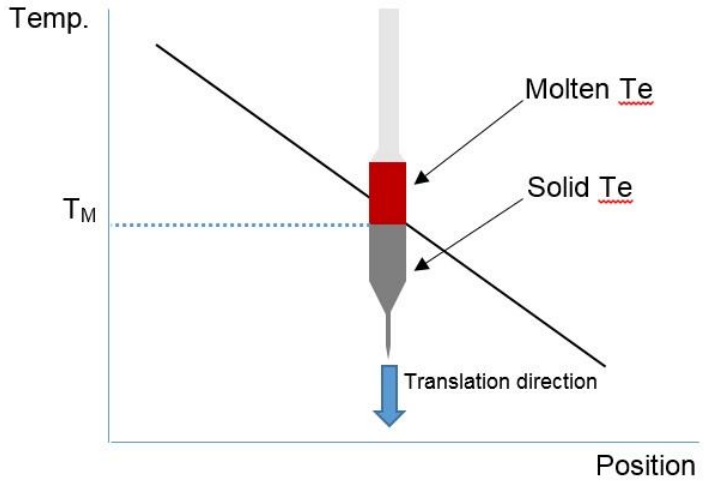

Figure 56. Diagram of temperature profile and growth in Bridgman

Tellurium Crystal Growth

A review of tellurium single crystal growth was undertaken to better understand what method should be utilized in this thesis. Table 11 shows the growth technique used by previous researchers along with the maximum dimensions of single crystalline boule they obtained. The use of the word “Bridgman” refers to any type of temperature gradient method aside from zone melting, this includes: horizontal Bridgman, Bridgman-Stockbarger and unspecified adaptations to the Bridgman method.

Table 11. Growth methods and maximum dimensions of tellurium single crystals reported in literature

Technique	Dia. (mm)	Length (mm)	Mass (g)	Source
Czochralski	15	50	-	(Caldwell & Fan, 1959)
Czochralski	17	70	-	(Keezer, 1963)
Czochralski	15	75	-	(Davies, 1957)
Czochralski	~20	55	-	(Dufresne & Champness, 1973)
Czochralski	10	15	-	(Ishiguro & Tanaka, 1967)
Czochralski	~20	~60	73	(I Shih & Champness, 1978)
Bridgman	6	90	-	(Ahmed & Weintroub, 1971)
Bridgman	6	-	-	(Bridgman, 1925)
Bridgman	6	-	-	(Caldwell & Fan, 1959)
Bridgman	20	80	-	(Chiang, 1966)
Bridgman	~3	~30	-	(Keezer, 1963)
Bridgman	15	-	-	(Loferski, 1954)
Zone melting	19	~100	-	(Chiang, 1966)

From this review it is seen that the Czochralski method has produced boules that range from 10-20 mm in diameter and have lengths of 15 – 75 mm (Caldwell & Fan, 1959; Davies, 1957; Dufresne & Champness, 1973; Ishiguro & Tanaka, 1967; Keezer, 1963; I Shih & Champness, 1978). The Bridgman technique has produced boules that are 3 – 20 mm in diameter and 30 – 80 mm in length and at times having polycrystalline crusts or unspecified imperfections (Ahmed & Weintroub, 1971; Bridgman, 1925; Caldwell & Fan, 1959; Chiang, 1966; Keezer, 1963; Loferski, 1954). Zone melting has produced boules that are 19 mm in diameter and having a length of ~100 mm (Chiang, 1966).

From this information it was determined that the most cost-effective method to produce single-crystalline tellurium would be the Bridgman method. This method offers the ability to control the environment of the melt and the target dimensions of the boule. It does however require the use of fused silica ampoules with limited ability to be reused and the low expansion ampoule would likely apply stress upon the crystal during growth. Additionally, the inner surface of the glass ampoule could serve as secondary nucleating sites making a polycrystalline crust on the tellurium boule likely.

Before assembling a Bridgman furnace, we first determined the characteristics of the setup we needed to construct. As in any liquid-solid crystal growth technique using high-purity material, the ideal condition will be one where (1) the translation rate (rate of pulling or pushing through the temperature profile) equals the growth rate, and (2) employs a geometry where the liquid-solid growth boundary is as close to flat as possible, yet slightly convex to help remove potential impurities (Laudise, 1970). The equation controlling the translation is shown to be:

$$\frac{dx}{dt} = \frac{1}{\rho_S L}\left[K_s\left(\frac{dT}{dx}\right)_S - K_L\left(\frac{dT}{dx}\right)_L\right] \quad (38)$$

Source: (Laudise, 1970)

where x is the direction of motion, dT/dx the thermal gradient of the solid (S) or liquid (L), t the time, ρ_s the density of the solid, L the heat of crystallization, and K_s

and K_L are the thermal conductivity of the solid and liquid respectively. The density of tellurium is 6.25 g/cm^3, the heat of crystallization (latent heat of fusion) is 17.49 kJ/mol, the thermal conductivity for the solid at the melt point is 2.29 W/m/K parallel to the ***c***-axis, 1.4 W/m/K perpendicular to the ***c***-axis and 2.9 W/m/K for the melt [Figure 57](Ho, Powell, & Liley, 1972; Weber, 2003). From this data, and assuming the temperature gradient of the liquid and solid matches that of the furnace and that crystal growth occurs parallel to the c-axis, one can calculate the theoretical ideal translation rate of the ampoule [Figure 58]. By translating the growth ampoule at this rate, the growth interface will theoretically stay at one position within the furnace and therefore, at a near constant temperature.

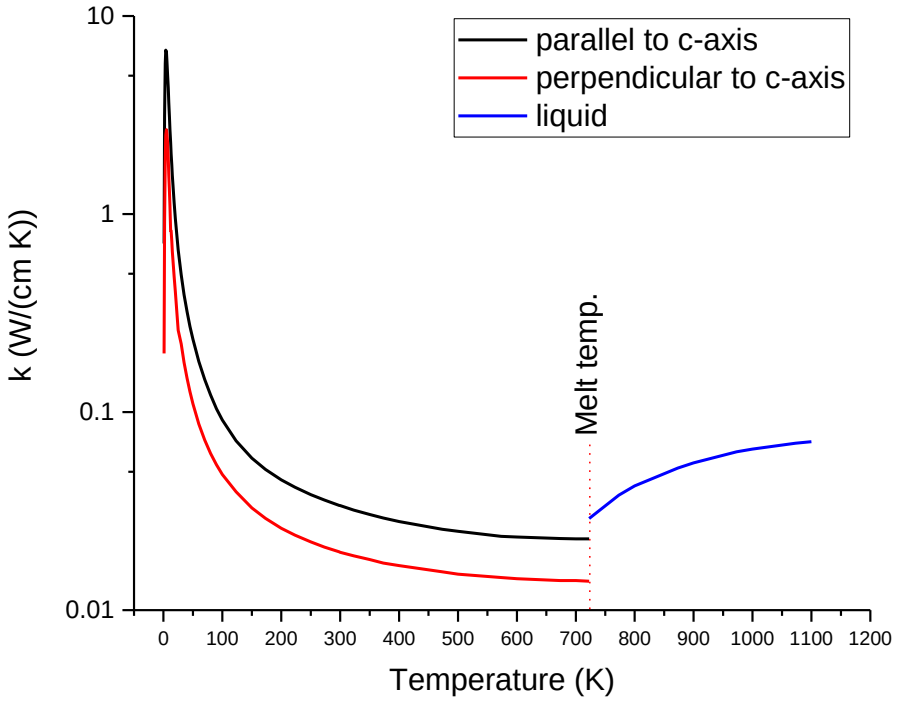

Figure 57. Thermal conductivity of tellurium

Source: Data from (Ho et al., 1972)

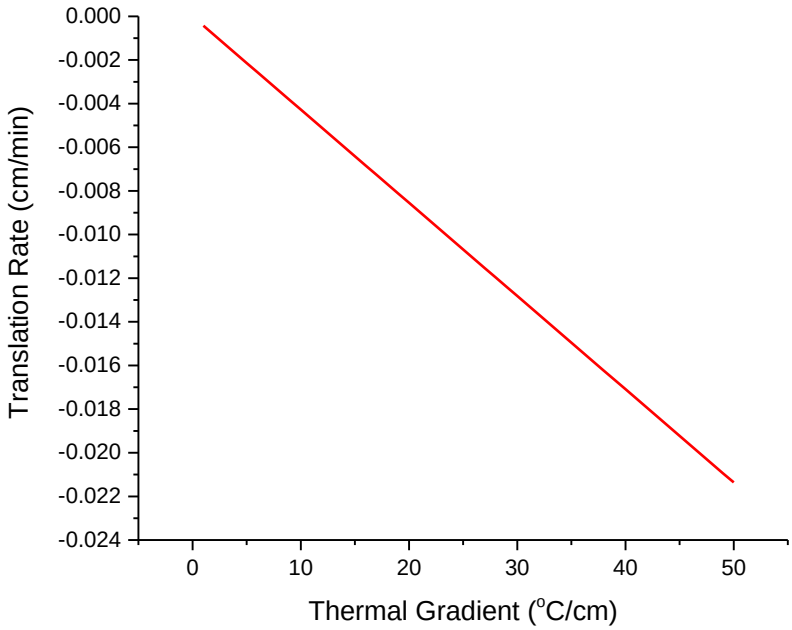

Figure 58. Theoretical ideal translation rate of the growth ampoule with c-axis of crystal parallel to translation

Ideal Bridgman-Stockbarger growth conditions of tellurium were studied by a previous researcher who found that a 2 cm diameter, 8 cm long single-crystal tellurium boule could be grown if (1) the lowering speed was set to 0.021 cm/min, (2) for a temperature gradient of 50 °C/cm, (3) an ampoule-tip angle of 45°, and (4) starting 90°C above freezing point (Chiang, 1966). The model predicts that for a temperature gradient of 50 °C/cm the ideal translation rate would be 0.021 cm/min which is precisely in line with Chiang's observation. Bridgman (1925) reported that growth can occur between 4 mm/hr and 60 cm/hr but no clear

guidance has been published on the relationship between temperature gradient, translation rate, ampoule size/design for tellurium growth in a Bridgman-Stockbarger furnace.

Properties of Tellurium Single Crystal

Tellurium crystals have chiral hexagonal-rhombohedral space groups $P3_121$ or $P3_221$ (D_3^4, D_3^6) and belongs to the chalcogen group (Adenis, Langer, & Lindqvist, 1989; Asendorf, 1957; Brown & Forsyth, 1996). The atoms in a tellurium lattice are arranged in chains which spiral along the c-axis and each spiral chain consists of three atoms with the fourth situated directly above the first [Figure 59] (Adenis et al., 1989; Bradley, 1924; Brown & Forsyth, 1996; Loferski, 1954; V. B. Voloshinov, 2004). These screw axes are classified as either right-handed (3_1) or left-handed (3_2) depending on the direction of rotation and are made up of strong covalently bonded atoms but the atoms that make up the chains are bound to their neighbors through weak Van der Waals forces and metallic binding (Loferski, 1954).

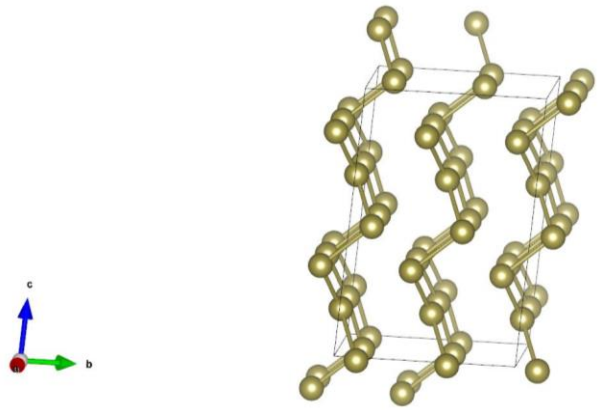

Figure 59. Crystallographic supercell structure of tellurium

Source: Position data from (Adenis et al., 1989)

The large crystalline anisotropy of tellurium, which is at the origin of its exceptional birefringence amongst materials, also causes a high non-uniformity of its other properties such as hardness and thermal expansion. When heated, tellurium will contract parallel to the c-axis and expand perpendicular to the c-axis having a coefficient of linear thermal expansion of -1.52×10^{-6} K^{-1} and 27.5×10^{-6} K^{-1}, respectively (Browder, Ballard, & Klocek, 1991).

Tellurium also has a high index of refraction (n_o and n_e) [Table 12] and a transmission window from 3.5-25 µm (Chai, 1995; Hartig & Loferski, 1954). The absorption spectrum [Figure 60] shows that this transmission window does not apply to the extraordinary axis where transmission is diminished in the 8 - 14 µm window (V. Voloshinov, Balakshy, Kulakova, & Gupta, 2008). For use as a waveplate, it would be necessary to have a high transmission in both polarization

directions, when the beam is split, and therefore this region would not be useful for this purpose. Also, owing to its high index of refraction, anti-reflection coatings would likely be necessary on optics made of the crystal, to reduce Fresnel losses.

Table 12. Index of refraction values of tellurium at selected wavelengths

λ (μm)	n_o	n_e
3.6		6.34
3.7		6.33
3.8		6.32
3.9	4.97	6.32
4.0	4.95	6.31
4.1	4.94	6.30
4.5	4.91	6.28
4.8	4.90	6.26
5.0	4.89	6.26
5.5	4.88	6.25
6.0	4.87	6.23
6.5	4.86	6.22
7.0	4.85	6.21
7.5	4.85	6.20
8.0	4.85	6.20

Source: (Hartig & Loferski, 1954)

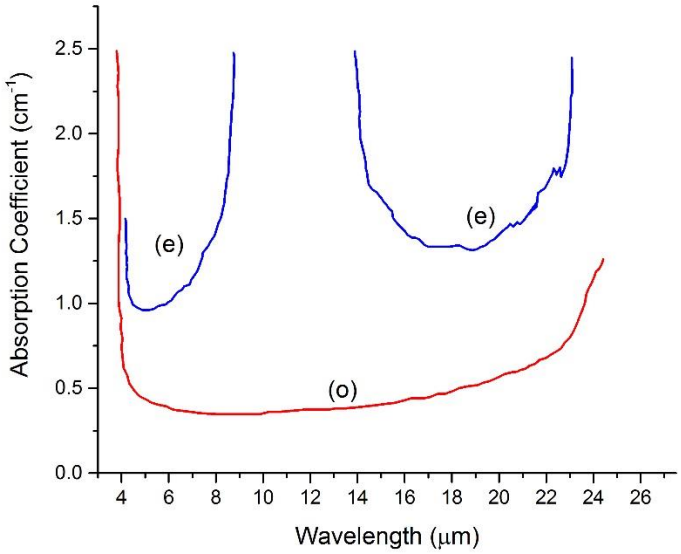

Figure 60. Absorption coefficient versus wavelength for polarized light in the ordinary (o) and extraordinary (e) directions

Source: Data from (V. Voloshinov et al., 2008)

The birefringence of tellurium is -1.45 at 4μm which is significantly greater than most other materials (*CRC handbook of laser science and technology. Supplement 2*, 1995; V. Voloshinov et al., 2008). The present study could not locate another infrared transparent material with higher birefringence. Other materials of note were: Hg_2I_2 at 0.825 at 0.63 μm, Hg_2Br_2 with 0.854 at 0.63 μm and Se with 0.81 at 3.39 μm (Gampel & Johnson, 1969; Singh, Gottlieb, Mazelsky, & Duval, 1993). This large birefringence would reduce the thickness necessary for the construction of optical elements

Tellurium also has strong optical activity and the rotation direction of the polarization state is dependent on whether the sample is dextro or levorotatory (Ades & Champness, 1975; Fukuda, Shiosaki, & Kawabata, 1975; Nomura, 1960; Stolze, Lutz, & Grosse, 1977). This rotation in the polarization direction of incident light, ρ, expressed in degrees per mm of travel, is shown in Figure 61 (Brown & Forsyth, 1996). When the incident light is split according to polarization direction in a waveplate each beam passes through a different path length of material before emerging. The strong optical activity of tellurium will rotate each of these beams by differing amounts and since index of refraction is based on the polarization direction the transmitted beams will emerge at differing angles.

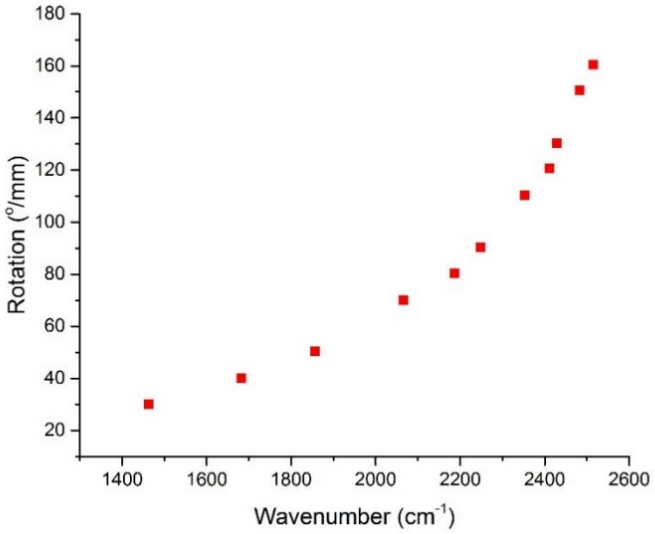

Figure 61. Optical activity of tellurium

Source: Data from (Brown & Forsyth, 1996)

Etching of Tellurium

After polishing a tellurium sample the reflection of light off the surface is too significant to effectively see crystalline grain boundaries either visually or through a microscope. Thus, in order to more clearly resolve these grain boundaries and thereby judge the size of crystalline grains, the use of etchants was investigated. It was found that etchants have successfully been used by many researchers to determine the handedness of a crystal, polish samples or determine crystal orientation. Etchants such as HNO_3 : H_2O, HCl : CrO_3 : H_2O, HNO_3 : CrO_3 : H_2O, H_2SO_4, H_3PO_4 : Cr_3, H_2SO_4, HF : HNO_3 : HAc and H_2O_2: HF have been used for these purposes (Ahmed & Weintroub, 1971; El Azab, McLaughlin, & Champness, 1975; Kalinski & Lehmann, 1976; Koma & Tanaka, 1970; Lovell, Wernick, & Benson, 1958; I. Shih & Champness, 1982; Walker & Tarn, 1990). However, no literature discussing etching to resolve grain boundaries specifically for Te were found. It is however well known that nitric acid acts to dissolve tellurium and the rate of dissolution is based on crystal orientation. Therefore, it was strongly suspected that a common nital solution (HNO_3 and CH_3OH solution) could be used to reveal grain boundaries.

Though beyond the scope of the current study, etch pits can be used in future work to determine the orientation of crystals and their handedness (levo/dextrorotary) through observation of their shape (Ahmed & Weintroub, 1971; Walker & Tarn,

1990). This presents the possibility of being able to evaluate crystal growth without the need for equipment that is currently not available to our laboratory. In addition, etching may be used in future work to create better polished surfaces of samples then what is currently possible by removing the Debye layer on the sample faces.

Methodology

Transparent Bridgman Furnace Design

For reasons of cost effectiveness and based on a review of previous growth studies, it was determined that a Bridgman furnace could be constructed and be used to grow tellurium single-crystals. The decision to make the furnace transparent was due to the desire to facilitate the seed attachment during seeded growths and have the possibility to characterize the solid-liquid interface of the growing crystal using infrared imaging. These functionalities will however be implemented in the future.

The furnace had to be of sufficient size to accommodate fused silica ampoules which are 34 mm in diameter and 356 mm in length. To this end a 36 in. (91.4 cm) long transparent furnace was envisioned, consisting of two 18 in. (45.7 cm) long zones. The upper zone had to reach temperatures in excess of 450 ˚C (tellurium melt point) and a steep temperature gradient was desired between the upper and

lower zones. Additional consideration for the placement of thermocouples and electrical feedthroughs was also necessary.

The zones were thermally segregated using a graphite zone separator and built using Kanthal™-A wire stranded helically upon three alumina supporting rods. The support structure was made of machined aluminum plates connected by bolts and threaded rods. Three concentric quartz tubes having outer diameters of 47 mm, 90 mm and 130 mm help maintain a uniform radial temperature profile from the heater wire outward. The plates, which support the furnace assembly, are designed to account for the linear expansion of the fused-silica jackets and alumina rods both radially and along their length during ramping up and down of the furnace. Additional feedthroughs had to be designed for the placement of alumina wrapped K-type thermocouples and electrical wires.

Diagrams of the bottom support plate is shown in Figure 62, the middle support plate in Figure 63 and the top plate in Figure 64 with dimensions expressed in inches as is standard for U.S. machine shops.

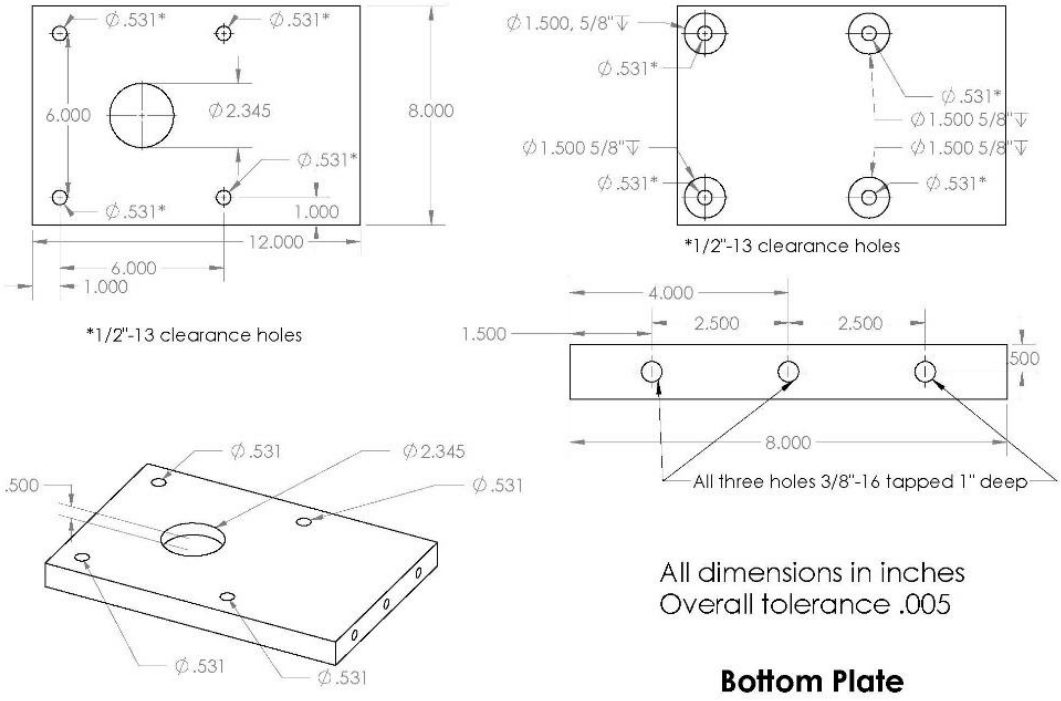

Figure 62. Transparent Bridgman furnace bottom support plate

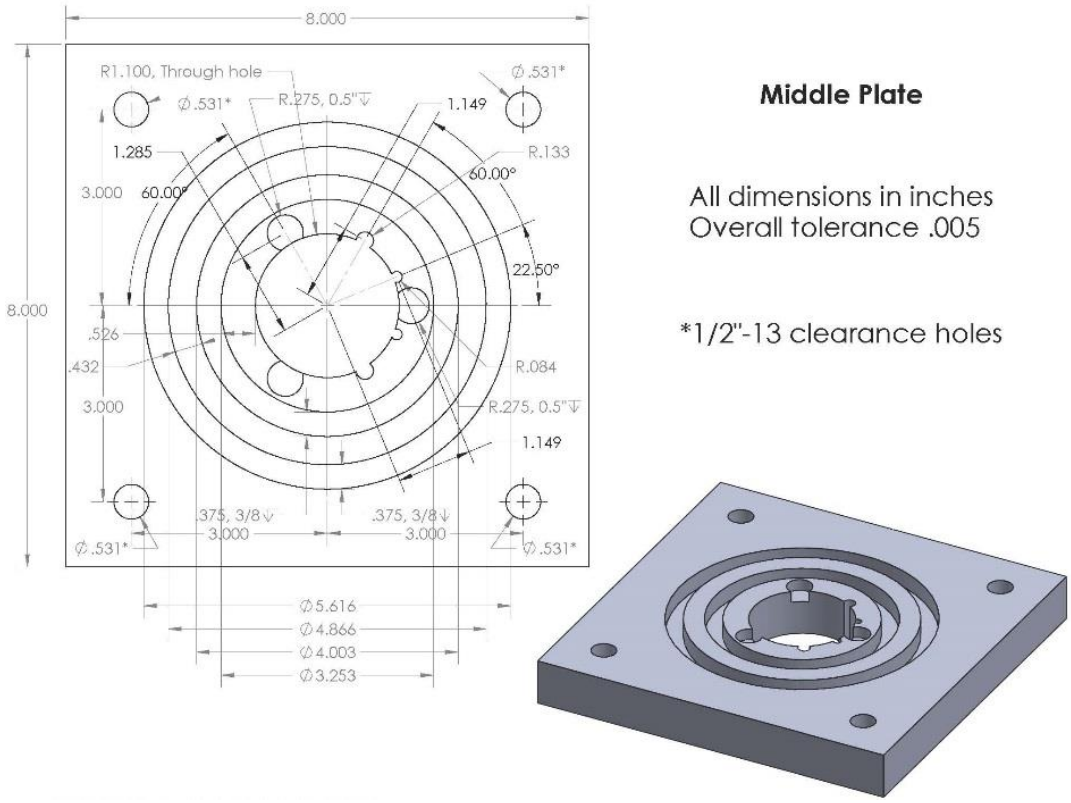

Figure 63. Transparent Bridgman furnace middle support plate

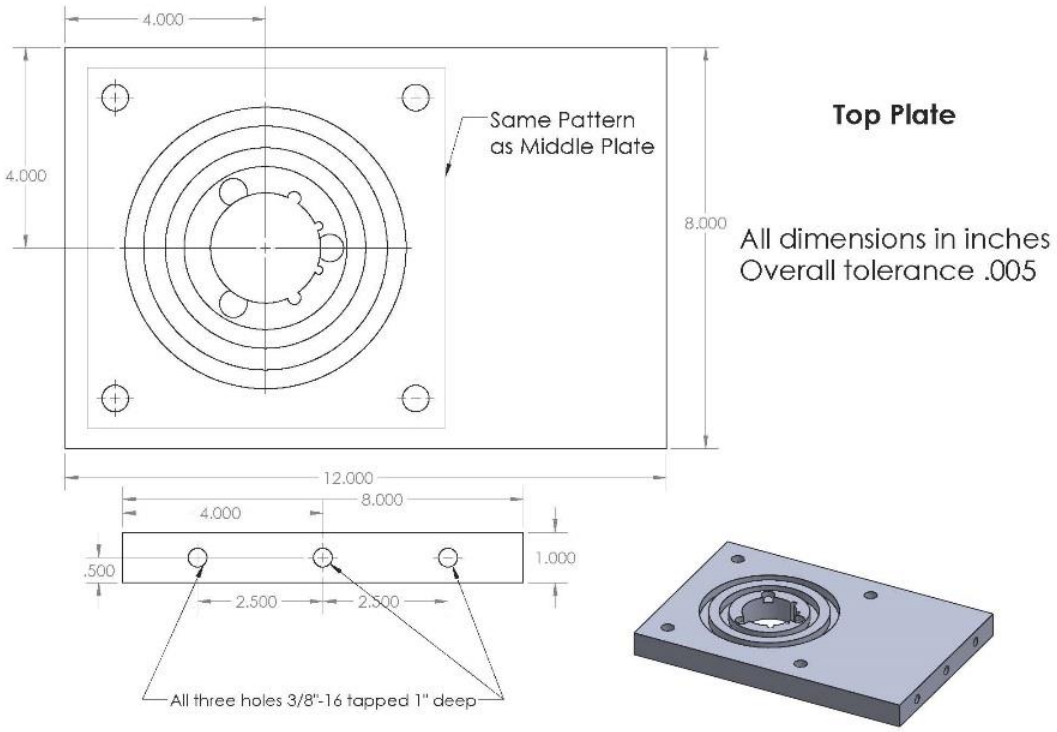

Figure 64. Transparent Bridgman furnace top support plate

The heater assembly was then constructed based around three alumina rods which are cut in a helical pattern to accommodate the heater wire. The heater wires were pre-formed into shape and placed upon alumina rods using wooden dowels and zip ties as temporary structure. A graphite zone separator was placed between the two zones and tightly fits between the inner and middle quartz tubes to reduce convection currents. A diagram of the in-process heater assembly build is shown in Figure 65.

Figure 65. Heater assembly during construction

K-type thermocouples were placed inside of thin alumina tubes and positioned near the inner quartz tube for temperature control of the upper and lower heater zones. The heater wires and thermocouples lead to a commercially acquired dual zone PID controller shown in Figure 66 which was used to regulate temperature. The glass structure of the furnace is partially enclosed by an aluminum reflector to further increase the internal temperature of the device.

Figure 66. PID temperature controller

A commercially manufactured mechanical lifter was used to translate the ampoules down the furnace from the upper hot zone to lower cool zone. This lifter is capable of a minimum translation rate of 0.22 cm/min which is significantly above the theoretically calculated 0.003 cm/min. Despite this drawback and owing to a lack of and uncertainty in the literature found about ideal translation rates initial experiments were performed using this lifter with one such experiment outlined in “Tellurium Crystal Growth Process One” section.

In order to slow down the translation rate a new lifter was built based on an Arduino™ controlled stepper motor. This new lifter was programmed to translate the ampoule at the desired 0.003 cm/min performed in discrete steps of

~0.024 mm (based upon 1.8° steps and 4.75 mm travelled per shaft rotation). This lifter is utilized for the “Tellurium Crystal Growth Process Two” section.

Tellurium Crystal Growth Process One

100 g of 99.99 % pure, zone refined, 1 – 3 mm sized tellurium pieces supplied by American Elements and stored in vacuum bags was placed inside a quartz growth ampoule manufactured by Sandfire Scientific which is 34 mm in diameter and 356 mm long [Figure 67]. A hole is drilled into the upper portion of the ampoule for hanging by a wire to the mechanical lifter and an indentation was made in the glass for sealing the ampoule with a quartz plug.

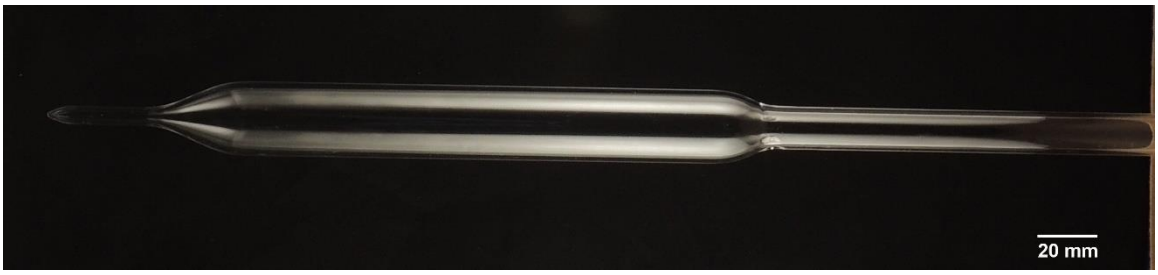

Figure 67. Growth ampoule is 20 mm inner diameter (ID), 24 mm outer diameter (OD) by 200 mm length with a 3 mm ID by 6 mm OD by 35 mm length capillary making up one end. The other end of the ampoule is a 10 mm ID by 14 mm OD by 150 mm long section meant to connect to existing vacuum valves.

Once filled a quartz plug was placed into the ampoule which stops at the indentation and the ampoule is connected to a vacuum valve and rough vacuum was drawn. Then the ampoule was sealed using a methane oxygen torch. The vacuum valve was removed, and a thin hanging wire was attached and the ampoule was hung from a mechanical lifter in the upper hot (> 450 ˚C) zone. Once the tellurium material was fully melted the ampoule was lowered at a rate of 0.41 cm/min. through the temperature gradient into the lower zone and the melt solidifies within the ampoule.

The ampoule was allowed to cool over the course of 6 hours and then removed from the system and the glass was broken away from the boule. The boule was cut using a diamond saw and then polished. Many polishing techniques were tried but the greatest success was realized when the slices were mounted onto a rotating head via wax and polished using 320, 600, 800, 1200 grit SiC paper and then 0.1 µm alumina polishing solution followed by 0.05 µm and 0.02 µm colloidal silica. The polishing method has not yet been perfected and in the future cutting with a solvent saw and chemical polishing, such as found in literature, may be necessary (Ahmed & Weintroub, 1971; El Azab et al., 1975).

Tellurium Crystal Growth Process Two

Due to the limited success of the first process a new growth procedure was developed. In order to reduce TeO_2 formation caused by trapped oxygen within the ampoule or tellurium's interaction with the quartz ampoule high vacuum was drawn within the ampoule through use of a diffusion pump and the ampoule used had an interior growth section coated in a vapor deposited 1 µm thick carbon layer. To reduce the possibility of TeO_2 being from surface contamination of the tellurium material 99.99 % pure tellurium from American Elements was purchased in larger 10 – 80 mm sized pieces which were stored within a vacuum bag within a nitrogen glovebox. This tellurium material was crushed within the glovebox and used as the source material. The ampoule was prepared inside the glovebox to prevent exposure to lab atmosphere and removed and connected to the diffusion pump while still sealed by a vacuum valve.

The sealed ampoule was suspended via wire in the hot zone of the furnace and held there for 24 hours to allow the melt to become uniform. Then the ampoule descends from the hot zone to the cool zone using the theoretically determined translation rate of 0.003 cm/min (in steps of ~0.024 mm) [Figure 68]. In order to accommodate this new translation rate a newly built lifter, which uses an Arduino™ controlled stepper motor, was constructed [Figure 69]. After all the material has

descended into the cool zone the furnace is cooled down from 430 ˚C to 23 ˚C over a period of two days (8.48 ˚C/hr).

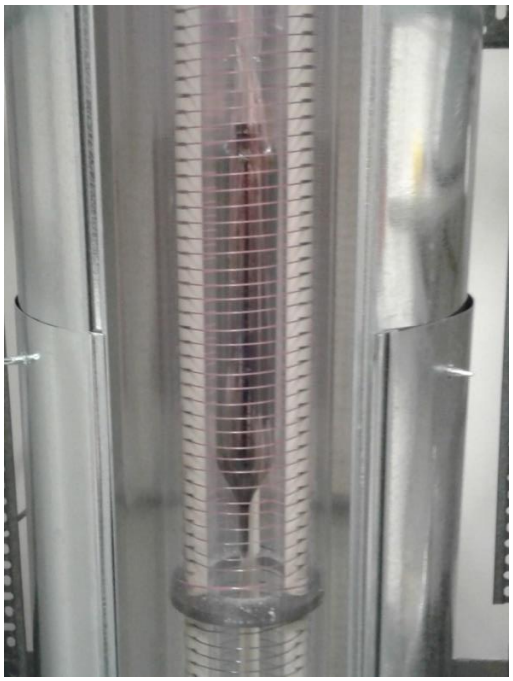

Figure 68. Carbon coated quartz ampoule descending towards the cool zone within the transparent Bridgman furnace. Outer diameter of the central quartz tube is 47 mm.

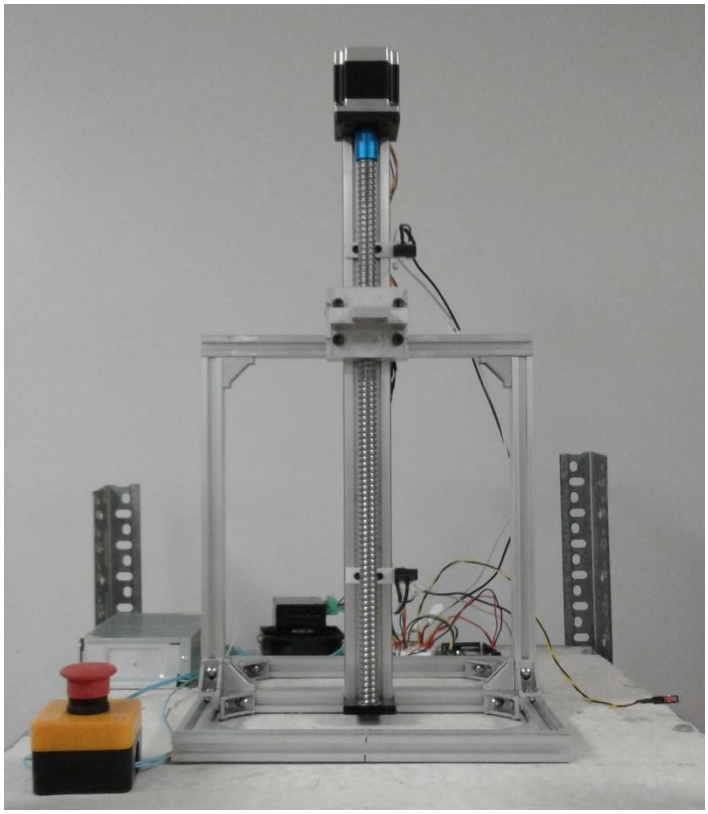

Figure 69. Arduino™ controlled lifter

Source: Built with assistance from Ryker Chute

The ampoule was then extracted from the device and the sample removed then the sample was cut and polished per the procedure outlined in “Tellurium Crystal Growth Process One.”

Crystal Structure Determination

The grain size of the tellurium crystals grown was found to be resolved through the use of a chemical etchant. A solution of nitric acid and methanol (nital) was prepared and the samples were immersed for 1 min. and then washed repeatedly in DI water. The nital solution was prepared using 70 % nitric acid supplied by Sigma-Aldrich and ACS grade methanol from Aqua Solutions. A typical nital solution used is 5 % nitric by volume. Another etchant procedure has also been adopted and uses 70 % ACS grade nitric acid supplied by Sigma-Aldrich and then 36.5 – 38 % ACS grade HCl supplied by Sigma-Aldrich. The sample is dipped in the nitric acid for a few seconds and then into the HCl for one minute.

The samples were then dried with compressed nitrogen. The process was repeated until the grain boundaries were clearly seen both visually and with an optical microscope.

Optical Microscopy

In this work, a Nikon Labophot-2 optical microscope was used, and the pictures were taken using Edmunds Optics EO-3112c camera. Microscope images were taken to determine grain size of crystal structures found within the sliced and polished boules of grown polycrystalline tellurium boules. Another method of determining structural features is through use of an infrared transmission.

Infrared Transmission

Initial experiments in the use of an infrared camera system to resolve grain structure of a grown, cut and polished tellurium sample have been performed. A FLIR SC7000 MWIR camera was used to identify large (> 1.5 μm based on spectral resolution of camera) features in polished tellurium samples. By placing a hot plate, set at 110 °C, behind a vertically mounted tellurium slice an IR image could be taken showing coloration differences caused by changes to the index of refraction or absorption coefficient (which are both crystal orientation dependent).

Owing to the optical anisotropy of tellurium and its relatively high absorption the slice imaged in this way must be sufficiently thin for clear images to be resolved. The work of improving these images has been undertaken through the use of collimators, diffusion screens and masking off of IR radiation from sources other than the hot plate but currently this work is preliminary.

Results

Bridgman Furnace

The transparent Bridgman furnace was successfully assembled and characterization of it was performed. As shown in Figure 70 the furnace consists an inner quartz tube surrounded by a heater assembly and insulated by way of two

additional layers of quartz tubing. An aluminum heat reflector was installed to partially surround the glass structure to further increase the inner temperature. The furnace was placed under a commercially acquired mechanical lifter.

Figure 70. Fully assembled transparent Bridgman furnace

The temperature profile of the transparent Bridgman furnace, which was used during crystal growth, is shown in figure 71 and shows that a temperature gradient of 6.14 ˚C/cm was utilized. The maximum temperature the upper zone can reach is ~550 ˚C which is well above the melt point of tellurium.

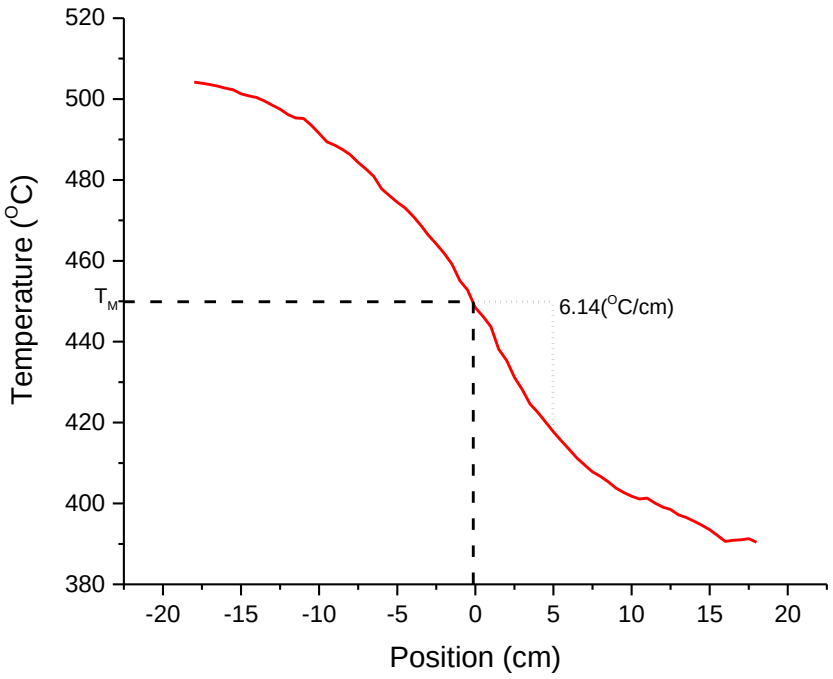

Figure 71. Experimentally determined temperature profile of transparent Bridgman furnace

The minimum translation rate of the lifter used could not match the 0.003 cm/min value suggested by theory. Even after the addition of a reducing gear the minimum translation rate of the lifter was 0.22 cm/min a level ~100 times faster than

optimally desired. After initial crystal growths showed the translation rate of the lifter to be too fast to match the theoretically determined ideal rate a new lifter was designed and is shown in Figure 69 of the “Tellurium Crystal Growth Process Two” section.

Tellurium Crystal Growth Process One

A tellurium boule was grown at a translation of 0.41 cm/min and is shown in Figure 72 where the capillary section of the boule has broken off.

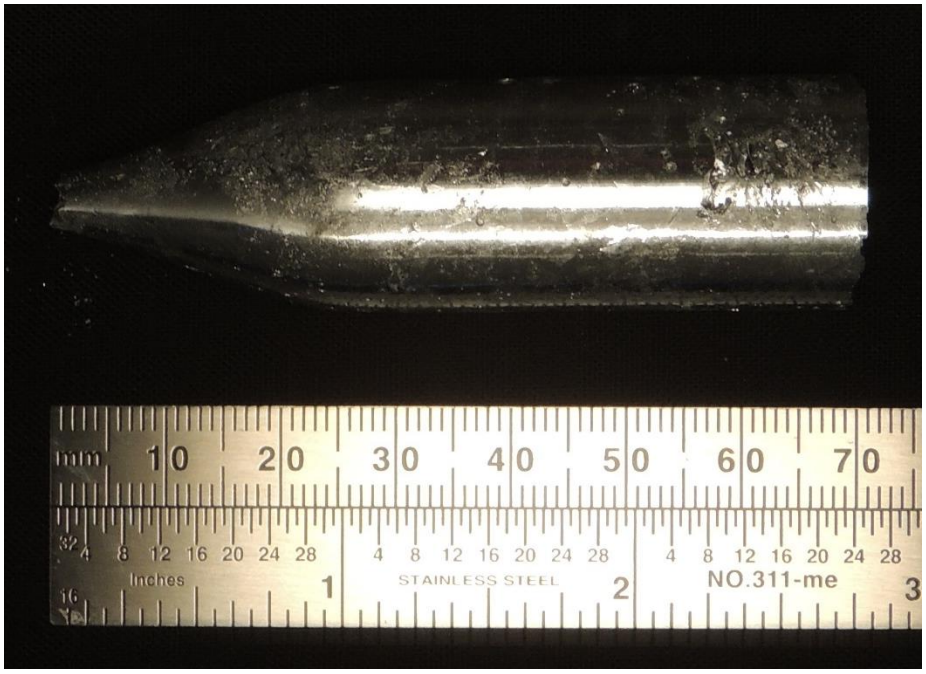

Figure 72. Tellurium crystalline boule

This tellurium boule has a damaged surface due to difficulty removing it from the quartz ampoule. This was likely due to TeO_2 contamination found on the pieces of tellurium material or from trapped atmosphere. This TeO_2 contamination forms a vapor pressure within the evacuated tube once heated and attacks the SiO_2 of the quartz ampoule and they fuse together (Prasad, Sudheer, Munirathnam, & Prakash, 2002; Veber et al., 2004).

The crystal boule shown in Figure 72 was cut into slices as seen in Figure 73 where slices at the 50 mm and 70 mm markings have been polished. Some of the grain structure of the slices can be seen as differences in reflectivity (haziness) and the presence of polycrystalline regions is more prevalent in the slices further from the capillary and near the sidewalls of the ampoule. A closer detail picture is shown in figure 74 where small stress fractures are visible in the polished faces.

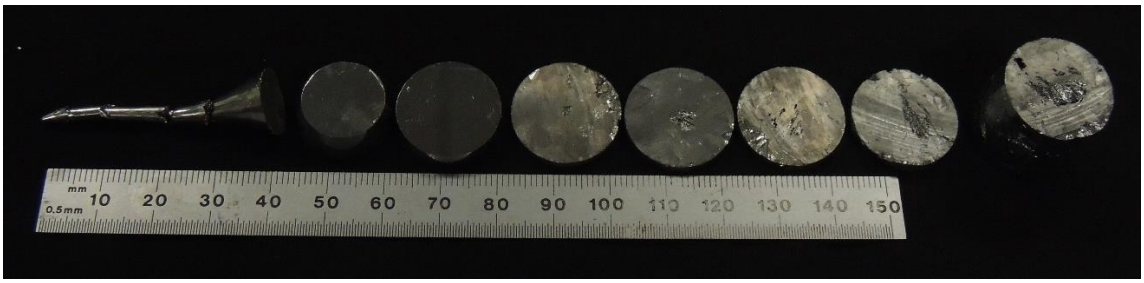

Figure 73. Tellurium crystal boule cut into slices

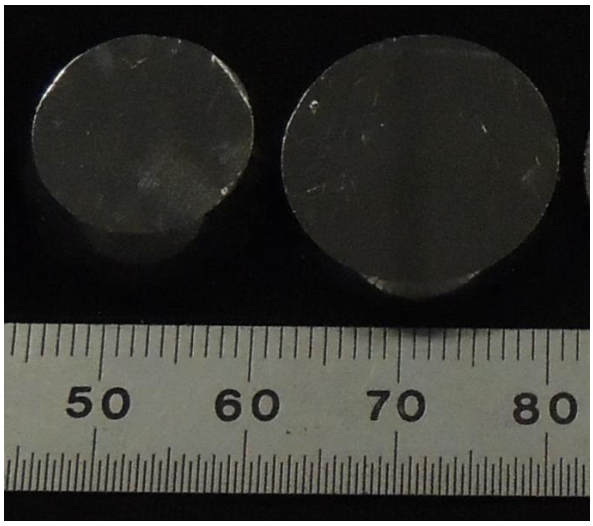

Figure 74. Tellurium crystal closer detail on two polished slices

The samples shown in Figure 74 were then etched and a high amount of crystalline grains were observed with the coloration of regions being an indicator of differing orientations [Figure 75]. Observed through an optical microscope with polarized light the individual grains of tellurium can be clearly seen [Figure 76]. Defects in the polish of the material is also shown under magnification as long vertical grooves in the surface and the grain size of ~0.1 – 0.3 mm in size can be seen.

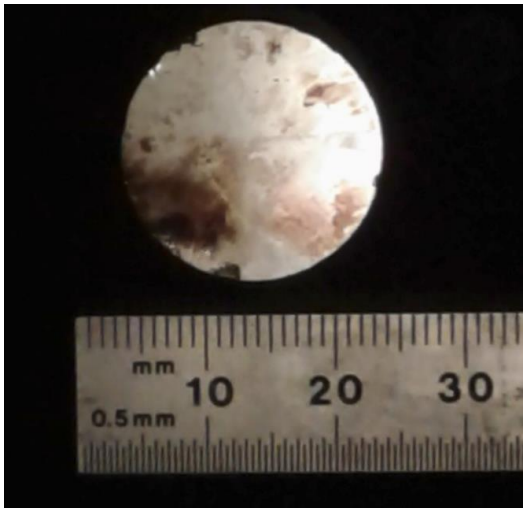

Figure 75. Etched tellurium sample

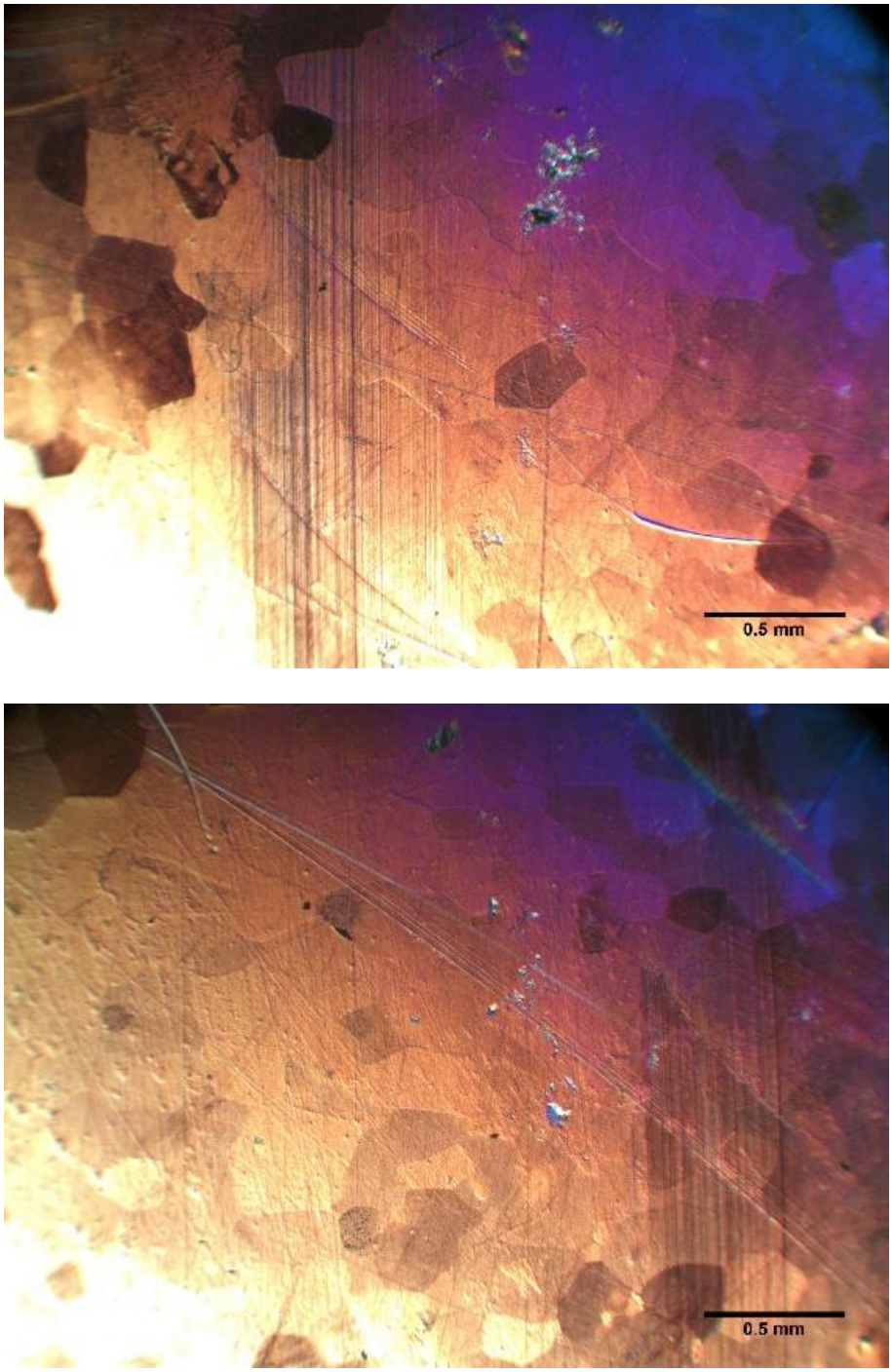

Figure 76. Microscope images of etched Te sample showing grain boundaries

Tellurium Crystal Growth Process Two

A tellurium boule was grown at a translation of 0.003 cm/min and is shown in Figure 77 and Figure 78. The exterior surface of the boule shows very little damage from sample adhesion to the now carbon coated quartz ampoule though the capillary section was still unable to be removed with the boule.

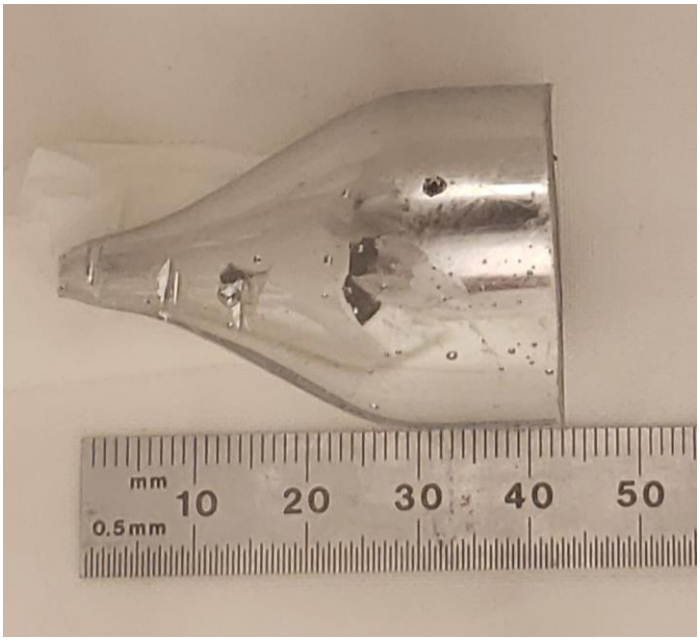

Figure 77. Tellurium crystalline boule, side profile, after process improvements

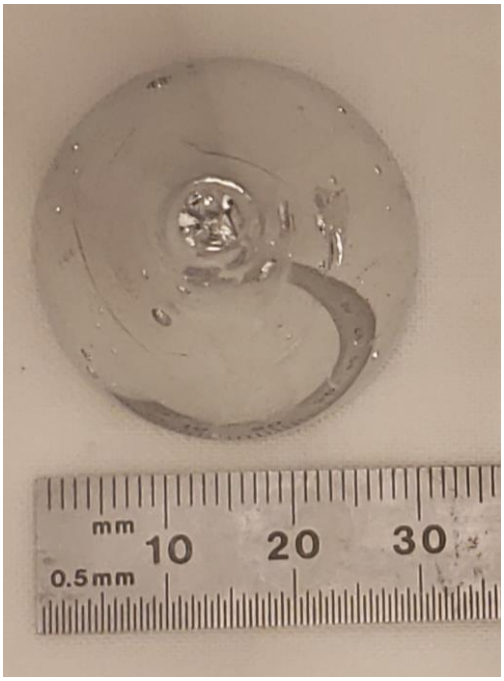

Figure 78. Tellurium crystalline boule, bottom view, after process improvements

The crystal boule was cut into slices as seen in Figure 79 and these slices were polished in preparation of etching [Figure 80]. The number of visible stress fractures has been reduced compared to the boule from growth method one.

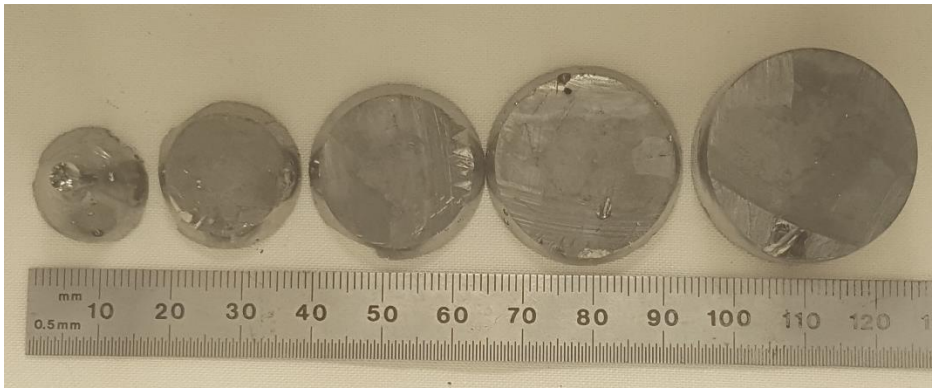

Figure 79. Tellurium crystal boule cut into slices

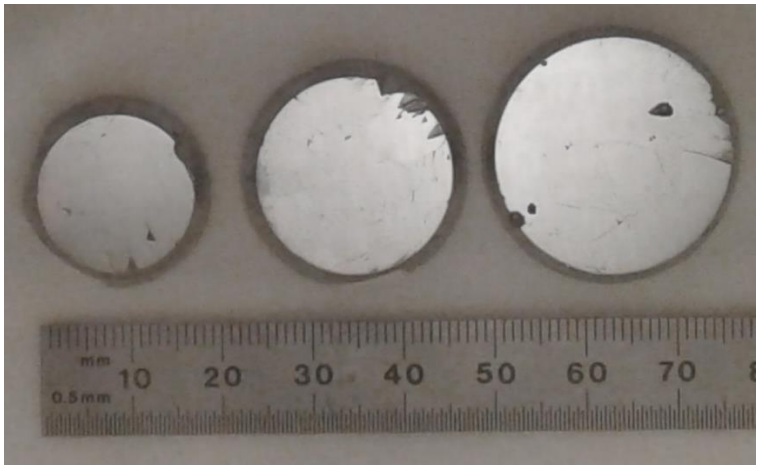

Figure 80. Polished tellurium slices

The polished slices were etched and the grain structure of the boule revealed [Figure 80]. Under microscope differences in coloration between regions can be used to differentiate the individual grains and some of the larger grains have been outlined [Figure 82]. Etching revealed that some of the grains have ~0.5 cm

diameter. This is a significant improvement from the process one growth and are of large enough size to be extracted for future seeded growth.

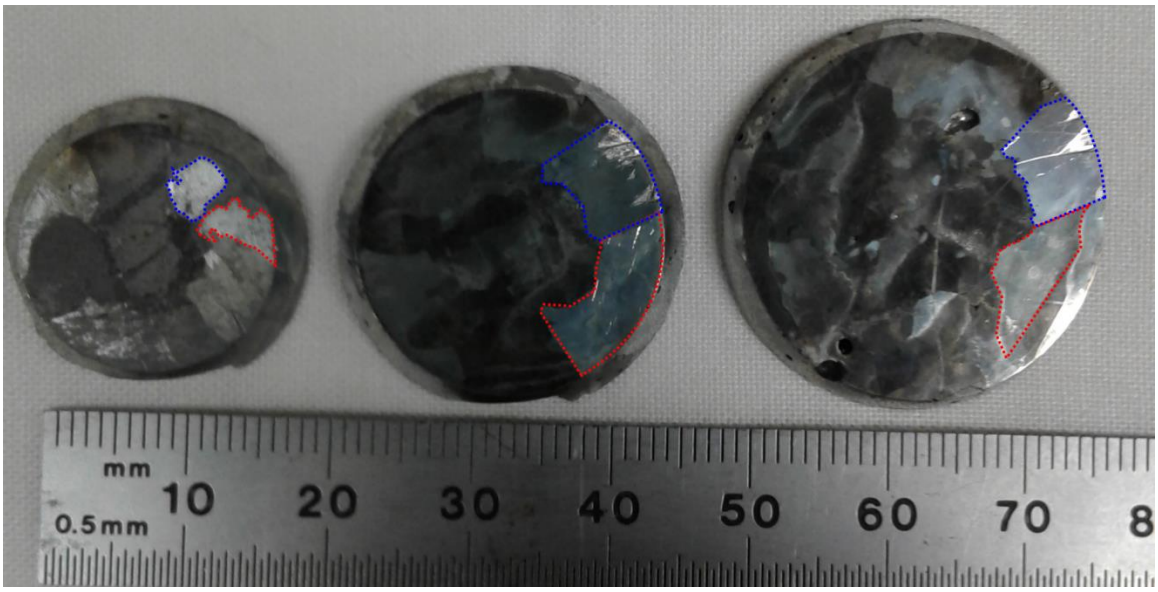

Figure 81. Etched tellurium sample with outlines showing large single crystalline grains

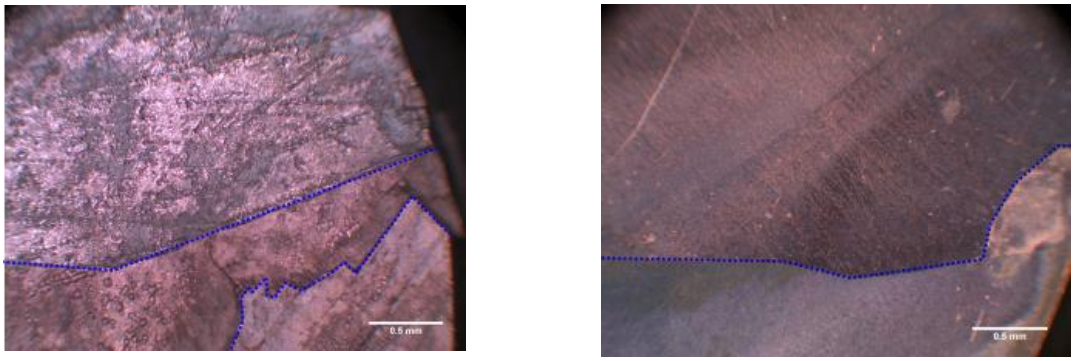

Figure 82. Microscope images of etched Te. Grain boundaries are highlighted by blue dotted lines as a guide to the eye.

The distinctive white powder of TeO_2 was no longer seen suggesting that the carbon coated ampoules along with the high vacuum atmosphere have significantly improved the growth purity by decreasing the amount of oxygen in the boule.

Infrared Transmission

Figure 83 shows an IR image taken of a thin slice of tellurium. This slice was taken from a polycrystalline boule prepared via procedure one but with a translation rate of 0.22 cm/min. Dark straight lines are seen which indicate cracks in the sample which can be visually confirmed when the cracks appear on the surface. Areas of grey or differing color to the background are areas which had high losses in intensity and indicate polycrystalline grains. Though most of these features can also been seen by performing an etch test of the samples the identification of interior stress fractures is not possible through etching.

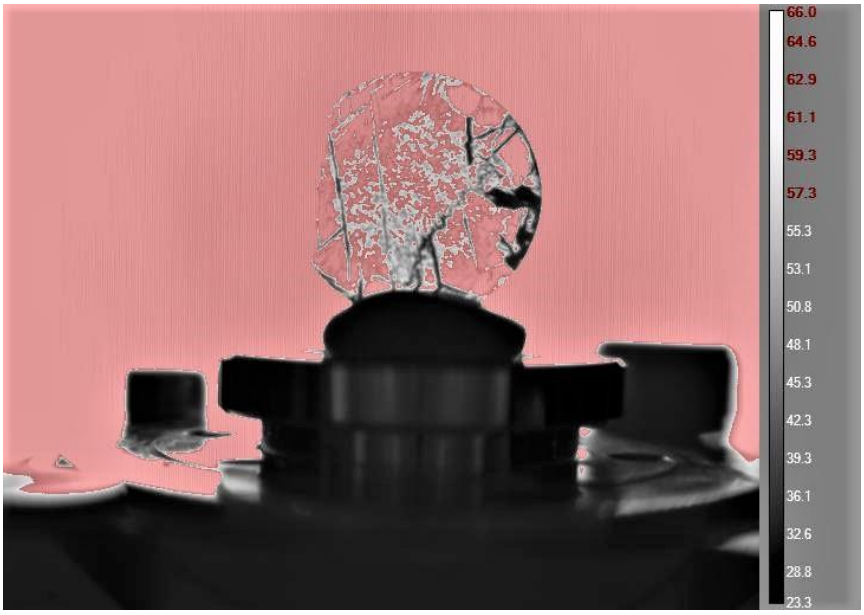

Figure 83. Tellurium slice seen in transmission using an infrared camera

This method shows promise for use in growth process improvement, particularly with materials which are optically isotropic and have lower absorption in the IR but are opaque to visual inspection. With a differently designed ampoule (square not cylindrical) and using a material which is less absorbing it would likely be possible to resolve these interior stress fractures without the need to break the ampoule.

Conclusions

Successfully constructed a transparent Bridgman furnace which is capable of a 6.14 ˚C/cm thermal gradient and consisting of two zones each 18 in. in length. The transparent furnace enables the ability to visually see the growth interface and ampoule placement within the furnace and key advantages for future growth

processes. A newly built translation device can match the theoretically determined ideal translation rate for tellurium growth of 0.003 cm/min.

The grain size of two tellurium boules grown using differing procedure was evaluated through use of a chemical etch test and optical microscope. The boule grown through the method described in “Tellurium Crystal Growth Process One” had damage to its exterior surface due to partial adhesion to the quartz growth ampoule owing to the formation of TeO_2. All slices taken from the boule have been shown to be polycrystalline with a grain size ranging from ~0.1 – 0.3 mm in size.

Process improvements were made as described in “Tellurium Crystal Growth Process Two” in order to reduce TeO_2 formation and reduce the translation rate to the theoretically determined 0.003 cm/min. These improvements were successful in decreasing TeO_2 formation and the sample no longer adhered to the quartz tube. The boule grown is polycrystalline but grain sizes ~ 0.5 cm in size. These grains are now of adequate size to extract for future seeded growth.

Future growth processes may benefit from the use of infrared imaging which has been shown to be able to resolve internal fractures, defects and grain structure within a crystalline tellurium slice.

CHAPTER FOUR:
CONCLUSIONS

Summary of Findings

TWL sintered glass using a sacrificial pressure-transmitting powder in a hot uniaxial die creates a fully densified compact with little to no crystallization and without contamination from the KCl powder. These compacts have increased optical absorption and decreased transmission in the near and mid-wave infrared.

Based on EDS measurements no apparent material contamination occurred in the sintered glass from the sacrificial pressure-transmitting KCl powder. Process improvement was made in that larger samples could be removed, and this removal process was made easier using a secondary powder. Raman measurements showed signs of redox reactions occurring, but they were not correlated with process time or temperature and further measurements at different wavelengths are necessary to definitively determine is reduction is occurring.

Sintered glass manufactured through both SPS and sacrificial pressure-transmitting sintering both increase absorption broadly across the entirety of the measured spectrum. The glass manufactured through sacrificial pressure-transmitting sintering has significantly greater absorption loss than even SPS and was likely due to variations in densification visible in the glass as non-uniform haziness in the glass and trapped and diffuse carbon contamination. XRD confirms

that the sintered materials remain largely amorphous though surface crystallization or crystallization below the detectable limit is possible. The density of the processed glasses was higher than that of the starting melt/quench powder they are derived from caused by differing free volumes and this density difference is not readily explainable by the formation of crystalline phases.

Successfully constructed a transparent Bridgman-Stockbarger furnace and mechanical lifter capable of 6.02°C/cm and translation rate slow enough to match the theoretical ideal temperature for tellurium. Characterization of crystalline boules grown using a chemical etchant showed that grains as large as ~0.5 cm in. size can be grown using this system. The use of carbon coatings on the interior of the quartz ampoule and high vacuum atmosphere prevented TeO_2 development and allowed for easy removal of boule from the ampoule. Infrared transmission using a hot plate and infrared camera was shown to be capable of resolving internal structure and grain structure in slices of tellurium.

Recommendations for Future Research of TWL

Carbon contamination has been a key limitation in SPS sintering of TW and TWL glasses as it causes absorption losses across the IR spectra. Carbon contamination, from the graphite dies, has been found to be both powder size dependent and process dependent and attempts to prevent it with use of thin diffusion barriers has not been entirely successful. Now that it has been

established that sintering to full densification is possible using a sacrificial pressure-transmitting powder there is a need to study the conditions producing color-centers or charge-transfer complexes in this glass composition.

Recommendations for Future Research of Tellurium

The tellurium boules grown so far have been polycrystalline but with large single crystalline regions. These single crystalline regions can now be extracted and used for seeded growth where it is highly likely that larger single crystal tellurium can be grown. Once grown these crystals can be cut and polished and used to begin experiments on its possible application to devices. The fragility and high reflection loss of these tellurium single crystals will be a key limitation in its use and therefore research into the application of anti-reflection coatings and adhesion of tellurium slices to substrates should be done. This will allow the tellurium single crystal to be successfully used as a waveplate or beam splitter.

Infrared imaging shows promise for use in infrared computed tomography whereby the grain structure and defects are resolved in a three-dimensional model. Such an approach could be useful for process improvement of future crystal growths where with a specially designed growth ampoule an analysis of internal grain structure could be possibly be done without opening the ampoule. If found to be polycrystalline the ampoule and contained material could immediately be reused

in another growth experiment. This would represent a significant savings of cost and time.

APPENDIX:
PROPERTIES OF TELLURIUM

Table 13. Properties of tellurium

Property	Value
Space Group	$P3_121$-$P3_221$
Atomic Weight	127.61 (Browder et al., 1991)
Density (g/cm^3)	6.25 (Weber, 2003)
Hardness (kg/mm^2)	18 (Weber, 2003)
Thermal Conductivity (W/(m·K))	6.3 (Browder et al., 1991)
Thermal Expansion ($x10^{-6}$ K^{-1})	
$\alpha_{\| c}$ (room temp.)	$-1.52x10^{-6}$ (Browder et al., 1991)
$\alpha_{\perp c}$ (room temp.)	$27.5x10^{-6}$ (Browder et al., 1991)
T_M	723K / 449.85˚C (Browder et al., 1991)
Lattice Parameters (Å)	
a	4.46 (Chizhikov & Shchastlivyi, 1970)
c	5.92 (Chizhikov & Shchastlivyi, 1970)
Transparency Window (µm) (≥10% in 1mm thick sample at 300K)	3.5-25 (Chai, 1995; Hartig & Loferski, 1954)
Band Gap (eV)	0.33 (Chai, 1995)
Index of Refraction (n_e / n_o)	6.372 / 4.929 @ 4µm (Caldwell & Fan, 1959) 6.246 / 4.796 @ 10µm (Caldwell & Fan, 1959)
Temp. Coeff. of Refractive Index (cm^{-1})	0.3 @ 10.6µm (Browder et al., 1991)
Birefringence (Δn)	1.4 @ 10.6µm (V. B. Voloshinov, 2004) 1.443 @ 4µm (Caldwell & Fan, 1959)
Solubility (g/100 g H_2O)	Insoluble (Browder et al., 1991)
Solubility in Ethanol	Unknown
Poisson's Ratio	0.25 (Weber, 2003)
Young's Modulus E (GPa)	35 (Weber, 2003)
Rigidity Modulus G (GPa)	14 (Weber, 2003)
Bulk Modulus B (GPa)	24 (Weber, 2003)
Flexure Strength (MPa)	11 (Weber, 2003)

$$n_o^2 = 18.5346 + \frac{4.3289\lambda^2}{(\lambda^2 - 3.9810)} + \frac{3.7800\lambda^2}{(\lambda^2 - 11813)} \quad (39)$$

Source: (Weber, 2003)

$$n_e^2 = 29.5222 + \frac{9.30368\lambda^2}{(\lambda^2 - 2.5766)} + \frac{9.2350\lambda^2}{(\lambda^2 - 13521)} \quad (40)$$

Source: (Weber, 2003)

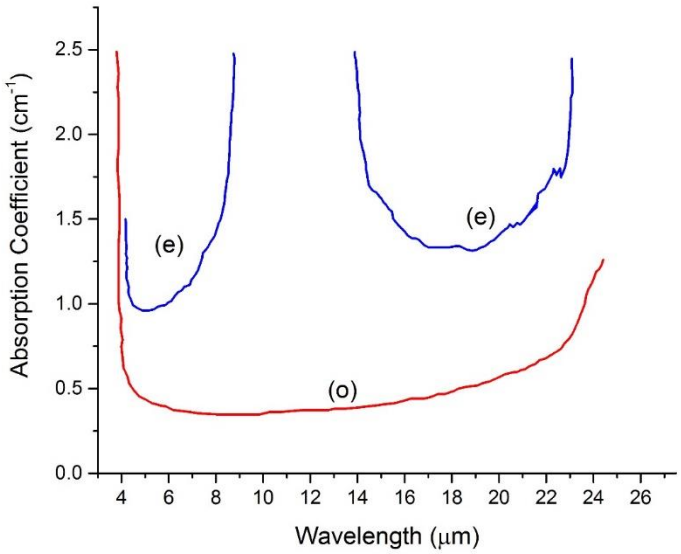

Figure 84. Absorption spectrum of tellurium for ordinary (o) and extraordinary (o) polarized light

Source: Data from (V. Voloshinov et al., 2008)

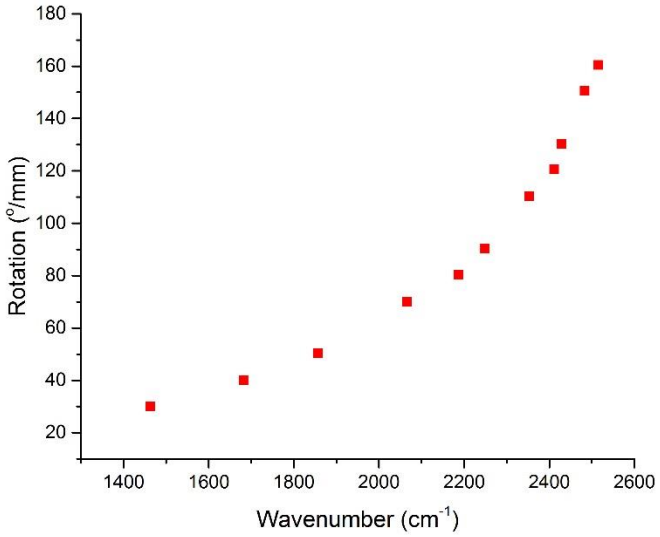

Figure 85. Optical activity of tellurium

Source: Data from (Brown & Forsyth, 1996)

LIST OF REFERENCES

Adenis, C., Langer, V., & Lindqvist, O. (1989). Reinvestigation of the structure of tellurium. *Acta Crystallographica Section C, 45*(6), 941-942. doi:doi:10.1107/S0108270188014453

Ades, S., & Champness, C. (1975). Optical activity of tellurium to 20 μm. *JOSA, 65*(2), 217-218.

Ahmed, S., & Weintroub, S. (1971). The chemical and thermal etching of tellurium single crystals. *Journal of Crystal Growth, 8*(3), 299-303. doi:https://doi.org/10.1016/0022-0248(71)90077-7

Anashkina, E. A., Andrianov, A. V., Dorofeev, V. V., & Kim, A. V. (2016). Toward a mid-infrared femtosecond laser system with suspended-core tungstate–tellurite glass fibers. *Applied optics, 55*(17), 4522-4530. doi:10.1364/AO.55.004522

Asendorf, R. H. (1957). Space group of tellurium and selenium. *The Journal of chemical physics, 27*(1), 11-16.

Badrinarayanan, P., Zheng, W., Li, Q., & Simon, S. L. (2007). The glass transition temperature versus the fictive temperature. *Journal of Non-Crystalline Solids, 353*(26), 2603-2612. doi:https://doi.org/10.1016/j.jnoncrysol.2007.04.025

Ballard, A. H., & Hendricks, J. R. (1966). The United States of America Patent No. 3,279,917. U. S. P. Office.

Barbaras, G. D. (1969). The United Stated of America Patent No. 3,455,682. U. S. P. Office.

Bernard-Granger, G., Benameur, N., Guizard, C., & Nygren, M. (2009). Influence of graphite contamination on the optical properties of transparent spinel obtained by spark plasma sintering. *Scripta Materialia, 60*(3), 164-167. doi:https://doi.org/10.1016/j.scriptamat.2008.09.027

Bertrand, A. (2015). *Verres, vitrocéramiques et céramiques transparentes à base de TeO_2 pour l'optique.* (École Doctorale Sciences et Ingénierie en Matériaux, Mécanique, Énergétique et Aéronautique), l'Université de Limoges, Limoges, France.

Bertrand, A., Carreaud, J., Delaizir, G., Duclère, J. R., Colas, M., Cornette, J., . . . Thomas, P. (2014). A Comprehensive Study of the Carbon Contamination in Tellurite Glasses and Glass-Ceramics Sintered by Spark Plasma Sintering (SPS). *Journal of the American Ceramic Society, 97*(1), 163-172.

Bradley, A. J. (1924). L. The crystal structures of the rhombohedral forms of selenium and tellurium. *The London, Edinburgh, and Dublin Philosophical Magazine and Journal of Science, 48*(285), 477-496. doi:10.1080/14786442408634511

Brandle, C. D. (1980). Crystal Pulling. In B. R. Pamplin (Ed.), *Crystal Growth* (2nd ed., pp. 275-300). Elmsford, New York: Pergamon Press.

Brennan, J. B. (1950). United States of America Patent No. 2,510,546. U. S. P. Office.

Bridgman, P. W. (1925). *Certain physical properties of single crystals of tungsten, antimony, bismuth, tellurium, cadmium, zinc, and tin.* Paper presented at the Proceedings of the American Academy of Arts and Sciences.

Browder, J. S., Ballard, S. S., & Klocek, P. (1991). Handbook of infrared optical materials. In P. Klocek (Ed.), *Handbook of Infrared Optical Materials*. New York: Marcel Dekker.

Brown, P., & Forsyth, J. (1996). The crystal structure and optical activity of tellurium. *Acta Crystallographica Section A: Foundations of Crystallography, 52*(3), 408-412.

Caldwell, R. S., & Fan, H. (1959). Optical properties of tellurium and selenium. *Physical Review, 114*(3), 664.

Carter, C. B., & Norton, M. G. (2007). *Ceramic materials: science and engineering*: Springer Science & Business Media.

Çelikbilek, M., Ersundu, A., Solak, N., & Aydin, S. (2011). Crystallization kinetics of the tungsten–tellurite glasses. *Journal of Non-Crystalline Solids, 357*(1), 88-95.

Chai, B. H. T. (1995). Optical Crystals. In M. J. Weber (Ed.), *Handbook of laser science and technology Supplement 2: Optical materials* (pp. 3-65). Boca Raton, Florida: CRC Press.

Chiang, P. T.-I. (1966). Tellurium single-crystal growth by zone-melting and Bridgman methods. *Canadian Journal of Physics, 44*(5), 1195-1197.

Chizhikov, D. M., & Shchastlivyi, V. P. (1970). *Tellurium and Tellurides* (M. Elkin, Trans. 1st ed.). Denington Estates, Wellingborough, England: Collet's.

Churbanov, M., Snopatin, G., Shaposhnikov, R., Shabarov, V., & Plotnichenko, V. (2007). Bingham viscosity and yield stress of molten $(TeO_2)0.78(WO_2)0.22$ glass. *Inorganic Materials, 43*(8), 885-887.

Churbanov, M., Snopatin, G., Zorin, E., Smetanin, S., Dianov, E., Plotnichenko, V., . . . Butsin, G. (2005). Glasses of TeO_2-WO_3 and TeO_2-WO_3-La_2O_3 systems for fiber optics. *Journal of Optoelectronics and Advanced Materials, 7*(4), 1765-1772.

CRC handbook of laser science and technology. Supplement 2. (1995). (M. J. Weber Ed.). Boca Raton, Florida: CRC Press.

Davies, T. (1957). Growth of Tellurium Single Crystals by the Czochralski Method. *Journal of Applied Physics, 28*(10), 1217-1218.

Dohlen, M. (2018). *Verres, vitrocéramiques et céramiques transparentes à base d'oxyde de tellure pour l'optique.* (École Doctorale Sciences et Ingénierie en Matériaux, Mécanique, Énergétique et Aéronautique), l'Université de Limoges, Limoges, France.

Dorofeev, V., Moiseev, A., Churbanov, M., Snopatin, G., Chilyasov, A., Kraev, I., . . . Pushkin, A. (2011). High-purity TeO_2–WO_3–(La_2O_3, Bi_2O_3) glasses for fiber-optics. *Optical Materials, 33*(12), 1911-1915.

Dufresne, R., & Champness, C. (1973). Growth of tellurium crystals by the Czochralski method. *Journal of Crystal Growth, 18*(1), 34-38.

Ebendorff-Heidepriem, H., Kuan, K., Oermann, M. R., Knight, K., & Monro, T. M. (2012). Extruded tellurite glass and fibers with low OH content for mid-infrared applications. *Optical Materials Express, 2*(4), 432-442. doi:10.1364/OME.2.000432

El Azab, M., McLaughlin, C., & Champness, C. (1975). Preparation and characterization of tellurium surfaces. *Journal of Crystal Growth, 28*(1), 1-7.

Fargin, E., Berthereau, A., Cardinal, T., Le Flem, G., Ducasse, L., Canioni, L., . . . Ducasse, A. (1996). Optical non-linearity in oxide glasses. *Journal of Non-Crystalline Solids, 203*, 96-101. doi:https://doi.org/10.1016/0022-3093(96)00338-9

Feng, X., Qi, C., Lin, F., & Hu, H. (1999). Tungsten–tellurite glass: a new candidate medium for Yb^{3+}-doping. *Journal of Non-Crystalline Solids, 256*, 372-377.

Frenkel, J. (1945). Viscous flow of crystalline bodies under the action of surface tension. *J. phys., 9*, 385.

Fujimoto, Y., Benino, Y., Fujiwara, T., Sato, R., & Komatsu, T. (2001). Transparent surface and bulk crystallized glasses with lanthanide tellurite nanocrystals. *Journal of the Ceramic Society of Japan, 109*(1269), 466-469. doi:10.2109/jcersj.109.1269_466

Fukuda, S., Shiosaki, T., & Kawabata, A. (1975). Infrared optical activity in tellurium. *physica status solidi (b), 68*(2).

Fulcher, G. (1925). GS Fulcher, J. Am. Ceram. Soc. 8, 339 (1925). *J. Am. Ceram. Soc., 8*, 339.

Gampel, L., & Johnson, F. (1969). Index of refraction of single-crystal selenium. *JOSA, 59*(1), 72-73.

Gladstone, J. H., & Dale, T. P. (1863). XIV. Researches on the refraction, dispersion, and sensitiveness of liquids. *Philosophical Transactions of the Royal Society of London, 153*, 317-343.

Googin, J. M., & McLaughlin, L. M. (1966). United States of America Patent No. 3,284,195. U. S. P. Office.

Guery, G., Cardinal, T., Fargues, A., Rodriguez, V., Dussauze, M., Cavagnat, D., . . . Richardson, K. (2014). Influence of hydroxyl group on IR transparency of tellurite-based glasses. *International Journal of Applied Glass Science, 5*(2), 178-184. doi:doi:10.1111/ijag.12044

Hartig, P. A., & Loferski, J. J. (1954). Infrared index of refraction of tellurium crystals. *JOSA, 44*(1), 17-18.

Ho, C. Y., Powell, R. W., & Liley, P. E. (1972). Thermal conductivity of the elements. *Journal of physical and chemical reference data, 1*(2), 279-421. doi:10.1063/1.3253100

Ishiguro, T., & Tanaka, T. (1967). Non-Ohmic and oscillatory behaviors at strong electric field in tellurium. *Japanese Journal of Applied Physics, 6*(7), 864.

Kalinski, Z., & Lehmann, G. (1976). Etch pits on Te basal planes. *Kristall und Technik, 11*(3), 281-283. doi:doi:10.1002/crat.19760110310

Kaur, A., Khanna, A., Sathe, V. G., Gonzalez, F., & Ortiz, B. (2013). Optical, thermal, and structural properties of Nb2O5-TeO2 and WO3-TeO2 glasses. *Phase Transitions, 86*(6), 598-619. doi:10.1080/01411594.2012.727998

Keezer, R. (1963). *Tellurium crystal growth* (AD428016). Retrieved from Cameron Station Alexandria Virginia:

Kingery, W. D., Bowen, H. K., & Uhlmann, D. R. (1976). *Introduction to ceramics* (2nd ed.). New York, NY: John Wiley and Sons.

Kissinger, H. E. (1956). Variation of peak temperature with heating rate in differential thermal analysis. *Journal of research of the National Bureau of Standards, 57*(4), 217-221.

Koma, A., & Tanaka, S. (1970). Etch Pits and Crystal Structure of Tellurium. *physica status solidi (b), 40*(1), 239-248.

Kuczynski, G. C. (1949). Study of the Sintering of Glass. *Journal of Applied Physics, 20*(12), 1160-1163. doi:10.1063/1.1698291

Kut'in, A. M., Plekhovich, A. D., & Dorofeev, V. V. (2016). A mathematical model for analysis of sequentially coupled crystallization–melting differential scanning

calorimetry peaks and the use of the model for assessing the crystallization resistance of tellurite glasses. *Inorganic Materials, 52*(6), 604-610. doi:10.1134/s0020168516060066

$La_2Te_6O_{15}$ ($La_{0.25}Te_{0.75}O_{1.875}$) crystal structure: Datasheet from "pauling file multinaries edition – 2012" in Springer Materials. (2012). Retrieved from https://materials.springer.com/isp/crystallographic/docs/sd_1500402

Lange, F., & Terwilliger, G. (1973). Powder vehicle hot-pressing technique. *AMERICAN CERAMIC SOCIETY BULLETIN, 52*(7), 563-565.

Laudise, R. A. (1970). *The growth of single crystals*. Englewood Cliffs, N.J.: Prentice-Hall.

Leal, J., Narro-García, R., Desirena, H., Marconi, J., Rodríguez, E., Linganna, K., & De la Rosa, E. (2015). Spectroscopic properties of tellurite glasses co-doped with Er^{3+} and Yb^{3+}. *Journal of Luminescence, 162*, 72-80.

Leftheriotis, G., Papaefthimiou, S., Yianoulis, P., & Siokou, A. (2001). Effect of the tungsten oxidation states in the thermal coloration and bleaching of amorphous WO_3 films. *Thin Solid Films, 384*(2), 298-306. doi:https://doi.org/10.1016/S0040-6090(00)01828-9

Lepp, J. M., & Slyh, J. A. (1951). United States of America Patent No. 2,568,157. U. S. P. Office.

Loferski, J. J. (1954). Infrared optical properties of single crystals of tellurium. *Physical Review, 93*(4), 707.

Lovell, L. C., Wernick, J. H., & Benson, K. E. (1958). Dislocation etch pits in tellurium. *Acta Metallurgica, 6*(11), 716-720. doi:https://doi.org/10.1016/0001-6160(58)90064-6

Mackenzie, J., & Shuttleworth, R. (1949). A phenomenological theory of sintering. *Proceedings of the Physical Society. Section B, 62*(12), 833.

Manière, C., Durand, L., Weibel, A., Chevallier, G., & Estournès, C. (2016). A sacrificial material approach for spark plasma sintering of complex shapes. *Scripta Materialia, 124*, 126-128.

Massera, J. (2009). *Nucleation and growth behavior of tellurite-based glasses suitable for mid-infrared applications.* (Doctor of Philosophy Dissertation), Clemson University, Clemson, SC. (463)

McClelland, J. (1961). A plastic flow model of hot pressing. *Journal of the American Ceramic Society, 44*(10), 526-526.

Morita, K., Kim, B.-N., Yoshida, H., Hiraga, K., & Sakka, Y. (2015). Spectroscopic study of the discoloration of transparent $MgAl_2O_4$ spinel fabricated by spark-plasma-sintering (SPS) processing. *Acta Materialia, 84*, 9-19. doi:https://doi.org/10.1016/j.actamat.2014.10.030

Morita, K., Kim, B. N., Yoshida, H., Hiraga, K., & Sakka, Y. (2015). Influence of spark plasma sintering (SPS) conditions on transmission of $MgAl_2O_4$ spinel. *Journal of the American Ceramic Society, 98*(2), 378-385. doi:10.1111/jace.13309

Nayar, S. K., Yasuma, F., & Mitsunaga, T. (2015). Generalized assorted pixel camera systems and methods. In: Google Patents.

Nomura, K. (1960). Optical activity in tellurium. *Physical Review Letters, 5*(11), 500.

Ohishi, Y., Mori, A., Yamada, M., Ono, H., Nishida, Y., & Oikawa, K. (1998). Gain characteristics of tellurite-based erbium-doped fiber amplifiers for 1.5-μm

broadband amplification. *Optics Letters, 23*(4), 274-276. doi:10.1364/OL.23.000274

"Optical Properties of Selected Inorganic and Organic Solids," in CRC Handbook of Chemistry and Physics. (2018). (99th (Internet Version 2018) ed.). Boca Raton, FL: CRC Press/Taylor & Francis.

Oughstun, K. E., & Cartwright, N. A. (2003). On the Lorentz-Lorenz formula and the Lorentz model of dielectric dispersion. *Optics Express, 11*(13), 1541-1546. doi:10.1364/OE.11.001541

Öveçoğlu, M. L., Özen, G., & Cenk, S. (2006). Microstructural characterization and crystallization behaviour of $(1-x)TeO_2–xWO_3$ (x=0.15, 0.25, 0.3 mol) glasses. *Journal of the European Ceramic Society, 26*(7), 1149-1158. doi:https://doi.org/10.1016/j.jeurceramsoc.2005.01.039

Prasad, D. S., Sudheer, C., Munirathnam, N. R., & Prakash, T. L. (2002). Tellurium purification: various techniques and limitations. *Bulletin of Materials Science, 25*(6), 545-547. doi:10.1007/bf02710547

Pye, D., Joseph, I., & Montenero, A. (2005). *Properties of glass-forming melts*: CRC Press.

Rabinovich, E. M. (1985). Preparation of glass by sintering. *Journal of materials science, 20*(12), 4259-4297. doi:10.1007/bf00559317

Rahaman, M. N. (2008). *Sintering of ceramics*. Boca Raton, FL: Taylor & Francis Group.

Rawson, H. (1967). *Inorganic glass forming systems* (Vol. 2). London: Academic Press Inc.

Ritland, H. N. (1955). Relation between refractive index and density of a glass at constant temperature. *Journal of the American Ceramic Society, 38*(2), 86-88. doi:doi:10.1111/j.1151-2916.1955.tb14581.x

Roumiguier, L. (2016). *Fabrication and characterization of TeO_2-based glasses for optical applications*. Internal Report. College of Optics and Photonics. University of Central Florida. Orlando.

Sarin, V. K. (1975). Morphological changes occurring during reduction of WO_3. *Journal of materials science, 10*(4), 593-598. doi:10.1007/bf00566566

Scherer, G. W. (1977). Sintering of low-density glasses: I, Theory. *Journal of the American Ceramic Society, 60*(5-6), 236-239. doi:doi:10.1111/j.1151-2916.1977.tb14114.x

Shah, J. S. (1980). Zone refining and its applications. In B. R. Pamplin (Ed.), *Crystal Growth* (2nd ed., pp. 301-355). Elmsford, New York: Pergamon Press.

Shaltout, I., Tang, Y., Braunstein, R., & Abu-Elazm, A. (1995). Structural studies of tungstate-tellurite glasses by raman spectroscopy and differential scanning calorimetry. *Journal of Physics and Chemistry of Solids, 56*(1), 141-150.

Shelby, J. E. (2005). *Introduction to glass science and technology*: Royal Society of Chemistry.

Shih, I., & Champness, C. (1978). Czochralski growth of tellurium single crystals. *Journal of Crystal Growth, 44*(4), 492-498.

Shih, I., & Champness, C. H. (1982). Basal plane etch pit orientation effect in tellurium. *Journal of Crystal Growth, 56*(1), 169-173. doi:https://doi.org/10.1016/0022-0248(82)90026-4

Shoulder, T. W., Locke, R., & Gaume, R. M. (2016). Elastic airtight container for the compaction of air-sensitive materials. *Review of Scientific Instruments, 87*(6), 063908.

Singh, N., Gottlieb, M., Mazelsky, R., & Duval, W. M. (1993). The optical quality of mercurous halide crystals. *Journal of Crystal Growth, 128*(1-4), 1053-1058.

Sokolov, V. O., Plotnichenko, V. G., Koltashev, V. V., & Dianov, E. M. (2006). On the structure of tungstate–tellurite glasses. *Journal of Non-Crystalline Solids, 352*(52), 5618-5632. doi:https://doi.org/10.1016/j.jnoncrysol.2006.09.006

Stockbarger, D. C. (1936). The production of large single crystals of lithium fluoride. *Review of Scientific Instruments, 7*(3), 133-136.

Stolze, H., Lutz, M., & Grosse, P. (1977). The optical activity of tellurium. *physica status solidi (b), 82*(2), 457-466.

Tamman, G. (1926). G. Tamman and WZ Heese, Anorg. Allgem. Chem. 156, 295 (1926). *Anorg. Allgem. Chem., 156*, 295.

Teertstra, D. K. (2005). The optical analysis of minerals. *The Canadian Mineralogist, 43*(2), 543-552.

Tsai, T.-H., & Brady, D. J. (2013). Coded aperture snapshot spectral polarization imaging. *Applied optics, 52*(10), 2153-2161.

Twede, D. (2013). Single camera color and infrared polarimetric imaging. In: Google Patents.

Uhlmann, D., Hays, J., & Turnbull, D. (1967). The effect of high pressure on B_2O_3: Crystallisation, densification, and the crystallisation anomaly. *Physics and Chemistry of Glasses, 8*, 1-10.

Upender, G., Bharadwaj, S., Awasthi, A. M., & Mouli, V. C. (2009). Glass transition temperature-structural studies of tungstate tellurite glasses. *Materials Chemistry and Physics, 118*(2-3), 298-302. doi:10.1016/j.matchemphys.2009.07.058

Varshneya, A. K. (1994). *Fundamentals of inorganic glasses*. San Diego, CA: Academic Press, Inc.

Veber, P., Mangin, J., Strimer, P., Delarue, P., Josse, C., & Saviot, L. (2004). Bridgman growth of paratellurite single crystals. *Journal of Crystal Growth, 270*(1), 77-84. doi:https://doi.org/10.1016/j.jcrysgro.2004.06.029

Vogel, H. (1921). The law of the relation between the viscosity of liquids and the temperature. *Phys. Z, 22*, 645-646.

Voloshinov, V., Balakshy, V., Kulakova, L., & Gupta, N. (2008). Acousto-optic properties of tellurium that are useful in anisotropic diffraction. *Journal of optics a: pure and applied optics, 10*(9), 095002.

Voloshinov, V. B. (2004). *Growth and characterization of tellurium single crystals for applications in imaging AOTFs*. Retrieved from

Wagner, F. C. (1960). United States Patent No. 2,928,733. U. S. P. Office.

Walker, P., & Tarn, W. H. (1990). *CRC handbook of metal etchants*: CRC press.

Wang, J. S., Vogel, E. M., & Snitzer, E. (1994). Tellurite glass: a new candidate for fiber devices. *Optical Materials, 3*(3), 187-203. doi:https://doi.org/10.1016/0925-3467(94)90004-3

Weber, M. J. (2003). *Handbook of optical materials*. Boca Raton, Florida: CRC Press.

Wilken, T. R., Morcom, W. R., Wert, C. A., & Woodhouse, J. B. (1976). Reduction of tungsten oxide to tungsten metal. *Metallurgical Transactions B, 7*(4), 589-597. doi:10.1007/bf02698592

Zhang, J., Dai, S., Wang, G., Sun, H., Zhang, L., & Hu, L. (2005). Fabrication and emission properties of Er^{3+}/Yb^{3+} codoped tellurite glass fiber for broadband optical amplification. *Journal of Luminescence, 115*(1), 45-52. doi:https://doi.org/10.1016/j.jlumin.2005.02.009